

The Theory and Modeling of Solar Cells Based on Semiconducting Quantum Dots

by

Ruibin Liu

Department of Chemistry
Duke University

Date: _____

Approved:

David N. Beratan, Supervisor

Weitao Yang

Michael J. Therien

Jie Liu

Dissertation submitted in partial fulfillment of
the requirements for the degree of Doctor
in the Department of
Chemistry in the Graduate School
of Duke University

2018

ABSTRACT

The Theory and Modeling of Solar Cells Based on Semiconducting Quantum Dots

by

Ruibin Liu

Department of Chemistry
Duke University

Date: _____

Approved:

David N. Beratan, Supervisor

Weitao Yang

Michael J. Therien

Jie Liu

An abstract of a dissertation submitted in partial
fulfillment of the requirements for the degree
of Doctor of Philosophy in the Department of
Chemistry in the Graduate School of
Duke University

2018

Copyright by
Ruibin Liu
2018

Abstract

Quantum dots (QDs) are promising building block materials for many emerging energy-harvesting applications. We theoretically investigated the influences of the QD-QD (CdTe-CdSe) charge transfer rates and mechanisms on QD solar cells power conversion efficiencies using multi-level modeling methods including the first principle quantum chemistry calculations of QD electronic and charge transfer properties and the kinetic modeling of solar cell performances.

We developed tight-binding electronic structure models to explore the QD electronic properties, and the charge transfer kinetics including their dependences on QD sizes and QD surface-to-surface distance. We calculated the QD-QD charge transfer rates following the non-adiabatic rate expression by Marcus. The QD-QD electronic coupling strength decays exponentially as the QD surface-to-surface distance increases. The QD-QD charge transfer rates generally increase (decay) as the acceptor (donor) QD radius increases. We found that the TS coupling mechanism can dominate the QD-QD coupling over the TB coupling. The difference between the TS and TB coupling size dependences results in a dominance switch between the TS and TB charge transfer mechanisms in the QD dyad as the QD sizes grow.

We further explored the use of an external charge to modulate the QD-QD coupling strength and the coupling mechanism. We found that a positively charged group

in the bridge strengthens the D-A coupling for all QD sizes. A negatively charged group in the bridge causes the D-A coupling reduction in large QDs. For small QDs, the D-A coupling variation induced by the negative charge depends on the QD sizes. Compared to the neutral bridge, we found that through-solvent and through-bridge mechanisms switch their dominance at smaller (larger) QD sizes for the positively (negatively) charged group in the molecular bridge.

Using the computed charge transfer rates, we explored the power conversion efficiencies of QD solar cells based on QD dyads and QD triads. We found that the external and internal power conversion quantum efficiencies are significantly enhanced by introducing a third QD between the donor and acceptor QDs. The improvements in the efficiencies can be further enhanced by tuning the band-edge energy offset of the middle-position QD from its neighbors.

Dedication

This dissertation is dedicated to my daughter, wife, parents and other family members. My parents have been supporting my life and study all through primary school to graduate study both spiritually and financially with full heart and love. Without them, I could not even come to the United States and Duke University. My wife admires my interests, respects my decisions and accompanies me through all the happiness and sorrow. My lovely daughter has been the biggest motivation for keeping writing this thesis. I am thankful to the nature for giving me such lovely family members.

Contents

Abstract	iv
List of Tables	x
List of Figures	xi
Acknowledgements	xiii
1. Introduction	1
2. Size-dependent electron-transfer kinetics of quantum-dot assemblies.....	7
2.1 Introduction to charge transfer in QD assemblies	7
2.2 Charge transfer theory and computational methods to capture charge transfer in QD assemblies.....	10
2.2.1 Charge transfer rate equation between two QDs	10
2.2.2 Tight-binding model for QDs electronic structure calculations	12
2.2.3 Reorganization energy and reaction free energy for charge transfer between two QDs	17
2.2.4 Parameterization of the tight-binding models for QDs	19
2.3 Size and dielectric constant dependent electron and hole transfer rates	25
2.3.1 Size-dependent QD DOS and activation free energy	25
2.3.2 Size-dependent TS/TB electronic coupling between QDs	28
2.3.3 Size-dependent electron transfer rates	34
2.3.4 Size-dependent hole transfer rates.....	46
2.3.5 Dielectric constant effects on charge transfer rates.....	52
2.4 Summary and conclusions	53

3. Charge-influenced Through-solvent and Through-bridge Electron Transfer Between Linked Quantum Dots.....	58
3.1 Introduction.....	58
3.2 Theoretical models and computational details	61
3.3 Parameterization of the charge induced solvent and QD energy changes	67
3.4 Results and discussion.....	74
3.4.1 Charge induced TS coupling in a QD dyad with fixed QD sizes	75
3.4.2 Charge induced TB coupling in a QD dyad with fixed QD sizes.....	80
3.4.3 QD size-dependent TS and TB couplings influenced by charged bridges.....	83
3.4.4 Tuning QD-QD charge transfer couplings using charge influenced TS and TB couplings	87
3.5 Summary.....	90
4. Solar Cell Performance Using Quantum Dot Triad Charge-separation Engines	94
4.1 Introduction to kinetics in QD dyad and triad.....	94
4.2 Theory and kinetic models for QD dyad and triad systems	98
4.2.1 Master equations in QD dyad and triad	98
4.2.2 Charge transfer rates in QD dyad and triad systems.....	100
4.2.3 Dyad and triad-based cell properties	104
4.3 Solar cell performance of QD dyad and triad systems.	108
4.3.1 I - U and P - U characteristics of QD assemblies.....	108
4.3.2 Short-circuit current I_{sc} , Open-circuit voltage U_{oc} , Maximum output power, P_{max} and Internal efficiency η_{in}	111

4.3.3 Effects of the M QD energy offsets (HOMO and LUMO) on the triad performance	117
4.3.4 Effects of QD absorber number on triad performance.....	122
4.3.5 Effects of quantum dot size on triad performance	128
4.3.6 Effects of hole effective hole mass on triad performance	129
4.3.7 Implications for PbS QD solar cells.....	130
4.4 Summary and conclusions	132
5. Conclusion	134
Appendix A.....	137
References	139
Biography.....	161

List of Tables

Table 1: Site energies and orbital coupling atom-to-atom parameters for CdTe and CdSe QDs	19
Table 2: Through-solvent coupling parameters for CdTe and CdSe QDs	24
Table 3: Cd ₃₃ Te ₃₃ and Cd ₃₃ Se ₃₃ HOMO and LUMO energy shifts.....	72
Table 4: c_1 and c_2 values in calculating the charge-influenced QD band edge energy shifts	73
Table 5: Tight-binding QD band edges and through-solvent and through-bridge couplings	76
Table 6: Parameters used in the current-voltage, output power-voltage, and efficiency calculations.....	106
Table 7: Performances of QD dyad and triad systems I.....	121
Table 8: Performances of QD dyad and triad systems II.....	129
Table 9: Performances of QD dyad and triad systems III.....	130

List of Figures

Figure 1: CdTe and CdTe QD band-edge energies	20
Figure 2: CdTe and CdSe densities of states.	21
Figure 3: CdTe-CdSe electronic couplings as a function of distance.....	23
Figure 4: CdTe and CdSe QD densities of states as a function of QD sizes.....	27
Figure 5: CdTe-CdSe charge transfer reaction free energy contour plots.....	28
Figure 6: The geometrical model of charge transfer couplings between two spherical QDs.	30
Figure 7: CdTe-CdSe charge transfer couplings as a function of QD sizes.	32
Figure 8: QD-QD charge transfer rates as a function of QD sizes.....	37
Figure 9: QD-QD charge transfer rates as a function of $\Delta_r G + \lambda$	41
Figure 10: Through-solvent and through-bridge electron transfer mechanism dominance switch.....	43
Figure 11: Ratio of electron to hole transfer rates as a function of QD radii.	46
Figure 12: Size-dependent hole transfer rates.....	47
Figure 13: CdTe-CdSe hole transfer rates as a function of $\Delta_r G + \lambda$	49
Figure 14: Through-solvent and through-bridge hole transfer mechanism dominance switch.....	51
Figure 15: Solvent dielectric constant effects.	52
Figure 16: Through-solvent and through-bridge coupling tight-binding model scheme.....	61
Figure 17: Charge-influenced water frontier orbital energetics.	69
Figure 18: Cd ₃₃ Te ₃₃ and Cd ₃₃ Se ₃₃ dyads	70
Figure 19: Charge-induced QD band edge shifts	74

Figure 20: Charge influenced distance-dependent through-solvent and through-bridge QD-QD couplings	80
Figure 21: Charge influenced QD size-dependent through-solvent and through-bridge QD-QD couplings	83
Figure 22: Band alignment between CdTe and CdSe QDs	95
Figure 23: Schemes of charge transfer network in CdTe-CdSe based solar cell	101
Figure 24: Current-Voltage and Power-Voltage curves.	110
Figure 25: Detailed current-voltage curve near open-circuit voltage.....	111
Figure 26: Solar cell performance comparisons between QD dyad and QD triad based solar cells	113
Figure 27: Effects of mediate QD band edge energies on PCE.....	116
Figure 28: Mediate QD-dependent open-circuit voltage in QD triad systems.....	122
Figure 29: I-U and P-U curves with L QD as light absorber	123
Figure 30: Solar cell performance for QD triad with L QD as light absorber.....	125
Figure 31: Mediate QD energetics influences on PCE for QD triad with L QD as light absorber	126
Figure 32: Mediate QD energetics influences on PCE for QD triad with R QD as absorber	127

Acknowledgements

First, I want to thank my advisor Prof. David N. Beratan for his continuous and professional support of my study and research. He supported me with enormous patience, enthusiasm, insights and knowledge. His guidance over the past few years helped me manage all the difficulties in research and writing this thesis.

Besides my advisor, I want to thank the other members in the committee: Prof. Weitao Yang, Prof. Michael J. Therien and Prof. Jie Liu, for their kind help and comments in the preliminary examination and the thesis defense.

Special thanks go to Dr. Peng Zhang, who helped me solve almost every detailed research problem. Without him, I cannot imagine how I could have finished this degree.

I would like to thank the collaborators Brian P. Bloom and Prof. David H. Waldeck at the University of Pittsburgh.

I thank many colleagues inside and outside the group: Dr. Chaoren Liu, Dr. Zheng Ma, Dr. Jiaying Lin, Dr. Yuqi (Gary) Zhang, Dr. Du Zhang, Dr. Yusong Bai, Dr. Lin Fu, Dr. Nicholas Polizzi, Dr. Chetan Rupakheti, Dr. Alexander Balaeff, Dr. Shahar Keinan, Dr. Aleksey Kuznetsov, Dr. Agostino Migliore, Xuyan Ru, Yujia Zhai, Jesús Valdiviezo, Ye Jin, Lianjun (Ellie) Zheng, Jonathon Yuly and Ben Rousseau for all kinds of helpful and interesting discussions.

This Ph.D. research was supported by DOE grant DE-SC0010662/ER46952.

1. Introduction

Semiconductor nanoparticles/nanocrystals, or quantum dots (QDs) have been widely utilized in many mature and emerging fields such as ultrasensitive biological detecting, labeling and imaging,¹⁻⁴ single-photon turnstile device,^{5,6} multicolor optical coding for biological assays,⁷⁻⁹ and thermoelectric materials and devices.¹⁰⁻¹³ As the world energy consumption and sustainable energy source needs grow,¹⁴⁻¹⁶ QDs are also considered as promising materials for designing and manufacturing third generation photovoltaic (PV)¹⁷⁻²³ and photoelectrochemical (PEC)²⁴⁻²⁶ solar cells.

QDs have many advantages in constructing solar cells, compared to traditional bulk silicon crystals. First, they can be synthesized in simple and less expensive ways.²⁰ Second, the interior of a QD has a higher purity than its bulk counterpart because of QD self-purification function, which drives impurities to the nanoparticle surface.²⁷ PEC cells benefit from a large surface-to-volume ratio that enhances catalysis.²⁶ Lastly, the quantum confinement determines the band gap and energy levels as QD size changes.²⁸⁻³¹ QDs with various sizes and band gaps can be used to capture a wide-range of the ultraviolet and visible spectrum of sunlight.^{23,32} For example, cadmium chalcogenide QDs have size-dependent band gaps that cover the entire ultraviolet and visible spectrum.³³ In addition, QDs can replace the traditional p-n junction. The Piezo-electric effect and the permanent dipole moment in QDs create a large electric field that drives the carriers into desired locations.^{34,35} The band alignment and the deformation potential contribute to a type-II staggered band gap architecture, which can also replace the traditional p-n junction in separating excitons into electrons and holes.³⁶⁻³⁸ Multiple exciton generation are found in

QD solar cells, which allows the peak external photocurrent quantum efficiency to exceed 100%.^{39,40}

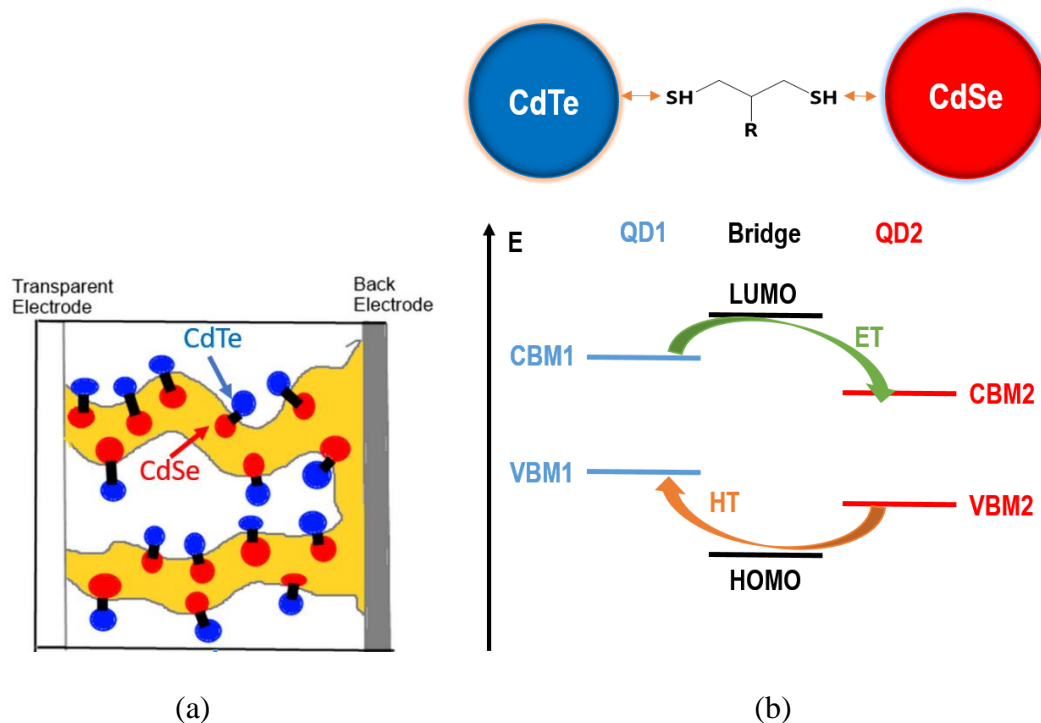
The power conversion efficiency in the current QD based solar cell does not exceed 12%, which is low compared to dye sensitized solar cell (13%)⁴¹ and perovskite solar cell (22.1%).⁴² Using inverted structure designs, i.e., inserting a layer of slightly doped p-type QDs with 1,2-ethanedithiol into the nickel oxide-PbS QD p-n junction, a 9.7 % power conversion efficiency (PCE) has been reached in a PbS colloidal quantum dot solar cell.⁴³ With a solution-based passivation scheme using molecular iodine, a PbS colloidal QD solar cell can reach a certified 9.9% PCE.⁴⁴ In contrast, a Zn-Cu-In-Se QD solar cell reaches 11.6% PCE because the absorption onset is extended to ~ 1000 nm, which generates higher photocurrent than other solar cells.⁴⁵

Charge recombination is a key factor that limits the QD based solar cell PCE.⁴⁶⁻⁵⁰ Large charge recombination rates arise from the high-density surface states. Meanwhile, the charge separation processes are slow because of the weak QD-QD electronic couplings.^{10,51} Molecular ligands like halide,⁴⁴ hydroxyl,⁵² and sulfide^{53,54} are commonly used in experiments to passivate the QD surfaces, so that the surface states are partially eliminated and the charge recombination rates are controlled to low levels. The core-shell structure is another surface passivation strategy to create a shell at the donor-acceptor interfaces in QD assemblies that blocks the charge recombination.⁵⁵⁻⁵⁷ As compared to usual band alignments among the QD donor, ligand barrier and QD acceptor, the cascade band alignment helps to generate higher photocurrent and to slow the charge recombination at the interfaces between different materials.^{43,45,58,59}

The electronic properties of the QDs and charge transfer between QDs have been investigated theoretically and experimentally. The QD band structures and densities of states have been explored with methods from tight-binding model,^{60,61} DFTB semi-empirical methods,^{62,63} and *ab initio* quantum chemistry computation methods.^{54,64,65} These theoretical studies confirm the quantum confinement effects of small sizes QDs and find that the surface states are mostly related to the dangling bond on the QD surfaces. Also, the band edge positions are highly affected by the surface ligands, leading to HOMO pinning phenomena in cadmium chalcogenide QDs.^{54,65} The computed charge transfer time scale in ZnSe/CdS core/shell QD solar cells is ~ 150 fs,⁶⁶ consistent with the charge transfer rates obtained with transient absorption spectrum measurements in core/shell QD solar cells.^{67,68} The QD size-dependent band edge energies and densities of states were attributed to the size-dependent charge transfer rates in the QDs. For a CdSe-TiO₂ solar cell, the electron injection rate from CdSe to TiO₂ QDs measured by transient absorption spectrum is $\sim 10^{10}$ s⁻¹ for 2.4 nm CdSe QDs and decreases rapidly to $\sim 10^7$ s⁻¹ as the QD diameter increases to 7.5 nm.^{17,68}

The experimental and theoretical studies showed that the QD sizes (affect charge separation rates) and the surface passivation conditions (affect charge recombination rates) in the QD assemblies are the most important factors that determine the power conversion efficiencies in QD solar cells. However, the origins of the charge transfer QD size-dependences are poorly understood, which impedes designing novel strategies to overcome the high charge recombination rate. For example, the QD size-dependent electronic

couplings and reorganization energies were not fully considered in calculating the QD size-dependent charge transfer rates.^{17,68}



Scheme 1. (a) CdTe-CdSe dyad based QD solar cells. Two kinds of photoconductive polymers (white and yellow) separate the CdTe (blue) and CdSe (red) QDs. Both the CdTe and CdSe QDs absorb light and generate charge carriers which are then collected by the transparent electrode and back electrode through two different polymers. QDs with various sizes are used to capture the wide range of the visible-IR spectrum of the sun. (b) A CdTe-CdSe dyad unit in (a). The CdTe and CdSe QDs are non-covalently linked by a dithiol bridge. After an electron is photoexcited in the CdTe QD, electron transfer occurs from the CdTe QD conduction band minimum (CBM), through the bridge lowest unoccupied molecular orbital, and to the CdSe QD CBM; after an electron is photoexcited in the CdSe QD, hole transfer occurs from the CdSe QD valence band maximum (VBM), through the bridge highest occupied molecular orbital (HOMO), and to the CdTe QD VBM. The separated charge carriers are further collected by the electrodes in (a).

To have a better understanding of the charge transfer rate, mechanism and their influences on power conversion efficiencies in QD solar cells and hence to provide novel

design strategies in improving the cell performance, we explored theoretically the QD electronic interaction and charge transfer kinetics in QD solar cells. We focus our study on the CdTe-CdSe QD dyad with type-II band edge energy alignment (Scheme 1). Theoretical strategies developed in this thesis can be applied to other QD systems.

The thesis is organized as: in chapters 2 and 3, we focus on the charge transfer properties in the CdTe-CdSe QD dyad; in chapter 4, we focus on the power conversion efficiency of QD solar cells based on QD dyads and triads.

In chapter 2, we discuss the charge transfer kinetics between the CdTe and CdSe quantum dots. The size-dependent electronic properties of these QDs are simulated with a tight-binding Hamiltonian with parameters fitted to experimentally derived data and to computed results using *ab initio* quantum chemistry methods. The dependence of electronic donor-acceptor couplings and charge transfer rates on QD sizes and QD surface-to-surface distance are explored. The charge transfer rates as a function of reaction free energy are discussed to link the charge transfer in QD assemblies to Marcus theory. Moreover, we shall see a mechanism dominance switching between through-space/solvent and through-bond/bridge pathways in the QD-QD charge transfer, as the QD radii and/or the QD surface-to-surface distance increase.

In chapter 3, we investigate the use of external charge to tune the QD-QD electronic couplings and their dependences on QD sizes and the QD surface-to-surface distance. A charged group is introduced into the molecular bridge that links the CdTe and CdSe QDs. The charge influenced D-A couplings are studied using tight-binding Hamiltonians and are explained by the charge induced changes in the effective tunneling barrier, the

donor/acceptor-bridge interactions and the effective tunneling pathway length. The different effects of the bridge charged group on through-solvent and through-bridge couplings are analyzed. Experimental implications of these charge influenced D-A couplings, through-solvent and through-bridge contributions are discussed in the end of the chapter. Moreover, we shall see the mechanism dominance switching between through-space/solvent and through-bond/bridge pathways in the QD-QD charge transfer occurs at smaller (larger) QD sizes when a positively (negatively) charged group replaces the corresponding neutral charge.

In chapter 4, we use the QD size-dependent charge transfer rate obtain in chapter 2 and 3 to explore theoretically the power conversion efficiency in QD solar cells where a QD triad is used as the energy-harvesting and charge-separating engine unit. We hypothesized that use of the QD triad will effectively reduce the charge recombination processes in the QD dyad. We found that the QD triad engine has high solar cell performance when the charge recombination rates are larger or comparable to the charge separation rates. The effects of QD absorber density, band edge offsets among three QDs and QD sizes on the QD triad engine performance are also discussed.

2. Size-dependent electron-transfer kinetics of quantum-dot assemblies

In this chapter, we discuss on the mechanisms of charge transfer between CdTe and CdSe QDs. This collaborative work with Peng Zhang (Duke University), Brian P. Bloom (University of Pittsburgh) and David H. Waldeck (University of Pittsburgh) has been published on *J. Phys. Chem. C*, 2017, 121 (27), pp 14401–14412.

2.1 Introduction to charge transfer in QD assemblies

The size-dependent band gaps of semiconducting nanoparticles (NPs), or quantum dots (QDs), make them useful as tunable light-harvesting structures that can absorb light across the solar spectrum. Because of quantum confinement,^{29,69–77} These features and the convenient solution processability of QDs has led to their use in light-emitting⁷⁸ and light-harvesting devices.^{32,73,79–81} In comparison to the well-known optical bandgap effects, the effect of QD size on the charge transfer characteristics of QD assemblies are less well understood.

Optimization of charge transfer requires a design that promotes the desirable charge transfer separation and inhibits the undesirable recombination pathways. One primary strategy is to create an energy gradient that promotes charge transfer and minimizes recombination. Successful band alignment between electrodes and QDs has been shown experimentally to increase charge separation efficiencies in QD bulk heterojunction architectures,^{77,82–86} and QD-based solar cell efficiencies have reached over 10% by employing band alignment engineering.^{58,59,87–90} The photo-induced charge-transfer

between CdTe and CdSe QD layers depend on the QD size,^{37,74} surface ligands,⁹¹ linkers,^{37,38,74} interfacial charge recombination,^{29,92,93} and QD organization.^{38,88}

The efficiency of type II heterojunction QD solar cells depends strongly on their charge-transfer kinetics,^{73,77,94–96} and the size-dependent charge transfer properties of QDs offer an avenue to manipulate and improve the efficiencies of solar cells.³⁸ Systems with smaller CdTe QDs and larger CdSe QDs have faster inter-QD electron transfer rates than systems with larger CdTe QDs and smaller CdSe QDs. The QD band edge energies for the CdTe and CdSe QDs have a type I alignment when CdSe is small and CdTe is large. The type I alignment makes the ET energy unfavorable ($\Delta_r G > 0$). Thus, the electron transfer rate from a large photo-excited CdTe QD to a small ground CdSe QD is slow compared to rates that would be found for type II band alignment.⁸⁸ Kamat et al.^{18,68,82,97} studied electron transfer (ET) rates between photo-excited CdSe quantum dots and metal oxide nanoparticles, both theoretically and experimentally; and they concluded that the ET rates increased with CdSe QD size because of an increase in the electronic density of states (DOS). Chu et al.⁹⁸ showed that charge transfer rates between Sn₂S₄ linked CdSe QDs depend on the QD size and linker conformations and used linear-scaling density functional theory methods to evaluate electronic and vibronic couplings between QDs. Graff et al.³⁷ examined electron transfer between a CdTe donor QD and CdSe acceptor QDs ranging in size from 2 nm to 4 nm and found that the ET rate increased monotonically with reaction free energy. These studies attribute the size-dependence of electron transfer rates between QDs to the size-dependent band edge energetics (i.e., electronic density of states and reaction free energy effects).

To make predictions of the Marcus ET rate as a function of QD size, requires methods that are qualitatively reliable and affordable for the computation of the key electronic properties (i.e., the QD-QD electronic couplings, band edge energies, and electronic DOS).^{68,98} We use an empirical tight-binding approach as a compromise between cost and reliability. The sp^3s^* tight-binding model^{60,61,99–102} has been widely used to calculate the conduction band minimum (LUMO) energy, valence band maximum (HOMO) energy, and the DOS for CdSe and CdTe QDs as a function of size. The typical sp^3s^* tight-binding models are based on nearest-neighbor Hamiltonians and do not describe through-solvent interactions between non-covalently coupled QD pairs. We introduce a modified tight-binding model that includes both through-solvent (TS) and through-bond (TB) electronic coupling interactions between atoms in the two distinct QDs. These electronic couplings perturb the QD densities of states,^{10,103} but we neglect this effect, assuming weak NP-NP coupling. We validated the approach, by comparisons of computed band-edge energies to experimental values and comparisons of tight-binding electronic DOS to those derived from higher-level theory.

We use this semi-empirical approach to investigate how the QD-QD ET kinetics change with QD size and the nature of the chemical linkers between QDs. We use a tight-binding model to compute size-dependent nonadiabatic ET rates between QDs. The rates are then decomposed into through-bond and through-solvent contributions as a function of QD radius and distance. The analysis finds that QD radius strongly affects the key ET rate parameters, namely the electronic couplings (the relative contributions of through-bond and through-solvent interactions are radius dependent), the QD densities of states, the

reaction free energies, and the ET reorganization energies. Compared to small molecule ET systems, the inverted free energy effects are typically weaker in QD ET systems because the reaction is usually made more exergonic by increasing the acceptor radius, which increases the acceptor density of states and accelerates the ET rate. Taken together, these two effects compensate each other somewhat and the inverted effect can be masked. These studies provide qualitative design principles for tuning the ET kinetics of coupled QD assemblies.

2.2 Charge transfer theory and computational methods to capture charge transfer in QD assemblies

2.2.1 Charge transfer rate equation between two QDs

CdTe QD excited states are generally assumed to undergo rapid internal conversion to the lowest energy excited electronic state (sub-picosecond time scale) and ET time scales are typically much slower (*ps* or longer).^{104–107} Thus, we approximate the ET as proceeding between the LUMO (HOMO) of the electron (hole) donor and unoccupied (occupied) orbital manifold of the electron (hole) acceptor. Further, we assume that the total QD-to-QD ET rate can be written as a sum of independent state-to-state electron transfer rates. The outer sphere reorganization energy λ , depending on the QD radii, for each state-to-state electron transfer rate is assumed to be the same and is approximated by the two-sphere Marcus formula; inner sphere reorganization energy effects are neglected. In this approximation, the overall QD-to-QD ET rate is:^{108–111}

$$k_{et} = \int k(E)\rho(E)dE = \sum_i k_i = \frac{2\pi}{\hbar} \sum_i |V(E_i)|^2 \frac{1}{\sqrt{4\pi\lambda k_B T}} e^{-\frac{(\Delta_r G + \lambda + E_i)^2}{4\lambda k_B T}} \quad (2.1)$$

where $k(E)$ is the electron transfer rate between the LUMO of CdTe and the unoccupied orbitals of CdSe at energy E , $\rho(E)$ is the CdSe density of states (DOS), k_i is the electron transfer rate between the LUMO of CdTe and the i^{th} unoccupied orbital of CdSe with energy E_i (relative to its LUMO energy), and $\Delta_r G$ is the energy difference between the LUMOs of the donor and acceptor. Since our systems are finite, the density of states in eq 2.1 is calculated as a sum over discrete electronic states. The use of eq 2.1 ignores Auger effects, described by Lian, Alivisatos, Prezhdo and others,^{28,112,113} which are found to become important for charge transfer rates in the highly inverted free energy regime.

We use a tight-binding Hamiltonian to compute the electronic structure of the QD assemblies that consist of a donor, acceptor, and bridge. The CdTe and CdSe QDs are modeled by defining a sphere of radius R , with its center at one Cd atom in a zinc blende lattice. Energy levels, densities of states, and electronic couplings between the donor and acceptor for different QD sizes are obtained from the tight-binding model. Because the electronic couplings $V(E_i)$ between the LUMO of CdTe and the low-lying unoccupied orbitals of CdSe were found to be of the same order of magnitude over the energy range relevant to ET, $V(E_i)$ was treated as energy independent and was approximated as the coupling between the LUMOs of CdTe and CdSe. The other ET parameters change as a function of the QD size. Hole transfer from photo-excited CdSe to CdTe occurs in the model between the HOMO of CdSe and the occupied orbitals of CdTe ($\Delta_r G$ for hole transfer is given by the HOMO energy differences). The through-solvent ($V_{DA,s}$) and through-bond ($V_{DA,b}$) contributions to the couplings were each analyzed.

2.2.2 Tight-binding model for QDs electronic structure calculations

Electronic Hamiltonian. The QD assembly includes a donor (D), acceptor (A), and bridge (B) with

$$\hat{H} = \hat{H}_0(D) + \hat{H}_0(B) + \hat{H}_0(A) + \hat{V}_{DB} + \hat{V}_{BA} + \hat{V}_{DA} \quad (2.2)$$

where \hat{H}_0 is the Hamiltonian operator for the isolated donor (D), bridge (B), or acceptor (A) and \hat{V}_{DB} , \hat{V}_{BA} and \hat{V}_{DA} describe the electronic interactions between the components of the assembly. When the QDs are weakly interacting, the limit of interest here, the acceptor DOS in eq 2.2 is well approximated by the DOS of the isolated acceptor. The Hamiltonian for the bridge (B) includes chemical bridging species that bind to the QDs. Interactions mediated by solvent are included in the through-solvent analysis.

Hamiltonians of the fragments. The tight-binding Hamiltonian of an individual QD is

$$\hat{H}_0 = \sum_{i\alpha} E_{i\alpha} |\alpha, i\rangle \langle \alpha, i| + \sum_{i \neq i', \alpha \neq \alpha'} V_{ii', \alpha\alpha'} |\alpha, i\rangle \langle \alpha', i'| \quad (2.3)$$

where $|\alpha, i\rangle$ denotes orbital i on site α and $E_{i\alpha}$ is the corresponding orbital energy. Each atom (site) in a QD is described using two effective orbitals with two electrons. The coupling $V_{ii', \alpha\alpha'}$ between orbitals in eq 2.3 is distance dependent (unless they are on the same atom, in which case the interaction is zero):

$$V_{ii', \alpha\alpha'} = A_{ii'} e^{(-\beta_{ii'} d_{\alpha\alpha'})} \delta_{ii'} (1 - \delta_{\alpha\alpha'}) \quad (2.4)$$

$d_{\alpha\alpha'}$ is the distance between atom α and α' . $A_{ii'}$, $\beta_{ii'}$, and $E_{i\alpha}$ (in eqs 2.3 and 2.4) are determined by fitting the computed CdTe and CdSe QDs band edge energies to experimental values.³³ $E_{i\alpha}$ values are set to previously parameterized s and s^* orbital

energies in the sp^3s^* tight-binding Hamiltonian.^{60,61} The Hamiltonian \hat{H}_0 enables the computation of $\rho(E)$ in eq 2.1. Our simplified tight-binding Hamiltonian is a two-orbital per atom Hamiltonian. Compared to the sp^3s^* model, our simplified tight-binding model parameterizes the through-solvent interactions between QDs, which is required for the following analysis.

Through-solvent QD-QD interactions. The interaction between two QDs is approximated as the sum of the pairwise atomic interactions between the QDs,

$$\hat{V}_{DA} = \sum_{i,\alpha,\alpha'} B_{i,\alpha\alpha'} |\alpha, i\rangle \langle \alpha', i| \quad (2.5)$$

where a and a' atoms (sites) belong to different QDs. $B_{i,\alpha\alpha'}$ is also distance dependent

$$B_{i,\alpha\alpha'} = D_i e^{(-\gamma_i d_{\alpha\alpha'})} \quad (2.6)$$

where $i = 0, 1$ represents s and s^* orbitals respectively; $d_{i,\alpha\alpha'}$ is the distance between atom a of the donor CdTe and atom α' of the acceptor CdSe, and D_i and γ_i are parameterized using DFT analysis of QD-QD through-solvent electronic couplings (see below). This model does not explicitly account for the coupling through the organic molecular layer, which may depend on geometry¹¹⁴ and energy.^{115,116} The model reflects the influence of the organic layer through the decay parameter γ_i .

Through-solvent coupling and tight-binding parameter fitting. The through-solvent contribution to the electronic coupling (eq S1) between D and A QDs is denoted as

$V_{DA,s}$,

$$V_{DA,s} = \langle \varphi_D | \hat{V}_{DA} | \varphi_A \rangle \quad (2.7)$$

where φ_D and φ_A are the eigenstates of the isolated QDs. For electron transfer, we compute $V_{DA,s}$ using the LUMOs of the donor and the acceptor. The interaction between the HOMOs describes the hole transfer coupling.

The through-solvent coupling is computed using block-diagonalization (BD) based on the Kohn-Sham matrix of density functional theory (DFT).¹¹⁷⁻¹¹⁹ Although we are focused on the through-solvent coupling, our analysis begins with a model of the full D-B-A system. D-B-A is broken into three components: a dithiol molecule is used as the bridge (B), the donor (D) is a CdTe QD, and the acceptor (A) is a CdSe QD. DFT calculation of the D-B-A system produces the Kohn-Sham matrix F^0 , which is orthogonalized using the overlap matrix S :

$$F = S^{-1/2} F^0 S^{-1/2} \quad (2.8)$$

F is then partitioned into D, B, and A blocks:

$$F = \begin{pmatrix} F_{DD} & F_{DB} & F_{DA} \\ F_{BD} & F_{BB} & F_{BA} \\ F_{AD} & F_{AB} & F_{AA} \end{pmatrix} \quad (2.9)$$

The diagonal blocks are each diagonalized,

$$U_{XX}^{-1} F_{XX} U_{XX} = E_X \quad (2.10)$$

where $X = D, B,$ and A . The composite matrix that transforms from adiabatic to diabatic states is

$$T = \begin{pmatrix} U_{DD} & 0 & 0 \\ 0 & U_{BB} & 0 \\ 0 & 0 & U_{AA} \end{pmatrix} \quad (2.11)$$

The matrix F is transformed to:

$$T^{-1}FT = \begin{pmatrix} E_{DD} & U_{DD}^{-1}F_{DB}U_{BB} & U_{DD}^{-1}F_{DA}U_{AA} \\ U_{BB}^{-1}F_{BD}U_{DD} & E_{BB} & U_{BB}^{-1}F_{BA}U_{AA} \\ U_{AA}^{-1}F_{AD}U_{DD} & U_{AA}^{-1}F_{AB}U_{BB} & E_{AA} \end{pmatrix} \quad (2.12)$$

The through-solvent coupling between the D and A is:

$$V_{DA,s} = U_{DD}^{-1}F_{DA}U_{AA} \quad (2.13)$$

For molecular orbital m on D (e.g., the LUMO of CdTe) and molecular orbital n on A (e.g., the LUMO of CdSe), the electronic coupling is $V_{DA,s}(m, n)$, and we use it to fit the parameters in eq 2.6 that describe the through-solvent DA interaction. We first perform B3LYP/lan2dz calculations on the $\text{Cd}_{33}\text{Te}_{33}\text{-SH}(\text{CH}_2)_x\text{SH-Cd}_{33}\text{Se}_{33}$ systems as a function of x and derive the electronic couplings using eq 2.12. The distance dependent through-solvent electronic couplings for $\text{Cd}_{33}\text{Te}_{33}\text{-Cd}_{33}\text{Se}_{33}$ systems, with the same edge-to-edge distances as in the linked $\text{Cd}_{33}\text{Te}_{33}\text{-SH}(\text{CH}_2)_x\text{SH-Cd}_{33}\text{Se}_{33}$ systems, calculated with eq 2.4 are fit to the couplings obtained from eq 2.12 (using a nonlinear least squares fitting scheme). Since the through-solvent interactions between two QDs arise mainly (>94%) from the surface atoms in the nearest “hemisphere”, we expect that the through-solvent coupling parameters fit to eq 2.6 for a $\text{Cd}_{33}\text{Te}_{33}$ and $\text{Cd}_{33}\text{Se}_{33}$ QD pair can be used for larger QD pairs. Note that dithiol molecules can attach either covalently or noncovalently to the NP.^{37,120,121} For calculational convenience, we noncovalently link the NPs with the bridging molecules, and the D-B and B-A couplings are relatively weak. The general conclusions related to the NP size-dependence of the ET kinetics do not likely depend on this linkage chemistry.

Through-bond electronic couplings. Linked NPs are also coupled by bond-mediated interactions (denoted as $V_{DA,b}$). Second-order perturbation theory describes these couplings^{122,123}

$$V_{DA,b} = \sum_B \frac{V_{DB}V_{BA}}{E-E_B} \quad (2.14)$$

where E is the electron or hole tunneling energy, approximated by the average energy of the donor and acceptor molecular orbital energy and E_B is the energy of the effective bridge (dithiol) molecular orbital, which is offset by ~ 3 eV compared to E (changes to this offset energy on the scale of 1 eV will not change our qualitative conclusions). The bridge-mediated couplings V_{DB} and V_{BA} are calculated from $V_{DB} = \langle \varphi_D | \hat{V}_{DB} | \varphi_B \rangle$ and $V_{BA} = \langle \varphi_B | \hat{V}_{BA} | \varphi_A \rangle$. One effective bridge orbital is used to describe either electron- or hole-mediated tunneling. The effective bridge molecular orbital is taken to couple only the two nearest Cd atoms on each of the two QDs. Therefore, the through-bond coupling is evaluated using the wavefunction coefficients of these two Cd surface atoms that bind to the bridging molecule,

$$V_{DA,b} = \frac{\xi C_D C_A}{E-E_B} \quad (2.15)$$

where C_D and C_A are the atomic coefficients of the Cd atoms that bind to the bridge. The amplitude of the Cd wavefunction coefficient is strongly influenced by the QD structure, including its size. The parameter ξ is different for electron and hole mediated tunneling and accounts for the manifold of either bridge bonding or bridge anti-bonding molecular orbitals. ξ is parameterized for each of these two manifolds using results of a bridge-

mediated coupling analysis. ζ values are independent of QD size, as long as the bridge molecules are identical in structure.

The D, B, and A states, which are computed using block-diagonalization, are used to compute the bridge-mediated coupling between the Cd₃₃Te₃₃ and Cd₃₃Se₃₃:

$$V_{DA,b} = \sum_B \frac{V_{DB}V_{BA}}{\bar{E} - E_B} \quad (2.16)$$

where V_{DB} and V_{BA} are computed as $V_{DB} = U_{DD}^{-1}F_{DB}U_{BB}$ and $V_{BA} = U_{BB}^{-1}F_{BA}U_{AA}$, respectively.

The summation in eq 2.16 runs over all bridge orbitals. The through-bond coupling between QD-localized diabatic states m and n are $V_{DA,b}(m, n)$. The LUMO-LUMO or HOMO-HOMO through-bond couplings are computed for the Cd₃₃Te₃₃-SH(CH₂)₂SH-Cd₃₃Se₃₃ system to estimate $V_{DA(33),b}$. The wave function coefficients $C_{D(33)}$ and $C_{A(33)}$ for Cd₃₃Te₃₃ and Cd₃₃Se₃₃ QDs are computed from the tight-binding model (eq S1), with the tunneling energy $E_{33} = (E_{D(33)} + E_{A(33)})/2$, so ζ in eq 2.15 is

$$\zeta = \frac{(E_{33} - E_B)V_{DA(33),b}}{C_{D(33)}C_{A(33)}} \quad (2.17)$$

We find that including only the frontier orbitals of the bridge in the coupling calculation is sufficient because the bridge length is short. The effective bridge energy, E_B , is therefore approximated as the energy of the bridge LUMO.

2.2.3 Reorganization energy and reaction free energy for charge transfer between two QDs

The reorganization energy, λ , and reaction free energy are the remaining parameters in eq 2.1. In high-dielectric constant solutions, the outer- sphere reorganization energy dominates λ . The inner sphere contribution is typically tens of meV for semiconducting

QDs,⁹⁸ while the outer sphere λ is usually hundreds of meV,^{97,124} so we neglect the inner sphere contribution in our treatment. We use the Marcus two-sphere model for the outer sphere reorganization energy:¹²⁵

$$\lambda = e^2 \left(\frac{1}{\varepsilon_{op}} - \frac{1}{\varepsilon_s} \right) \left(\frac{1}{2R_D} + \frac{1}{2R_A} - \frac{1}{r_{DA}} \right) \quad (2.18)$$

where ε_{op} and ε_s are the optical and static relative dielectric constants of the solvent, respectively. We set $\varepsilon_{op}=2$ and $\varepsilon_s=15$ (ε_s is ~ 7 for bulk CdTe and CdSe, and the influence of varying ε_s is discussed in section 2.3.5). R_D (R_A) is the radius of the donor (acceptor) QD, and r_{DA} is the center-to-center distance between the QDs.

The reaction free energy difference includes contributions from the electronic energy difference between the QD eigenstates, the difference between the QD-QD Coulomb interaction in the initial and final states, and the entropy difference between initial and final states. The entropy contribution from the QDs to $\Delta_r G$ is assumed to be small because the electron transfer charge is spread over very large QD surface areas. The entropy contribution to the solvation free energy is also neglected because the charge on the QDs in the charge separated state is highly delocalized. The ET reaction free energy is estimated using

$$\Delta_r G_{ET} = E_{CdSe,LUMO} + E_c - E_{CdTe,LUMO} \quad (2.19)$$

where $E_{CdSe,LUMO}$ and $E_{CdTe,LUMO}$ are the LUMO electronic energies of CdSe and CdTe and E_c is the Coulomb energy for the charge-separated state approximated by two point charges at a center to center distance of r_{DA} ,

$$E_c \approx -\frac{1}{\varepsilon_s r_{DA}} \quad (2.20)$$

where the dielectric constant ϵ_s is the same as in eq 2.18, intermediate between the bulk semiconductor and solvent dielectric constants. The free energy difference for hole transfer from the photo-excited CdSe to a ground-state CdTe QD is

$$\Delta_r G_{HT} = E_{CdTe,HOMO} + E_c - E_{CdSe,HOMO} \quad (2.21)$$

where $E_{CdSe,LUMO}$ and $E_{CdTe,LUMO}$ are the electronic energies of the CdSe and CdTe HOMOs.

2.2.4 Parameterization of the tight-binding models for QDs

The parameters in eqs 2.3-2.6 are obtained as described above and listed in Table

1. We check the band edges and DOS of the QDs obtained from this parameter set here.

Table 1: Site energies and orbital coupling atom-to-atom parameters for CdTe and CdSe QDs in eqs 2.3-2.4

Species	CdTe			CdSe		
Parameters	$E_i(\text{eV})$	$A_i(\text{eV})$	$\beta_i(1/\text{\AA})$	$E_i(\text{eV})$	$A_i(\text{eV})$	$\beta_i(1/\text{\AA})$
$i = 0$	-8.89	47.61	1.46	-9.63	52.64	1.57
$i = 1$	-0.59	-5.89	1.02	0.03	-20.58	1.35

*The two orbitals used for each atom. $i = 0$ corresponds to the valence band and $i = 1$ corresponds to the conduction band. (same below)

The CBM energy decreases and the VBM energy increases as the CdTe and CdSe QD sizes grow. The band edge energy positions that are obtained from the tight-binding model for the two different QDs have a type II alignment. These band edge energies are used to estimate the reaction free energy (eqs 2.19 and 2.21).

Size-dependent band edges of CdTe and CdSe QDs. The band edge energies of CdSe and CdTe are known as a function of QD radius.³³ The band edge energies also depend on the linker atom;⁵⁴ here we assume a thiol linker. The parameters A_i , β_i , and $E_{i\alpha}$ shown in Table 1 (eqs 2.3 and 2.4) were computed by fitting the experimental band edge energies (Figure 1). The atomic site energies were chosen as the s and s* orbital energies from the sp^3s^* method. This choice of s and s* energies is not unique, but small changes to these parameters do not significantly alter the band-edge energies and DOS that are derived.

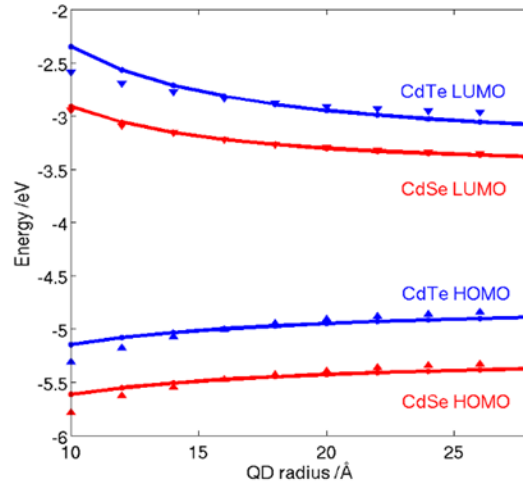


Figure 1: CdTe and CdSe QD band-edge energies as a function of QD size in the tight-binding model (dots) and experimental data (lines);³³

CdSe DOS. The computed CdSe conduction band DOS from the tight-binding model is shown in Figure 2 along with those calculated from the sp^3s^* method. Our tight-binding results approximately reproduce the magnitude and energy dependence of the DOS obtained from the sp^3s^* model near the band edge (-3.4 to -2.4 eV). When the energy is larger than -2.4 eV, our DOS is much smaller than the DOS that is found with the sp^3s^*

method because the p orbitals that produce a higher density of states in the conduction band are absent in the tight-binding model. The LUMO energy of CdSe QDs is ~ 0.39 eV lower than the LUMO energy of CdTe. The CdSe DOS in the energy range from -3.4 eV to -2.4 eV dominates the integral in eq 2.1, and for the energies larger than -2.4 eV, the DOS contributes little to the ET rate. The computed valence band DOS of CdTe (Figure 2 b,c) decreases with energy and increases with the cube of the QD radius. These trends agree qualitatively with the sp^3s^* model and the free-particle model.

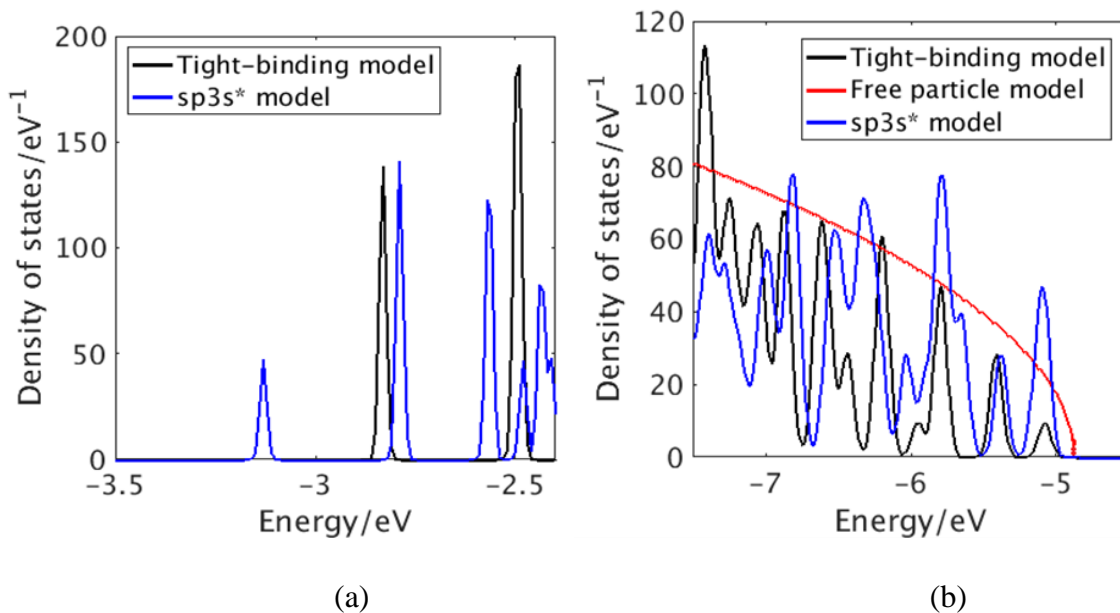


Figure 2: CdTe and CdSe densities of states. (a) CdSe conduction band DOS calculated using our tight-binding model (black) and the sp^3s^* model (blue) with a Gaussian width 0.05 eV; (b) CdTe valence band DOS calculated using our tight-binding model (black), the sp^3s^* model (blue) and effective mass free particle model (red) with a Gaussian width 0.1 eV. The CdSe QD has 15.5 Å radius.

Distance dependent electronic couplings between $Cd_{33}Te_{33}$ and $Cd_{33}Se_3$. The tight-binding parameters for through-solvent and through-bond couplings are fitted to couplings derived from DFT calculations (B3LYP/LANL2DZ for geometry optimization

and B3LYP/LANL2DZdp with ECP for electronic structure calculations) on Cd₃₃Te₃₃–SH(CH₂)_xSH–Cd₃₃Se₃₃ (x=2-7). These dithiols, particularly ethanedithiol (x=2), are commonly used as crosslinkers to increase the conductivities of QD thin films.¹²⁰ The Kohn-Sham matrix for this system is computed at the B3LYP/LAN2DZdp level, which is appropriate for describing Cd₃₃Te₃₃ and Cd₃₃Se₃₃ QD electronic structure.¹²⁶ Through-solvent and through-bond couplings for these systems are obtained using eqs 2.8-2.13 and 2.17.

The computed through-solvent couplings ($V_{DA,s}$) between Cd₃₃Te₃₃ and Cd₃₃Se₃₃, and their dependence on the surface-to-surface distances R_s , are shown in Figure 3. The LUMO-LUMO and HOMO-HOMO couplings decrease approximately exponentially with distance (decay exponent β_s). The β_s values for the LUMO-LUMO and HOMO-HOMO decays are 0.30 Å⁻¹ and 0.51 Å⁻¹, respectively. Assuming an effective mass $m^* = m_e$, tunneling through a one dimensional 3 eV square barrier (typical of QD electron affinity), produces a coupling decay constant of 0.89 Å⁻¹. Our computed β_s values are smaller than this value. This may arise from the reduced effective mass of electrons in semiconductors (0.116 for CdSe and 0.098 for CdTe)¹²⁷ and the polarization of frontier orbitals that arises from interactions with the bridge molecule (influencing both the effective height and shape of the tunneling barrier). The computed through-solvent coupling value is consistent with experimental electron transfer rates between CdTe and CdSe QDs.⁸⁸ The electron transfer rates between 2.5 nm CdTe and 3.5 nm CdSe QDs separated by 1.0 nm are measured to be 10⁹ s⁻¹,⁸⁸ and the associated coupling is estimated to be 10⁻² eV, assuming a reorganization energy of 0.28 eV and a reaction free energy of -0.50 eV based on eq 2.19. Our result for

the LUMO-LUMO coupling between $\text{Cd}_{33}\text{Te}_{33}$ and $\text{Cd}_{33}\text{Se}_{33}$ separated by 10 \AA is $3.27 \times 10^{-3} \text{ eV}$, qualitatively consistent with the experimentally estimated coupling of 10^{-2} eV .³⁷

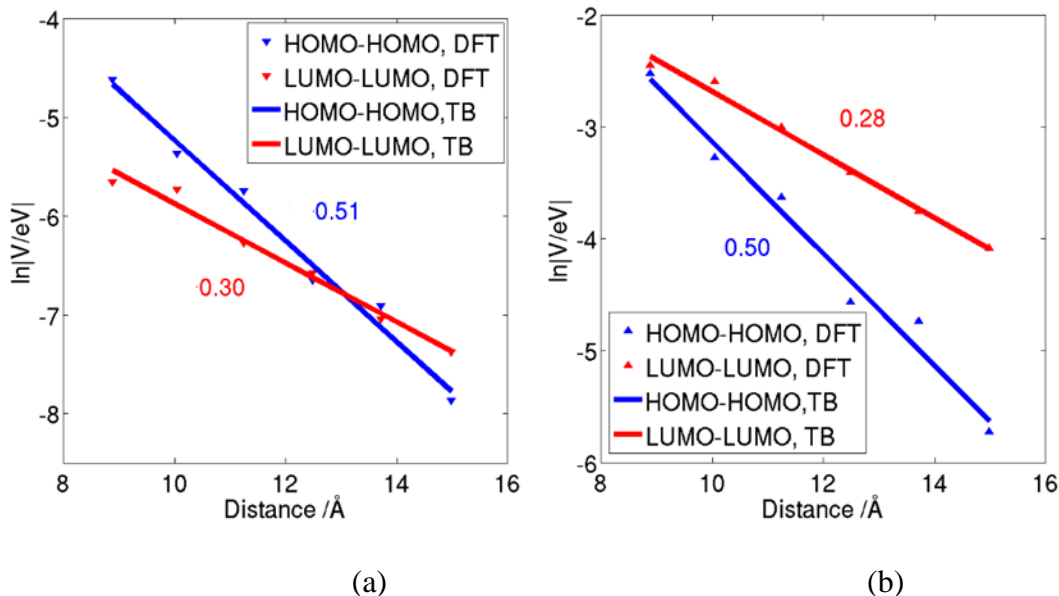


Figure 3: CdTe-CdSe electronic couplings as a function of distance. Through-solvent (a) and through-bond (b) HOMO-HOMO (blue) and LUMO-LUMO (red) couplings between $\text{Cd}_{33}\text{Te}_{33}$ and $\text{Cd}_{33}\text{Se}_{33}$, based on block diagonalization of the Kohn-Sham matrix (DFT in plots) and our tight-binding method (TB in plots). The numbers along the lines indicate the slopes, in units of \AA^{-1} .

The computed through-bond $\text{Cd}_{33}\text{Te}_{33}$ to $\text{Cd}_{33}\text{Se}_{33}$ couplings are shown in Figure 3b. The exponential decay of the coupling with distance is consistent with a bridge-mediated super exchange mechanism. For the $\text{Cd}_{33}\text{Te}_{33}\text{-SH}(\text{CH}_2)_x\text{SH-Cd}_{33}\text{Se}_{33}$ system, we found a through-bond decay exponent of $\beta_b=0.28 \text{ \AA}^{-1}$ (electron-mediated coupling) and $\beta_b=0.50 \text{ \AA}^{-1}$ (hole-mediated coupling). The through-bond coupling decay constant computed with the B3LYP/6-31G(d) analysis is 0.26 \AA^{-1} for an alkyl chain,¹²⁸ similar to the above value. Wang et al. studied ET from CdSe QDs molecularly bridged (by *n*-methylene based $\text{SH-}[\text{CH}_2]_n\text{-COOH}$) to SnO_2 films using optical pump-THz probe

spectroscopy.¹²¹ They found that the coupling decays with bridge length, with $\beta = 0.37 \pm 0.03 \text{ \AA}^{-1}$, in qualitative agreement with our computed β_b value. A recent study of Graff et al. finds a similar coupling decay, β value of 0.27 \AA^{-1} , for CdTe-CdSe QD pairs linked by a hydrocarbon with an amide group in the middle.³⁷ The qualitative consistency between our computed couplings and the couplings drawn from experimental rate data enables us to use the DFT results to fit our tight-binding model.

Fitting the tight-binding through-solvent parameters using DFT. The fitted through-solvent Cd₃₃Te₃₃-to-Cd₃₃Se₃₃ tight-binding coupling parameters (eq 2.6) are shown in Table 2. The values are close to the β_s values because the through-solvent interaction is the sum of atom-atom interactions that originate with similar tunneling barriers. The values derived for this specific system can be used for larger CdTe and CdSe QDs because the main contribution to the through-solvent coupling arises from the interaction between surface atoms on the two facing hemispheres, and the through-solvent tunneling barrier between the two ‘hemispheres’ does not change as the QDs size grows.

Table 2: Through-solvent coupling parameters for CdTe and CdSe QDs in eqs 2.5-2.6

	$D_i(\text{eV})$	$\gamma_i(1/\text{\AA})$
$i=0$	-7.11	0.54
$i=1$	-0.06	0.31

Fitting the tight-binding through-bond parameters using DFT. The through-bond tight-binding scaling parameter is ζ (independent of QD size, eqs 2.15 and 2.17). The ζ value depends on the bridging molecule, and its value drops approximately exponentially with distance. In the ET coupling and rate analysis below, we fix the bridge molecule

(length and chemistry) and change the QDs size (CdTe–SH(CH₂)₂SH–CdSe). For these structures, $\xi = 30 \text{ eV}^2$ (11.2 eV²) for LUMO-LUMO (HOMO-HOMO) couplings.

2.3 Size and dielectric constant dependent electron and hole transfer rates

2.3.1 Size-dependent QD DOS and activation free energy

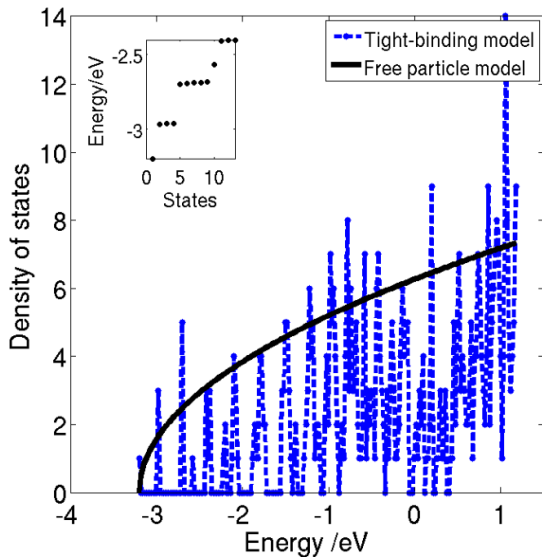
DOS. The DOS computed with our tight-binding method generally increases with the conduction band energy and was compared with the DOS (see Figure 4a) estimated using an electron in a sphere model,⁶⁸ namely

$$\rho(E_p) = V \frac{(2m^*)^{\frac{3}{2}}}{2\pi\hbar^3} \sqrt{E_p} \quad (2.25)$$

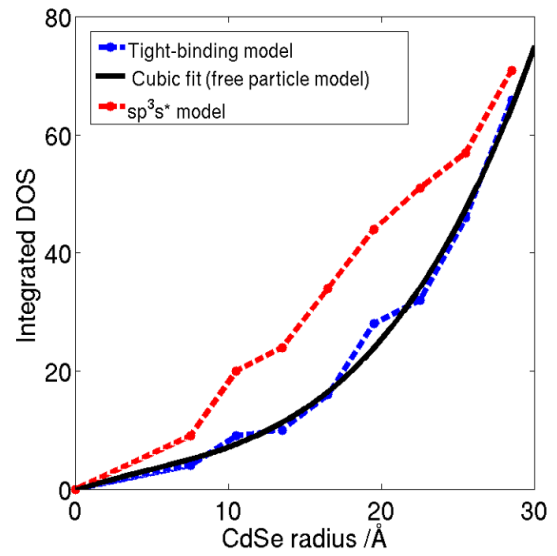
where E_p is the electronic energy for a particle with an effective mass m^* , and V is the volume of the sphere.

The computed DOS of CdSe conduction band is qualitatively consistent with the simple tight-binding model. The fine structure in the DOS spectrum originates from breaking the degeneracy of the first 13 electronic orbitals ((n-1)s (n-1)p nd ns np orbitals, see inset in Figure 4a), which resembles the degeneracy of the orbitals derived from the spherical potential model and from the sp³d⁵s* tight-binding model.^{102,129} At very high energies, the tight-binding models fail; however, this energy regime is not relevant to the ET processes of interest here. Another important characteristic of the DOS (Figures 4b,c) is its dependence on the QD radius. If we integrate the DOS over a 1 eV energy window near the band edge, we find that it appears to increase as the radius R_{CdSe} cubed; i.e., the volume. This dependence is consistent with the DOS in the sp³s* model and the free-particle model.^{102,129} This DOS radius dependence near the band edge indicates that the

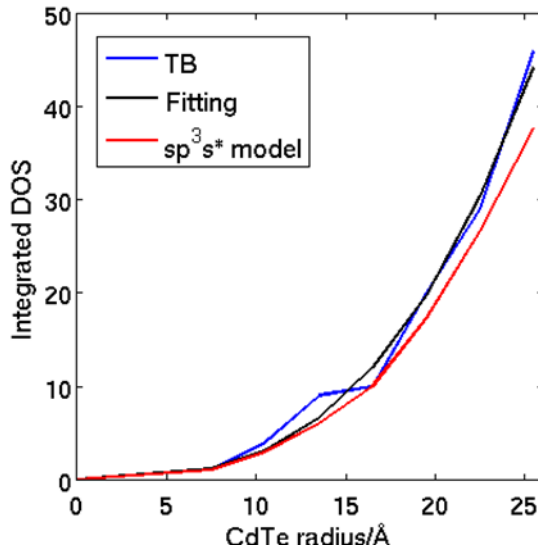
tight-binding model captures the essential features of the QD's electronic structure. We find similar agreement between our computed CdTe valence band DOS and the DOS obtained from the sp^3s^* model and the free-particle model.



(a)



(b)



(c)

Figure 4: CdTe and CdSe QD densities of states as a function of QD sizes. (a) The graph shows the conduction band DOS of CdSe QDs with a 15.5 Å radius calculated using our tight-binding model (blue dotted line, energy bin size of 0.02 eV), spherical potential well model (black solid line), and energy levels of the first 13 electronic states from the tight-binding model (inset). The effective mass for the spherical potential model is 0.12 m_e .¹²⁷ (b) & (c) The plot shows the integrated DOS of CdSe & CdTe QDs as a function of radius in the sp^3s^* model, our model, and cubic fitting. The energy range is from the CdSe LUMO energy to ~1 eV higher;

Activation free energies. The Marcus free energy of activation (for $E_i = 0$ in eq 2.1) is $\Delta G^\ddagger = \frac{(\Delta_r G + \lambda)^2}{4\lambda}$ for LUMO-LUMO (electron) or HOMO-HOMO (hole) transfer. Figures 5a,b show ΔG^\ddagger contours with varying CdSe and CdTe radii. The free energy of activation for ET reaches its smallest value for a QD radius ratio (R_{CdTe}/R_{CdSe}) of ~ 1.8 , however the radius ratio value depends on the electronic structure of the two QDs, the edge-to-edge distance between the QDs, and the dielectric constant (discussed below). In contrast to the molecular case, the acceptor DOS influences the overall charge transfer rate; and the maximum charge transfer rate in these coupled QD systems may not occur when $\Delta G^\ddagger = 0$. The ΔG^\ddagger for hole transfer reaches its smallest value for a QD radius ratio (R_{CdSe}/R_{CdTe}) ~ 2.0 , similar to ET. That is, both HT and ET Franck-Condon factors are the largest when the donor radius is ~ 2 times larger than the acceptor radius. For a fixed donor radius when $|\Delta_r G| > \lambda$ (inverted region), ΔG^\ddagger increases with the acceptor radius for both HT and ET. If charge transfer rates depended only on ΔG^\ddagger , the HT and ET rates vs. the acceptor radius would display a maximum with acceptor size. Note that the QD radius ratio ($R_{donor}/R_{acceptor}$) which produces the charge transfer activation free energy valley in Figure 5a,b depends on the dielectric constant (ϵ_s), since $\Delta_r G$ and λ depend on ϵ_s .

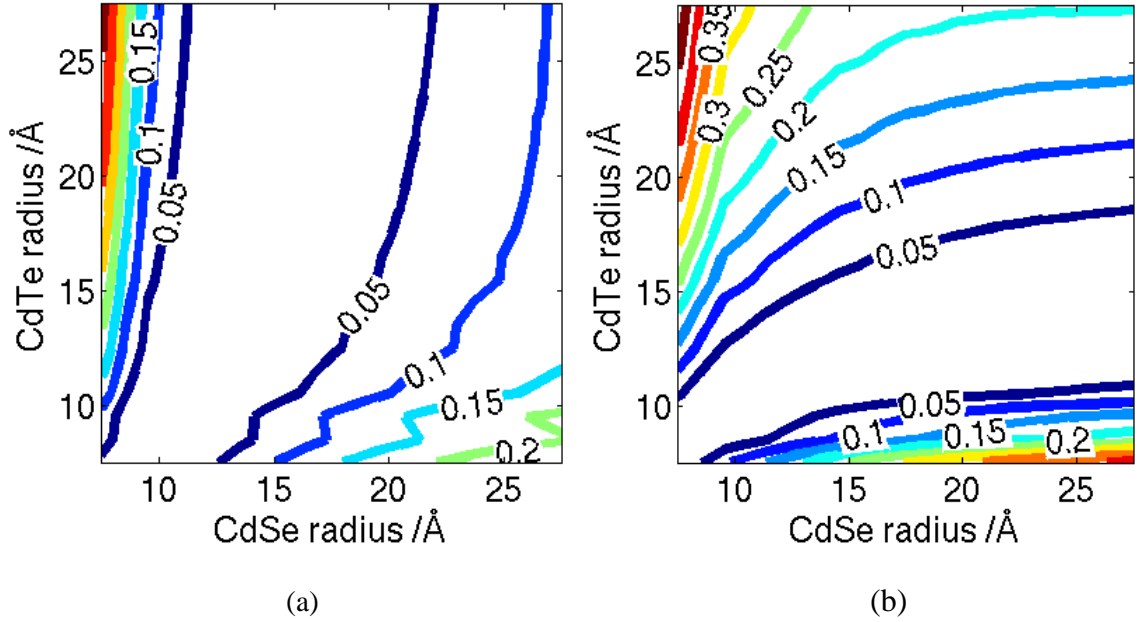


Figure 5: CdTe-CdSe charge transfer reaction free energy contour plots. (a) The Contour plots are shown for the charge transfer Gibbs energy of activation as a function of QD radii for (a) LUMO-LUMO electron transfer; (b) HOMO-HOMO hole transfer

For a CdTe-CdSe coupled QDs with fixed radii, activationless electron and hole transfer cannot be realized simultaneously, because both R_{CdTe}/R_{CdSe} (for electron transfer) and R_{CdSe}/R_{CdTe} (for hole transfer) would need to be larger than one. However, if the band edge energies of the two coupled QDs can be tuned independently (for example, by changing the QD chemical composition), both electron and hole transfer could be tuned into the activationless regime.

2.3.2 Size-dependent TS/TB electronic coupling between QDs

Through-space analysis. We construct a simple model for the dependence of the donor-acceptor coupling on the QD radii, including the influence on through-bond and through-space interactions. Donor and acceptor electronic states are each assumed to be

localized on one of the QDs and to be delocalized predominantly on the surface atoms, consistent with findings of a DFTB (density functional based tight binding) analysis of CdTe and CdSe QDs.^{58,130} The through-space coupling between QDs of radii r_1 and r_2 is calculated by summing over all pairwise interatomic interactions, v_{ij} , with distance, d_{ij} , between the atoms. The interaction v_{ij} is assumed to decay exponentially with distance, such that $v_{ij} = c_s \frac{1}{\sqrt{N_D}} \frac{1}{\sqrt{N_A}} e^{-\gamma_s d_{ij}}$, where c_s is a constant with units of energy, γ_s describes the electron tunneling decay between QDs, and N_D and N_A are the number of surface atoms on the donor and acceptor, respectively. The two QDs are centered (in Cartesian coordinates) at $(0, 0, -r_1 - a)$ and $(0, 0, r_2 + a)$, and $2a$ is the edge-to-edge distance between them. Using polar coordinates (see Figure 6), the through-space coupling (where $r_i = r_1$, $r_j = r_2$) is

$$\begin{aligned}
J_{DA,s} &= \frac{N_D}{4\pi r_1^2} \frac{N_A}{4\pi r_2^2} \int_0^\pi \int_0^\pi \int_0^{2\pi} \int_0^{2\pi} r_i \sin\theta_i r_j \sin\theta_j v_{ij} d\varphi_i d\varphi_j d\theta_i d\theta_j \\
&= \frac{c_s \sqrt{N_D N_A}}{16\pi^2 r_1 r_2} \int_0^\pi \int_0^\pi \int_0^{2\pi} \int_0^{2\pi} \sin\theta_i \sin\theta_j e^{-\gamma_s d_{ij}} d\varphi_i d\varphi_j d\theta_i d\theta_j
\end{aligned} \tag{2.23}$$

The distance d_{ij} is

$$d_{ij} = \sqrt{(r_j \sin\theta_j \cos\varphi_j - r_i \sin\theta_i \cos\varphi_i)^2 + (r_j \sin\theta_j \sin\varphi_j - r_i \sin\theta_i \sin\varphi_i)^2 + (r_i \cos\theta_i - r_j \cos\theta_j + 2a)^2} \tag{2.24}$$

The TS coupling $J_{DA,s}$ is approximately exponential in the distance between the QDs. More than 90% of the QD-QD coupling arises from the hemispheres of QD atoms that face each other (for QDs with radii $> 17.5 \text{ \AA}$, $\gamma_s = 0.44 \text{ \AA}^{-1}$ (fitted from DFT

computed couplings between $\text{Cd}_{33}\text{Te}_{33}$ and $\text{Cd}_{33}\text{Se}_{33}$; see Sec. 2.2.3), and edge-to-edge distances $> 8 \text{ \AA}$.

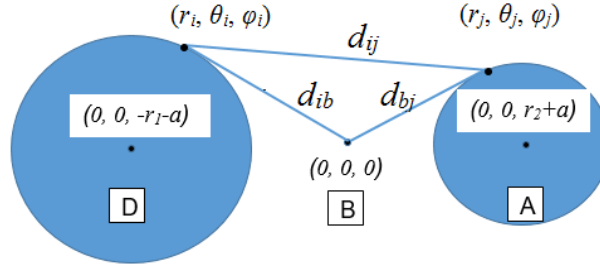


Figure 6: The geometrical model of charge transfer couplings between two spherical QDs. The z-axis joins the QD centers. One effective bridge orbital appears at the origin.

The tight-binding model is used to investigate the size-dependent through-space couplings for $\text{CdTe-S-(CH}_2)_2\text{-S-CdSe}$. Figure 7a shows the dependence of the through-space couplings on the QD radius, as derived from the simple geometrical analysis (black, eq 2.21) and from the tight-binding model (red, blue). The LUMO-LUMO and HOMO-HOMO couplings are qualitatively consistent with one another and are determined, in part, by the atom-to-atom through-space interaction distance decay constant β_s . As the QD size increases, the through-space couplings decrease. The through-space couplings for radii $< 10 \text{ \AA}$ are typically one order of magnitude larger than the couplings for radii $> 20 \text{ \AA}$. For fixed edge-to-edge distances, the QD center-to-center distance grows with QD radius and as a result the wavefunction amplitude for each individual surface atom decreases. The approximate amplitude on a surface atom scales with $1/\sqrt{N}$, where N is the total number of surface atoms; thus the coupling between two QDs is expected to decrease as $1/R$, where R is the QD radius. Deviations from a simple $1/R$ dependence (for QD radii from 7.5 \AA -

9.5 Å) likely arises from the non-spherical structure of the QDs and the spreading of amplitude into the NP core. Note, that Figures 7a,b show plots of $\ln(V \cdot R)$ versus R , and the range along the vertical axis are different between the two graphs. The differences between the tight-binding model and the geometrical analysis arise from the non-spherical shape of finite size QDs and the additional non-surface atomic interactions of the QDs in the tight-binding model. The through-solvent (through bond) couplings are within a factor of 2 - 3 (~ 7) of the constant potential model over the entire range.

Through-bond analysis. The second-order coupling between atoms on different QDs mediated by one bridge orbital is $w_{ij} = \frac{v_{ib}v_{bj}}{\epsilon - \epsilon_b}$ where ϵ and ϵ_b are tunneling and bridge energies, respectively. In analogy with the through-solvent analysis, we write $v_{ib} = c_b \frac{1}{\sqrt{N_D}} e^{-\gamma_b d_{ib}}$ and $v_{bj} = c_b \frac{1}{\sqrt{N_A}} e^{-\gamma_b d_{bj}}$; where c_b is a constant with units of energy, and γ_b is the decay of the pairwise interaction between a QD atom and a bridge site ($\gamma_b = 1.53 \text{ \AA}^{-1}$ is chosen to reproduce the size-dependent dot-to-dot through-bond coupling derived from the tight-binding analysis). d_{ib} and d_{bj} are the distances between the bridge site and the surface atoms on the QDs, calculated similarly with eq 2.24. The through-bond coupling is similar to eq 2.23, but with the bridge mediated w_{ij} ; and thus the distance d_{ij} replaced with $(d_{ib} + d_{bj})$ and γ_s replaced by γ_b . Note that d_{ij} and $(d_{ib} + d_{bj})$ can be viewed as effective through-space and the through-bond tunneling distances, respectively, for the two QDs. The d_{ij} values represents the through-solvent tunneling distance, independent of the ligand length. The through-bridge tunneling pathway distance is determined by the length of the organic bridging molecules, which is encoded in the values of d_{ib} and d_{bj} .

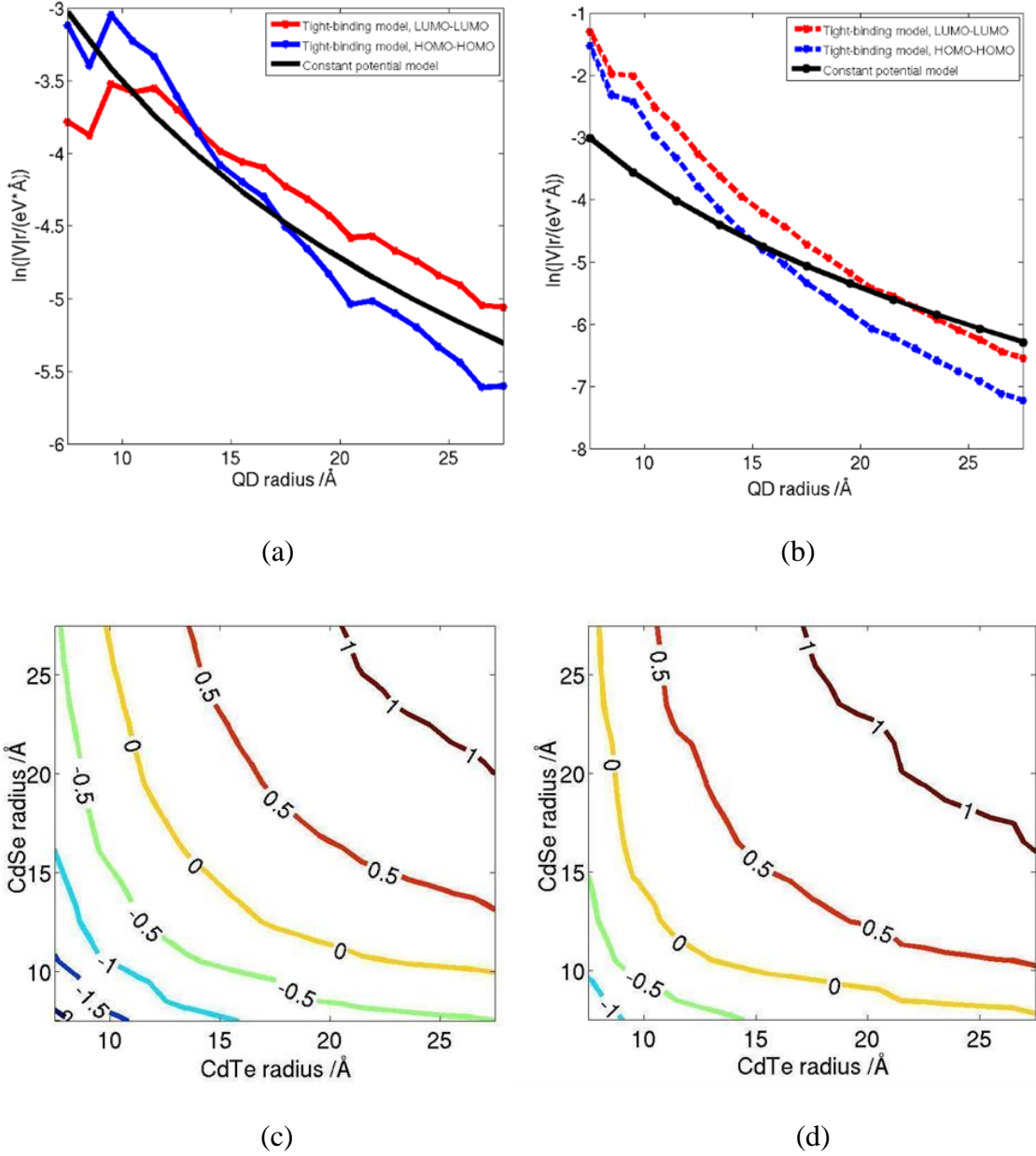


Figure 7: CdTe-CdSe charge transfer couplings as a function of QD sizes. Panels (a) and (b) show the size-dependence of the through-space (a) and through-bond (b) couplings between spherical QDs in the constant potential model (black line) and the HOMO-HOMO (blue dotted line) and LUMO-LUMO (red dotted line) couplings in the tight-binding model; the surface-to-surface distance, a , is 8.9 \AA , similar to the length of an extended ethanedithiol linker. Here, β_s is 1.0 \AA^{-1} and β_b is 1.5 \AA^{-1} (Sec. II.). Panel (c) shows $\log(\text{TS coupling}) - \log(\text{TB coupling})$ between LUMOs of the QDs, for various NP size combinations, and panel (d) shows the same as part (c)

for the HOMO couplings between QDs. $\log(\text{TS coupling}) - \log(\text{TB coupling})$ is approximately a function of the QD radius product $R_{\text{CdTe}} \times R_{\text{CdSe}}$.

The tight-binding model is also used to investigate the size-dependent through-bond couplings for CdTe–S-(CH₂)₂-S–CdSe. The bridge molecule creates coupling pathways for super exchange between the two QDs. Figure 7b shows the computed through-bond couplings using both the geometrical and the tight-binding analysis. The through-bond coupling, like the through-space coupling, decreases with increasing QD radius. Note that the through-bond couplings deviate more strongly from the constant potential model (solid black line) than do those for the through-space case. For through-solvent couplings, all atoms are used in the tight-binding model; for through-bond couplings, only two atoms near the bridge are considered. However, in our constant potential model, all surface atoms are considered.

Comparison of through-space and through-bond couplings. Two differences between through-space and through-bond couplings in Figure 7 are noteworthy. First, the deviation from a $1/R$ dependence of the coupling's pre-exponential factor in the small radius limit is greater for through-space than for through-bond tunneling. This is reflected as the unsmooth curves for the couplings from the tight-binding model. This deviation arises because of the greater number of surface atoms involved in the through-space coupling as compared to the through-bond coupling. Second, the through-space couplings decrease more slowly with QD radius than the through-bond couplings (for fixed edge-to-edge QD distances). This occurs because the through-bond tunneling distance $d_{ib} + d_{bj}$ increases more rapidly with QD radius than the effective through-space tunneling distance

d_{ij} (see Figure 7 and eq 2.23). Contour plots of the logarithmic difference between through-space and through-bond couplings (see Figures 7c,d) indicate that the QD radius combination producing a constant coupling difference occurs when the product $R_{CdTe} \times R_{CdSe}$ is approximately constant. When the through-bond and through-space couplings are equal, $R_{CdTe} \times R_{CdSe} = 225 \text{ \AA}^2$ (126 \AA^2) for the LUMO-LUMO (HOMO-HOMO) coupling. Dominance of through-space or through-bond coupling is therefore indicated by the value of $R_{CdTe} \times R_{CdSe}$, which can be controlled experimentally.

2.3.3 Size-dependent electron transfer rates

Charge transfer rates are computed using eq 2.1 with the coherent sum of the couplings $V_{DA} = V_{DA,s} + V_{DA,b}$. We decompose the charge transfer rates into three terms, proportional to $V_{DA,s}^2$, $V_{DA,b}^2$, and the interference term $2V_{DA,s}V_{DA,b}$. We define the $V_{DA,s}^2$ and $V_{DA,b}^2$ dependent terms in eq 2.1 as the through-space and the through-bond contributions to the rate, respectively. This separation is useful when either the through-bond or the through-space coupling dominates the donor-acceptor interaction. Figure 8 shows the computed through-space (panel a) and through-bond (panel b) electron transfer rates as a function of acceptor radius (eq 2.1) using DOS, coupling, reorganization energy, and free energy differences.

Through-space ET rates. Figure 8a shows the rates computed for photoinduced ET from CdTe to CdSe as R_{CdSe} increases from 7.5 \AA to 27.5 \AA , for five different CdTe QD radii. Although the electronic coupling between CdTe and CdSe decreases as R_{CdSe} increases, the increase in the CdSe DOS and the increasing reaction driving force lead to

an increase in the electron transfer rate with CdSe size. Note also, that the ET rates increase as the CdTe radius (R_{CdTe}) decreases for all CdSe QDs. For small CdTe QD radii (< 12.5 Å), the computed ET rates range from $4.5 \times 10^{10} \text{ s}^{-1}$ to $6.7 \times 10^{11} \text{ s}^{-1}$, consistent with the experimental ET rates.^{68,88} The rate computed for ET from a small CdTe QD ($R_{CdTe} = 13.5$ Å) to a large CdSe QD ($R_{CdSe} = 27.5$ Å) is $2.7 \times 10^{11} \text{ s}^{-1}$, in close agreement with the experimentally derived ET rates ($1.2 - 2.8 \times 10^{11} \text{ s}^{-1}$) for a small donor CdSe QD ($R_{CdSe} = 14.0$ Å) to metal oxide NPs.¹³¹ The rate computed for ET from a small CdTe QD ($R_{CdTe} = 6.5$ Å) to a large CdSe QD ($R_{CdSe} = 27.5$ Å) is $9.9 \times 10^{11} \text{ s}^{-1}$ in the tight-binding analysis, comparable to the ET rate derived from first principles DFT simulations ($6.3 \times 10^{12} \text{ s}^{-1}$) for ET between a radius 6.5 Å QD and a TiO₂ nanobelt.¹⁰⁶

An increase in the ET rates can arise either from an increase in the acceptor DOS or from changes in ΔG^\ddagger . We found that the CdSe DOS increases approximately with the QD radius cubed (Figure 4b,c). As R_{CdSe} changes from 7.5 Å to 27.5 Å for $R_{CdTe} = 7.5$ Å, the ΔG^\ddagger changes from 0.04 eV in the normal regime to 0.23 eV in the inverted regime. The reorganization energy of the CdTe-CdSe pair changes from 0.64 eV to 0.44 eV, and the LUMO-LUMO energy difference changes from -0.32 eV to -1.08 eV. This reorganization energy is consistent with typical values reported in the literature.^{18,98} The rapid decrease in the LUMO-LUMO energy offset and the slow variation of the reorganization energy with the CdSe radius causes the ET process to change from the normal to the inverted free energy regime; however, a rate maximum was not found in the computed ET rates because the DOS grows rapidly as R_{CdSe} increases, which tends to increase the rate with R_{CdSe} . The lower coupling as a function of QD radius and the increased activation free energy in the

inverted regime, are both more than compensated by the growing electronic DOS with R_{CdSe} . Figures 2, 4a, 7b show that the computed DOS does not uniformly increase with energy and the LUMO-LUMO coupling's pre-exponential factor does not have a pure I/R dependence (as discussed above). Taken together, these two effects cause small variations in the dependence of the ET rates on R_{CdSe} , displayed in Figure 8a. ET rates for $7.5 \text{ \AA} < R_{CdTe} < 27.5 \text{ \AA}$ show a similar R_{CdSe} dependence.

The ET rate decreases as R_{CdTe} increases for all R_{CdSe} sizes because of the decrease in electronic coupling and the decrease in reaction free energy change associated with the shift in the CdTe's LUMO energy. For a fixed R_{CdSe} , the tunneling energy for ET is set by the LUMO energy of the CdTe QD, which decreases as the radius increases, and the CdSe DOS at the CdTe (LUMO) tunneling energy also decreases as the CdTe size increases. The decreasing DOS and coupling as a function of R_{CdTe} causes a subsequent decrease in the ET rates; the ET rates from a photo-excited CdTe QD to a 7.5 \AA CdSe QD decrease from 10^{11} s^{-1} to 10^4 s^{-1} as R_{CdTe} increases from 7.5 \AA to 27.5 \AA . Note that the recombination rate for the QDs is typically of order 10^8 to 10^7 s^{-1} , which precludes efficient ET at rates below 10^8 s^{-1} .

In summary, the ET rate increases with R_{CdSe} because the DOS of CdSe increases with the CdSe radius. The growth in the CdSe DOS itself increases the ET rates, and this effect dominates all other effects (namely coupling and activation free energy changes), which tend to decrease the ET rate as R_{CdSe} increases. In addition, the ET rate decreases as the CdTe radius increases because its LUMO shifts to lower energy and accesses a smaller

CdSe DOS. As the CdTe radius increases, the electronic coupling drops and the ET rate slows.

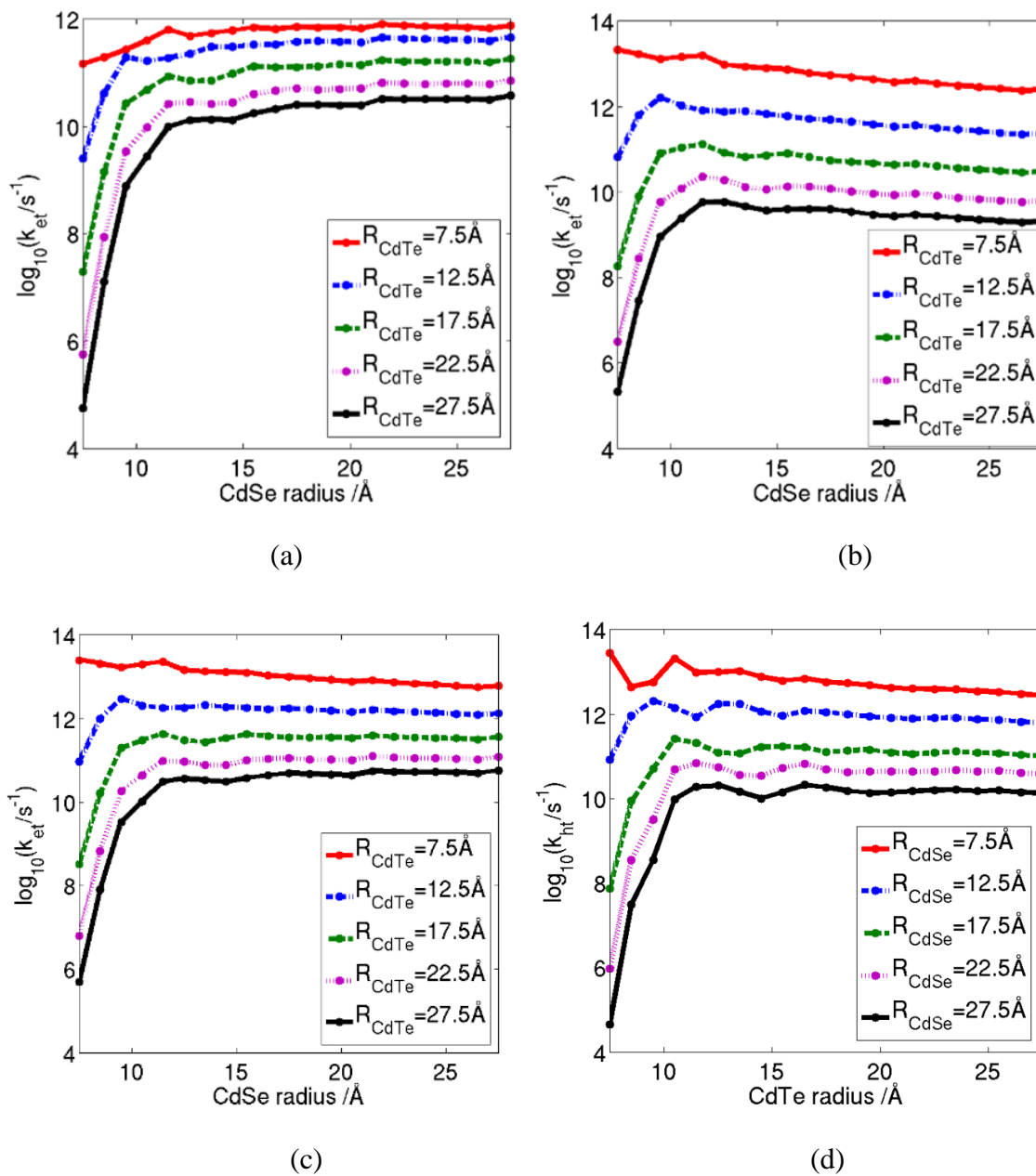


Figure 8: QD-QD charge transfer rates as a function of QD sizes. Computed through-space ET (a), through-bond ET (b), total electron (c) and total hole (d) transfer rates between CdTe and CdSe QDs are plotted as a function of the acceptor QD

radius for different sizes of the donor QD - based on eq 2.1. The solvent dielectric constant is 20. ET and HT rates increases as the charge donor radius decreases, but they may increase or decrease with the acceptor radius depending on the donor radius.

Through-bond ET rates. Figure 8b shows ET rates computed for photoinduced ET from CdTe to CdSe by way of a through-bond coupling mechanism as a function of R_{CdSe} for five CdTe radii. As the acceptor CdSe QD radius increases from 7.5 Å to 27.5 Å, an ET rate maximum (at R_{CdSe}^*) appears for all R_{CdTe} sizes. The positions of the maxima shift to larger CdSe radii as R_{CdTe} increases, following the approximate line $R_{CdSe}^* = 0.21 \times R_{CdTe} + 8.0$. For small acceptor QDs (7.5 Å), the computed through-bond ET rate changes over eight orders of magnitude as the donor QD size changes from 7.5 Å to 27.5 Å and the reaction free energy changes from negative to positive. The appearance of the rate maximum occurs because the through-bond LUMO-LUMO coupling decreases more rapidly than the CdSe conduction band DOS grows with increasing R_{CdSe} (similar to the through-space dependence of ET rates on QD size).

The predicted difference between through-bond and through-space ET rates arises from the competition between the decrease in the through-bond coupling and the increase in the DOS as a function of R_{CdSe} . For larger CdSe QDs, the QD conduction band DOS increases and the through-space and through-bond LUMO-LUMO couplings decrease with increasing CdSe size. The through-bond LUMO-LUMO coupling decays more rapidly than the through-space LUMO-LUMO coupling as R_{CdSe} increases. The decrease in through-bond coupling is rapid enough to compensate for the increasing DOS with R_{CdSe} ,

making it possible to observe the activation free energy effects on the computed rates, *vide infra*.

Overall electron transfer rates. The overall electron transfer rates were computed using the coupling evaluated as the coherent sum of the through-space and through-bond coupling contributions. Figures 8c and 8d show how the rates change with acceptor size. For all acceptor radii, the charge transfer rates decrease as the donor size increases, because the through-space ($V_{DA,s}^2$) and through-bond ($V_{DA,b}^2$) couplings decrease with the donor size, as discussed above. However, the ET and HT rate changes have different acceptor size dependencies for different donor radii. The ET rate changes show three distinct dependences as the acceptor radius grows: (1) the ET rate increases for donor radii (R_{CdTe}) $> \sim 17.5 \text{ \AA}$; (2) the ET rate decreases for donor radii (R_{CdTe}) $< \sim 8.5 \text{ \AA}$; and (3) the ET rate displays a maximum when the donor radius is in the range of $8.5 - 17.5 \text{ \AA}$. As the acceptor radius increases from 7.5 \AA to 27.5 \AA for hole transfer, the rates (i) decrease if the donor radius is small ($R_{CdSe} < \sim 9.5 \text{ \AA}$) and (ii) show a maximum if the donor radius is large ($R_{CdSe} > \sim 9.5 \text{ \AA}$).

For small donor QDs, the HT and ET rate variations with respect to the acceptor radius are dominated largely by changes in the reaction free energy and coupling (the DOS variation effect on the charge transfer rate is small compared to those effects from the changes in the reaction free energy and coupling). This is because, for type II QD architectures, the energy gap E ($E > 0$) between donor and acceptor band edges is large for small donor QDs and the charge transfer process is in the inverted region ($\Delta_r G = -E + E_C$, eqs 2.20 and 2.21), where the charge transfer rate decreases with the increase in the energy

gap E (caused by the increase in the acceptor QD radius). The electronic couplings for hole transfer and ET (and consequently the hole transfer and ET rates) also decrease with increasing acceptor size, for small donor radii. Conversely, for large donor QDs, the HT and ET rates increase with an increase in the acceptor QD size. This is because the large increase in the DOS with an increasing acceptor radius dominates the HT and ET rates more than the decrease in rate caused by a decrease in coupling. Also, the charge transfer process is mostly in normal region, where the ET rate increases with the increase in energy gap E or the acceptor QD radius.

In the small QD size regime, the through-space and through-bond interference is relatively strong because they have similar values (the magnitude of the TS and TB cross-term $V_{DA,s}V_{DA,b}$ is comparable to the magnitude of the individual TS or TB couplings). The total charge transfer rates always decrease as the acceptor radius increases, in contrast to the through-space and through-bond rates where a rate maximum *versus* acceptor radius is observed. The comparison of through-space and through-bond couplings is discussed in Sec. 2.3.2 (Figure 7). In the regime where through-space and through-bond couplings are of similar size, both contribute to the rate, and our calculations show that the overall charge transfer rate is smaller than the incoherent sum of the rates that arise from through-space and through-bond channels alone, indicating destructive interference. Therefore, the charge transfer rate decreases as the acceptor radius grows.

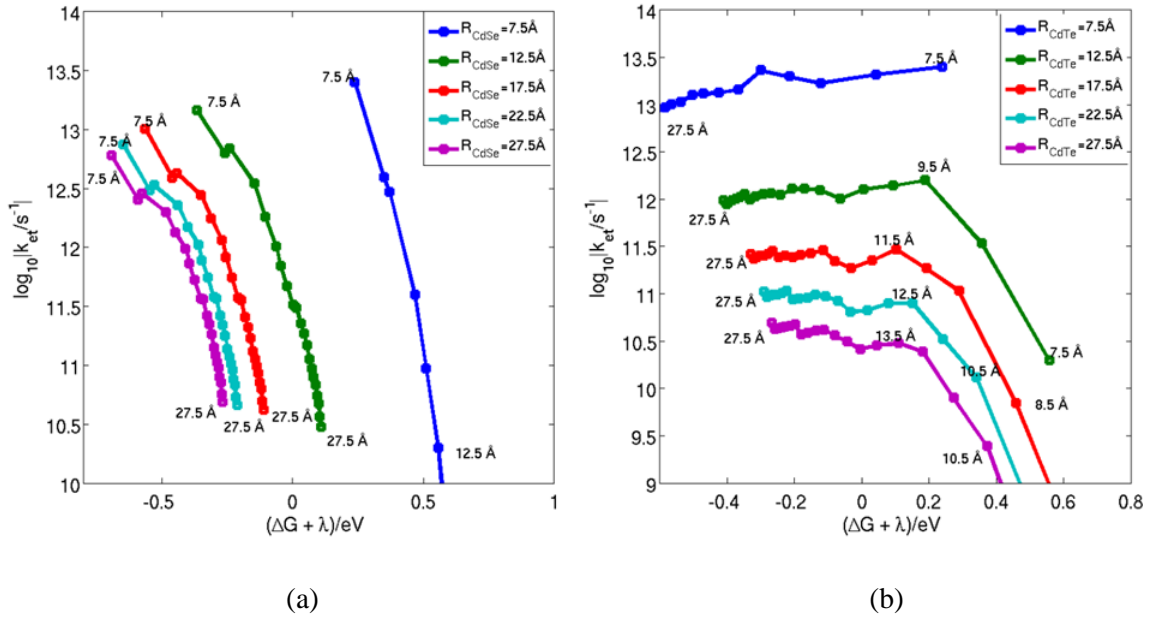


Figure 9: QD-QD charge transfer rates as a function of $\Delta_rG+\lambda$ with fixed acceptor (a) and donor (b) radii. The numbers on the lines indicate the radii of the QD, which determines the value of $\Delta_rG+\lambda$.

ET Rates as a function of $\Delta_rG+\lambda$. In the two-state Marcus theory, the charge transfer mechanism changes from the normal to the inverted regime when $\Delta_rG+\lambda$ changes sign. The total ET rates (eq 2.1) as a function of $\Delta_rG+\lambda$ are shown in Figure 9. Note that all the ET parameters (reaction free energy, reorganization energy and donor-acceptor coupling) are all radius dependent. ET rates drop rapidly as $\Delta_rG+\lambda$ increases when the acceptor radius is fixed (Figure 9a). This is because the donor-acceptor electronic coupling and the acceptor DOS near the corresponding donor LUMO energy position decreases with the increase in the donor radius. In these ET systems, a transition from the normal to the inverted regime displays only a modest decrease in the ET rates, and only in some instances when the donor radius is fixed (Figure 9b). For example, if R_{CdTe} is fixed at 12.5 Å, the rate goes through a maximum for positive $\Delta_rG+\lambda$. The coupling's change with QD size has

significant effects on the rate versus $\Delta_r G + \lambda$ plots, for the same reasons discussed in the context of the rate dependence on QD sizes. In the positive $\Delta_r G + \lambda$ regime, $\Delta_r G + \lambda$ increases as R_{CdSe} decreases (Figure 9b). Increasing $\Delta_r G + \lambda$ reduces the rate, while decreasing R_{CdSe} accelerates the rate by increasing the electronic coupling. These two counteracting effects make the ET rates weakly sensitive to $\Delta_r G + \lambda$, except when R_{CdSe} is small (in this case the electronic couplings are more sensitive to R_{CdSe} than in the large radius case). Including other factors, such as the inner sphere reorganization energy, will not substantially change the general conclusions regarding the rate dependence on $\Delta_r G + \lambda$ and they may soften the rate maximum.

Transition between through-bond and through-space coupling mechanisms as QD radii change. Through-bond ET rates are generally one order of magnitude larger than the corresponding through-space rates if the donor and acceptor QDs radii are smaller than 12 Å (see Figure 8). However, as one or both of the QDs increase in size, the through-space charge transfer rates tend to be larger than the through-bond rates at fixed CdSe to CdTe edge-to-edge distances. Therefore, the ET between CdTe and CdSe QDs at a given distance are predicted to have specific radii in which the ET mechanism switches from dominantly through-space to dominantly through-bond.

Figure 10a shows a contour plot of the through-bond and through-space ET rate differences as a function of donor and acceptor radii. As discussed in Sec. 2.3.2, the through-bond couplings are larger than the through-space couplings if the two QD radii are less than 15 Å (at fixed distances) and *vice versa*. This difference between through-space and through-bond couplings causes the through-bond ET rates to be two orders of

magnitude larger than the through-space ET rates in the small-size regime (both QD radii ~ 10 Å), and one order of magnitude lower in the large-size regime (both QD radii ~ 25 Å). In other size regimes, through-space ET rates can be larger or smaller than through-bond ET rates depending on the radii. This switching between through-bond and through-space mechanisms as a function of QD size causes the through-bond mechanism to dominate for small QDs and the through-space (including through-solvent) mechanism to dominate for larger QDs.

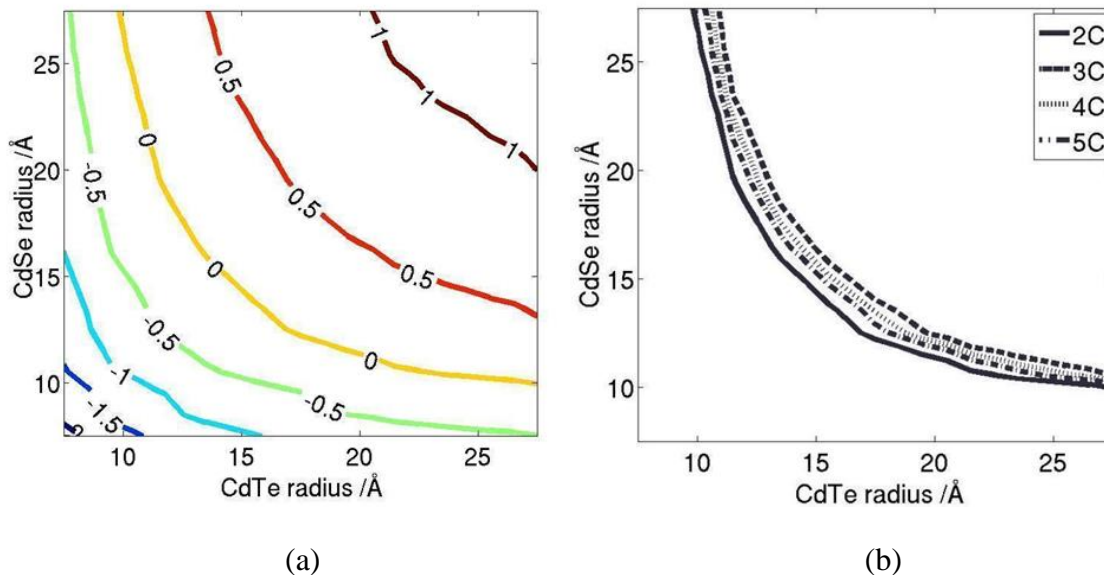


Figure 10: Through-solvent and through-bridge electron transfer mechanism dominance switch. (a) The plot shows contour lines at fixed values of $\log_{10}(k_{TS}/k_{TB})$ for ET as a function of CdTe and CdSe radii. (b) Equal rate lines for through-bond and through-space ET rates are shown for CdSe and CdTe QDs bridged by SH(CH₂)₂SH (2C), SH(CH₂)₃SH (3C), SH(CH₂)₄SH (4C) and SH(CH₂)₅SH (5C). The values of $\log_{10}[k_s(R_{CdTe}, R_{CdSe})/k_b(R_{CdTe}, R_{CdSe})]$ are indicated on the contour lines.

The through-space and through-bond couplings between QDs decrease with edge-to-edge distance in the bridged structures (Figure 7). Our calculations find that the equal-rate separation line for different edge-to-edge distances (dithiol bridge lengths) are

approximately $L = R_{CdTe} \times R_{CdSe}$, where $L = 126 \text{ \AA}^2$ (Figure 10a). The equal rate lines for different bridge lengths nearly overlap. Therefore, the edge-to-edge distance between QDs does not significantly change the dominance of the coupling mechanisms. This insensitivity to distance arises from the fact that the through-space and through-bond coupling distance decay constants are nearly equal for all of the QD sizes studied. Our DFT results show that both through-space and through-bond LUMO-LUMO couplings decay exponentially with decay constants of 0.30 \AA^{-1} . For electron mediated QD-to-QD tunneling, the position of the bridge LUMO energy defines the effective tunneling barrier. The dithiol molecules have LUMO energies near the ionization limit, so the vacuum tunneling barrier and the bridge-mediated electron tunneling barriers are similar; however other bridging molecules with different energetics could change this feature. We find that the dividing line separating through-bond and through-space ET coupling mechanisms is nearly independent of the edge-to-edge distance. Analogous behavior is found for hole transfer (see Figure 7c,d in section Sec 2.3.2). In general, the contour plot for the through-space and through-bond hole transfer rates as a function of CdSe and CdTe radii has similar characteristics to those found for the ET rates shown in Figure 10a. The line where the through-space rate equals the through-bond rate is also independent of the dithiol length. The crossover line for through-bond/through-space hole transfer is described by $R_{CdTe} \times R_{CdSe} = 225 \text{ \AA}^2$.

Differences between electron transfer and hole transfer rates depends only on the QD radius ratio. Efficient solar cells require similar electron and hole transfer rates to

keep charge carriers from becoming trapped. After an electron in a photoexcited QD transfers to another QD, a hole is left. If the hole transfer is slow, the regeneration of the photoinduced electron current will be inhibited. Figure 11 shows the difference between the total electron and the hole transfer rates as a function of QD radii. The total ET rates are larger than the total hole transfer rates for the approximate radius ratio $R_{CdTe}/R_{CdSe} < 1.3$, and ET rates are smaller than hole transfer rates if $R_{CdTe}/R_{CdSe} > 1.3$. As discussed above, smaller donor and larger acceptor radii generally lead to larger charge transfer rates, mainly because of the acceptor DOS. Larger ET rates correspond to smaller R_{CdTe}/R_{CdSe} values, and larger hole transfer rates correspond to smaller R_{CdSe}/R_{CdTe} values. The CdTe to CdSe radius ratio of 1.3 (for comparable hole transfer and ET rates) is different from the radius ratio of ~ 2.0 where the ET activation free energy reaches its minimum and the value of 1.3 is also far from ~ 0.6 (~ 1.8 for R_{CdSe}/R_{CdTe}) where the hole transfer activation free energy reaches its minimum value. This difference between these two radius ratios arises from the differences in the band edge energies of CdTe and CdSe. It is possible that other QD pairs will have comparable ET and hole transfer rates, as well as large charge transfer rate values.

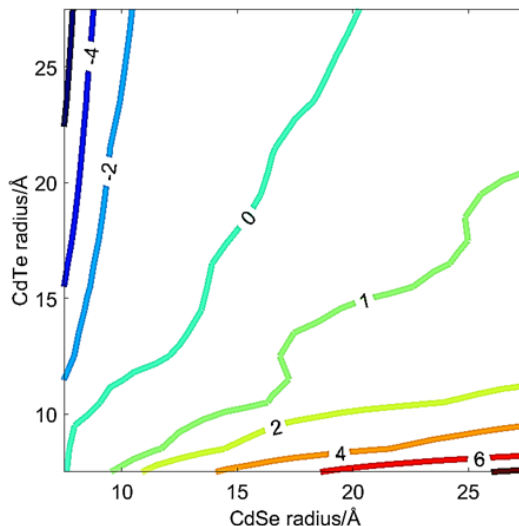


Figure 11: Ratio of electron to hole transfer rates as a function of QD radii. The plot shows contour lines at fixed values of $\log(k_{ET}/k_{HT})$ as a function of CdTe and CdSe radii.

2.3.4 Size-dependent hole transfer rates

Through-solvent hole transfer rates. The computed hole transfer (HT) rates from photo-excited CdSe of a fixed size to ground state CdTe are shown in Figure 12a as a function of R_{CdTe} . As the acceptor R_{CdTe} increases, a maximum HT rate is found at a radius of ~ 12 Å. A maximum in rate is found because of the larger HT pairwise atom-to-atom distance decay constant γ_i value (see Table 2) for the HOMO-HOMO interaction than for the LUMO-LUMO interaction. This causes the coupling to decay more quickly as a function of QD radius for the HOMO-HOMO (HT) coupling than for LUMO-LUMO (ET) coupling. In bulk CdTe, the estimated effective masses are $0.112 m_e$ for light holes and $0.892 m_e$ for heavy holes.¹²⁷ The estimated electron effective mass in bulk CdSe is $0.116 m_e$. Therefore, the DOS of the CdTe valence band is expected to increase more slowly as the energy decreases, compared to the case of electron transfer. The slower DOS increase

in the CdTe valence band and the more rapid coupling decrease coupling with R_{CdTe} than in the ET case lead to maxima in the HT rates as a function of R_{CdTe} for nearly activationless HT reactions. The computed HT rates decrease with donor radius (R_{CdSe}), and the causes are similar to those that produce a decrease in the ET rates with its donor radius (R_{CdTe}). Note that these rate maxima may be modified by features not yet taken into account, such as inner sphere reorganization energy, QD structure, or QD surface states.

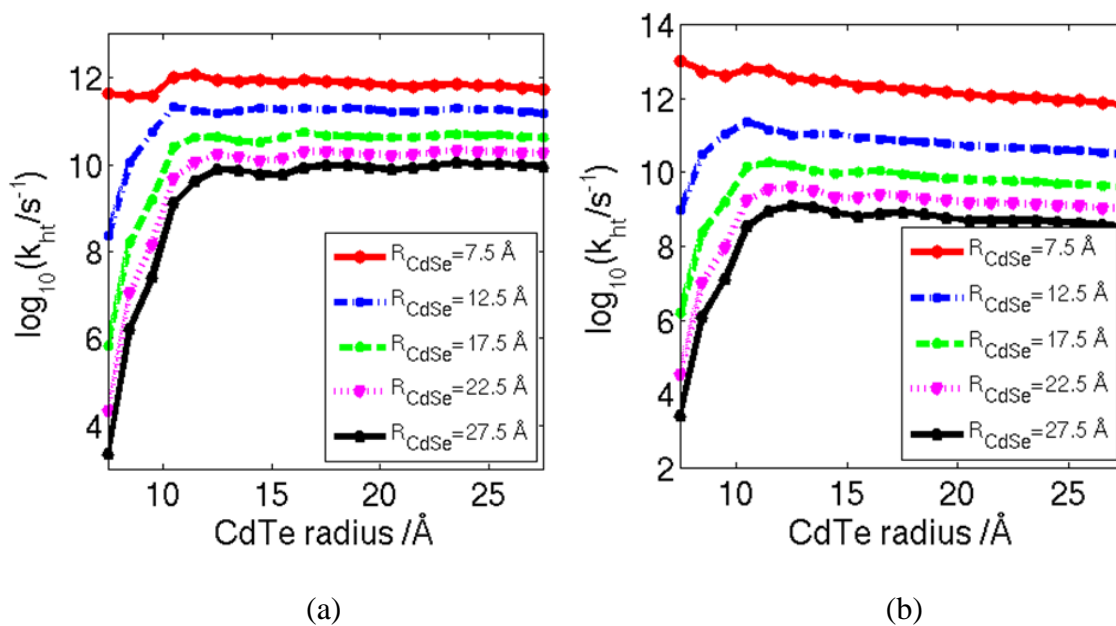


Figure 12: Size-dependent hole transfer rates. Computed through-solvent (a) through-bond (b) HT rates between CdTe and CdSe QDs as a function of acceptor QD radius. The HT rates depend on the donor QD radius. The dielectric constant is 15.

We found that the maximum HT rate is expected to occur near a single CdSe radius for all CdTe QD radii. The charge transfer rate as a function of $\Delta_r G$ (which depends on QD radii) is expected to reach a maximum when $-\Delta_r G = \lambda$.^{108,132,133} The value of R_{CdTe} for activationless HT, R_{CdTe}^* , increases with R_{CdSe} . For example, if R_{CdSe} increases from 7.5 Å to 21.5 Å, R_{CdTe}^* increases from 8.5 Å to 12.5 Å. The computed R_{CdTe}^* that maximizes the

HT rate does not change significantly with R_{CdTe} ; its value remains near 11 Å. The rapid decrease in the HOMO-HOMO coupling with R_{CdTe} compared to the slow increase in the DOS causes the rate maxima to be weakly R_{CdTe} dependent as R_{CdSe} varies. The predicted oscillations in the HT rates as a function of R_{CdTe} are relatively large compared to the oscillations predicted for the ET rates, because of the fluctuations in the HOMO-HOMO through-solvent coupling (Figure 7b) and in the CdTe valence band DOS are larger than for ET.

For a 7.5 Å radius QD acceptor, the HT rates are $\sim 10^{12} \text{ s}^{-1}$ as the donor QD size varies from 27.5 to 7.5 Å. For a 7.5 Å radius QD acceptor, the ET rates range from 10^{10} to 10^{12} s^{-1} as the donor QD size decreases from 27.5 to 7.5 Å. These trends in the rates are understood because the reaction free energy windows for HT and ET from a QD donor to a small QD acceptor are different. For ET from a 7.5 - 27.5 Å radius donor (CdTe) QD to a small 7.5 Å radius acceptor (CdSe) QD, $\Delta_r G^\ddagger$ changes from 0 to 0.25 eV, whereas HT from a 7.5 - 27.5 Å radius donor (CdSe) QD to a small 7.5 Å radius acceptor (CdTe) acceptor, $\Delta_r G^\ddagger$ changes from 0 to 0.45 eV.

Through-bond HT rates. The computed through-bond HT rates as a function of R_{CdTe} at selected R_{CdSe} values are shown in Figure 12b. The HT rates decrease with a decrease in both CdTe and CdSe QD sizes. Maxima in the R_{CdTe} dependent HT rates occur approximately following the linear relation $R_{CdTe}^* = 0.23 \times R_{CdSe} + 7.5$. The stronger through-bond HOMO-HOMO coupling decay with R_{CdTe} , combined with the slow growth in the computed CdTe DOS with R_{CdTe} , causes the reduced HT rates as R_{CdTe} grows. The faster through-bond HOMO-HOMO coupling decay, compared to the through-solvent

HOMO-HOMO coupling decay as a function of R_{CdTe} , results in the R_{CdTe} dependent maxima in the HT rates to disappear when R_{CdSe} increases. The HT rates decrease with increasing R_{CdSe} for the same reason as in the case of through-solvent hole transfer. In summary, as the size of the CdTe QD increases, the rapid decay of the through-bond HOMO-HOMO coupling compensates the possible HT rate enhancements produced by the increase in the CdTe DOS and the decrease in the activation free energy. As a result, the through-bond hole transfer rates are always predicted to decrease with an increase in R_{CdTe} .

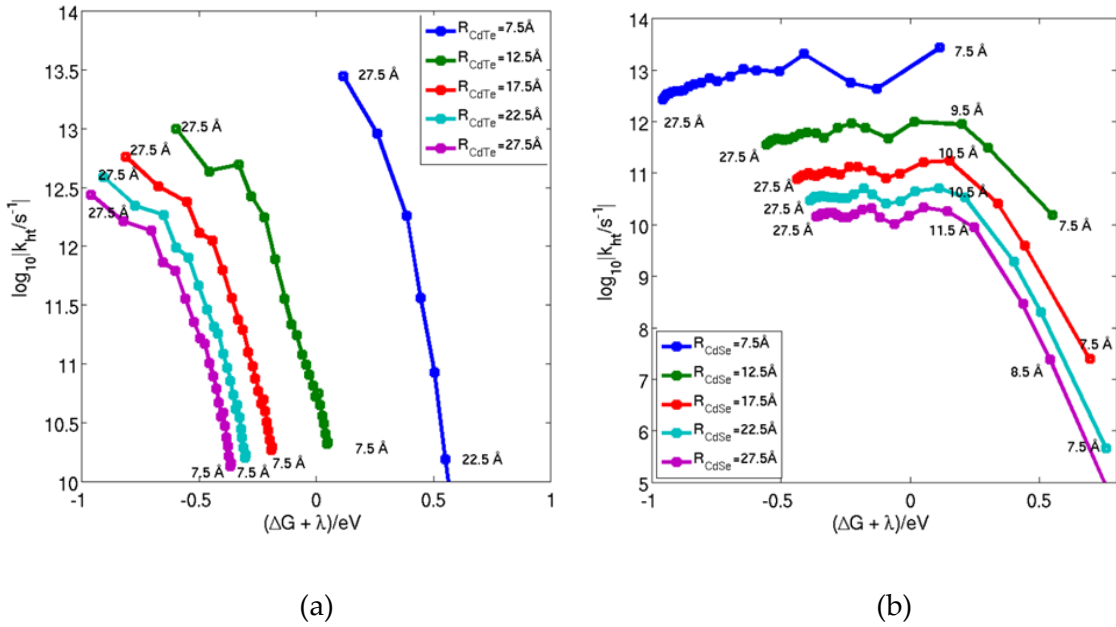


Figure 13: CdTe-CdSe hole transfer rates as a function of $\Delta_r G + \lambda$ with fixed acceptor (c) and donor (d) radii. The numbers on the lines indicate the radii of the QD, which determines the value of $\Delta_r G + \lambda$.

HT Rates as a function of $\Delta_r G + \lambda$. In the two-state Marcus theory, the charge transfer mechanism changes from the normal to the inverted regime when $\Delta_r G + \lambda$ changes sign. The total HT rates (eq 2.1) as a function of $\Delta_r G + \lambda$ are shown in Figure 13a and 13b

respectively. In these QD-QD HT systems, a transition from the normal to the inverted region appears only in some instances. For example, if R_{CdTe} is fixed at 12.5 Å, the rate goes through a maximum for positive $\Delta_r G + \lambda$. The reasons have been discussed in the main text.

Transition between through-bond and through-solvent coupling mechanisms as QD radii change. Through-bond HT rates are generally one order of magnitude larger than the corresponding through-solvent rates if the donor and acceptor QDs' radii are smaller than 12 Å (see Figure 12). However, as one or both of the QDs increase in size, the through-solvent charge transfer rates tend to be larger than the through-bond rates at fixed CdSe to CdTe edge-to-edge distances. Therefore, the charge transfer between CdTe and CdSe QDs at a given distance are predicted to have specific radii in which the charge transfer mechanism switches from dominantly through-solvent to dominantly through-bond.

A contour plot of the difference between the through-bond and through-solvent HT rate is shown in Figure 14a. The through-bond to through-solvent HT transition occurs at smaller $R_{CdTe} \times R_{CdSe}$ values than for ET and arises because of the different through-bond and through-solvent coupling dependence on the QD size. The LUMO-LUMO and HOMO-HOMO through-bond couplings are close to each other for all QD sizes, and they are larger in magnitude than those of through-solvent couplings for small QD sizes. However, through-solvent couplings decay more slowly than through-bond couplings as a function of the donor and acceptor QD radii. Therefore, a crossover from through-bond to through-solvent at larger QD radii occurs. In addition, the magnitude of the LUMO-LUMO

through-solvent coupling is smaller than the HOMO-HOMO through-solvent coupling for small QD sizes. Therefore, through-solvent HT coupling crosses with through-bond HT coupling at a smaller QD size than for ET. The similarity between the two through-bond couplings may arise from the nature of the bridge dithiol molecule, and the differences between the two through-solvent couplings are expected from the differences between the atom-to-atom interaction pre-factors and distance constants (Table 2) for LUMO-LUMO and HOMO-HOMO couplings in the tight-binding model.

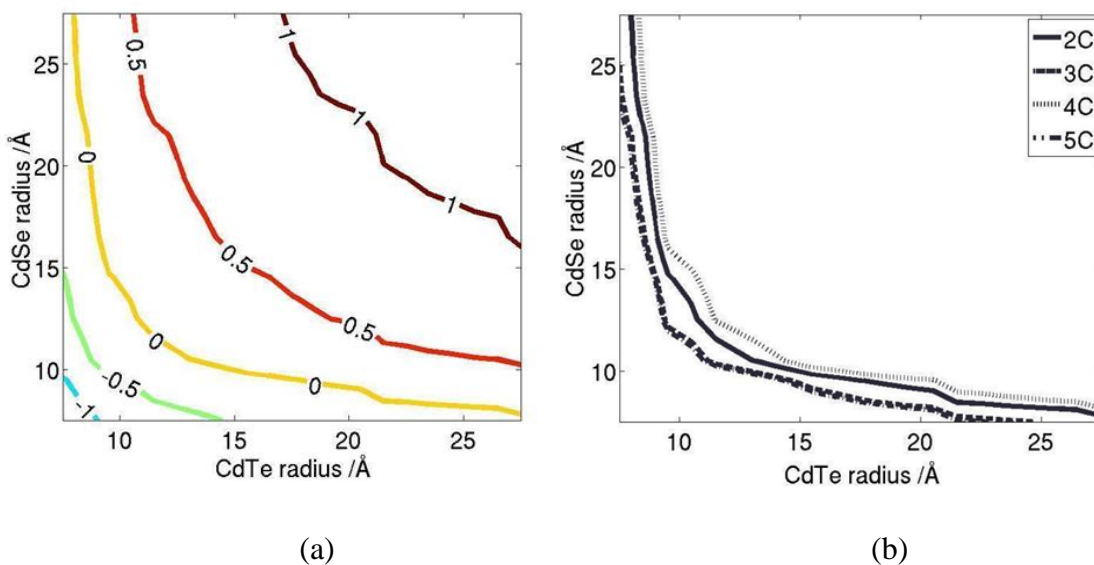


Figure 14: Through-solvent and through-bridge hole transfer mechanism dominance switch (a) Contour lines indicate $\log_{10}(k_{TS}) - \log_{10}(k_{TB})$ for HT as a function of CdTe and CdSe radii. (b) Equal rate lines for through-bond and through-solvent HT rates for CdSe and CdTe QDs bridged by SH(CH₂)₂SH (2C), SH(CH₂)₃SH (3C), SH(CH₂)₄SH (4C) and SH(CH₂)₅SH (5C). The values of $\log_{10}[k_s(R_{CdTe}, R_{CdSe})/k_b(R_{CdTe}, R_{CdSe})]$ are indicated on the contour lines.

The transition from through-bond to through-solvent dominated HT mechanism weakly depends on edge-to-edge distance. The through-solvent and through-bond couplings between QDs decrease with edge-to-edge distance in the bridged structures

(Figure 7). Our calculations find that the equal-rate separation line for different edge-to-edge distances (dithiol bridge lengths) are approximately $L = R_{CdTe} \times R_{CdSe}$, where $L = 225 \text{ \AA}^2$ for HT (Figure 14b). The equal rate lines for different bridge lengths nearly overlap. Therefore, the edge-to-edge distance between QDs does not significantly change the dominance of the coupling mechanisms. This insensitivity to distance arises from the fact that the through-solvent and through-bond coupling distance decay constants are nearly equal for all of the QD sizes studied. The same reasons have been discussed for ET case.

2.3.5 Dielectric constant effects on charge transfer rates

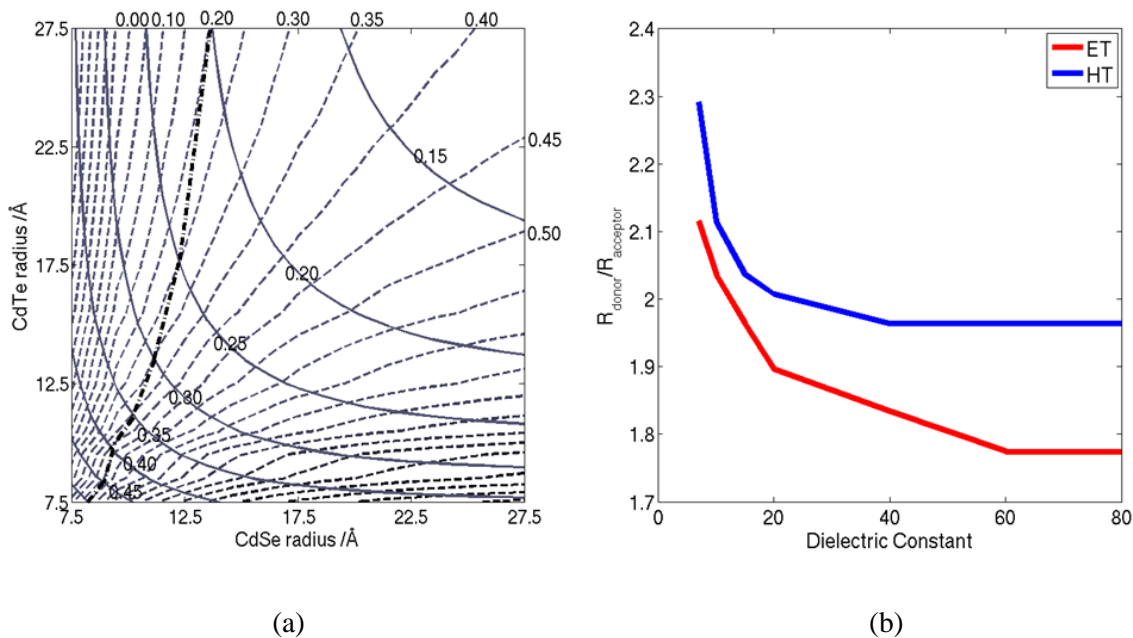


Figure 15: Solvent dielectric constant effects. (a) Contour plot of reaction free energy, $\Delta_r G$, and reorganization energy, λ , with respect to QD radii; the dashed lines refer to $\Delta_r G$ (in eV, labeled at the top of the plot), the solid lines refer to λ (in eV, labeled inside the plot) and the dot-dash line indicates the QD radius combination where $-\Delta_r G = \lambda$. (b) The donor acceptor radius ratio that produces the smallest charge transfer activation free energy value is plotted as a function of dielectric constant.

The QD radius ratio ($R_{donor}/R_{acceptor}$) that produces the charge transfer activation free energy valley in Figure 5a,b depends on the dielectric constant (ϵ_s), since $\Delta_r G$ and λ depend on ϵ_s . The $R_{donor}/R_{acceptor}$ value that produces the smallest charge transfer activation free energy values is plotted in Figure 15a. The $R_{donor}/R_{acceptor}$ value (R_{CdTe}/R_{CdSe} for ET, and R_{CdSe}/R_{CdTe} for hole transfer) that produces the smallest activation free energies decreases as ϵ_s increases, and the dependence is especially pronounced when $\epsilon_s < 20$. When $\epsilon_s > 20$, the $R_{donor}/R_{acceptor}$ value that produces the smallest activation free energy decreases slowly to 1.8 for ET (2.0 for hole transfer) as ϵ_s approaches the dielectric constant of water. For ET (hole transfer) can be analyzed similarly), the Coulomb energy of the charge separated state is much smaller than the reorganization energy ($|E_c| \ll \lambda$), so the activation free energy is dominated by λ and the band edge energy difference ($E_{CdSe,LUMO} - E_{CdTe,LUMO}$), eq 2.19. The λ increases with ϵ_s , while $|E_{CdSe,LUMO} - E_{CdTe,LUMO}|$ is independent of ϵ_s , but increases as R_{CdTe}/R_{CdSe} decreases (See Figure 1 for details). Therefore, the R_{CdTe}/R_{CdSe} values for activationless ET ($-|\Delta_r G| + \lambda = 0$) decrease as ϵ_s grows.

2.4 Summary and conclusions

We constructed a tight-binding Hamiltonian model to describe the electronic properties of large QD systems and used it to explore the size dependent electron and hole transfer rates between donor and acceptor QDs.

Through-bond and through-space couplings depend on the QD radii. The through-bond coupling between QDs linked by an extended geometry dithiol molecule decreases with increasing QD radii because the wavefunction amplitudes of the QD atoms attached to the dithiol decrease as the QD radii increases. The through-space coupling

between two QDs at fixed distance also decreases with increasing QD radii because of the same surface wavefunction dilution effect. Overall, the decrease in the through-space coupling is weaker than the decrease in the through-bond coupling with increasing QD radius because the increasing surface area of the QD partially compensates for the wavefunction dilution effect.

A growing acceptor DOS competes with the shrinking coupling and Franck-Condon factor for rate control. As the acceptor QD radius increases, the decreasing through-bond and through-space electronic couplings and the increasing DOS have opposite effects on the rate. As the acceptor QD size increases, the through-bond (electron transfer and hole transfer) and the through-space hole transfer rates display a maximum as a function of acceptor radius. The acceptor radii of these three rate maxima are determined by the radius-dependent ΔG^\ddagger . However, as the acceptor radius increases, the through-space electron transfer rate depends weakly on the acceptor radius, and there is no maximum in the rate *versus* radius plot. This behavior occurs because the growth in the acceptor DOS (which accelerates the rate) overwhelms the rate slowing induced by the decrease in the through space electronic coupling and the reaction free energy inverted effect. This interplay of size effects can produce a rate behavior in QDs that is distinct from the inverted free energy regime found for electron transfer and hole transfer in molecules.

The electron transfer or hole transfer rates show a similar size-dependence because of the comparable competition among coupling, DOS, and Franck-Condon factors. In general, the rates show maxima as the acceptor QD radii increase for donor radii ranging from $\sim 9.5 \text{ \AA}$ to $\sim 21.5 \text{ \AA}$. For smaller donors (radii $< \sim 9.5 \text{ \AA}$), the rates drop as the acceptor

radius increases and for larger donors (radius $> \sim 21.5 \text{ \AA}$), the electron transfer rates increase with the acceptor radius. In molecules, the charge transfer rate displays a maximum when the reaction changes between the normal and the Marcus inverted regimes; however, in the QD systems a charge transfer rate maximum can only occur in certain size regimes and is determined by the QD's electronic properties.

Donor radius effects on charge transfer rates. The through-space, through-bond, and total charge transfer rates decrease with donor radius for three reasons; (1) the tunneling energy increases as the donor radius increases, (2) the tunneling electron accesses a lower acceptor DOS, and (3) the donor-acceptor coupling decreases. Therefore, larger charge transfer rates are expected for smaller donor QD radii.

Charge recombination. The charge recombination rate also depends on the sizes of CdTe and CdSe QDs, but they are most strongly influenced by the surface defect states.^{134–136} The electronic properties of the surface defect states are system dependent and their description would require high-level electronic structure analysis, which is beyond the scope of the current study. The charge recombination rates arising from the QDs in the absence of defect states (our model) are expected to be much slower than the defect state induced charge recombination rates of 10^8 s^{-1} observed experimentally.^{46,57}

The dominance of through-space vs. through-bond charge transfer mechanisms is determined by QD size. Through-bond coupling dominates for small QD pairs and through-space coupling dominates for larger QD pairs. The fraction of the QD surface area that participates in the through-space coupling increases with the QD radius. As such, increasing the QD radius weakens the through-bond coupling more than it

weakens the through-space coupling. When through-space and through-bond couplings are comparable in strength, the total charge transfer rate needs to include interference among the coupling pathways. For small QDs, we find that the interference effect on the total charge transfer rate is significant. The interference changes the size dependence of the charge transfer rate compared to the individual through-space and through-bond rate dependences on size. For large QDs, the interference effect is less significant. The contributions of the through-bond and through-space charge transfer mechanisms can be manipulated by changing the QD radii as shown in Figures 10a,14a. When $R_{CdTe} \times R_{CdSe} = 225 \text{ \AA}^2$ for electron transfer (126 \AA^2 for hole transfer), through-space and through-bond mechanisms contribute approximately equally. When $R_{CdTe} \times R_{CdSe}$ is much larger than the above values, through-space coupling dominates. Through-bond coupling dominates when $R_{CdTe} \times R_{CdSe}$ is much less than 225 \AA^2 for electron transfer (126 \AA^2 for hole transfer). These values are found to be independent of dithiol length in the edge-to-edge distance range of 9 - 13 \AA . This originates from the similar rate of decrease for the through-space and through-bond couplings with edge-to-edge distance in the QDs. The larger prefactor for through-space coupling compared to through-bond coupling causes through-space charge transfer rates to be larger than through-bond charge transfer rates when $R_{CdTe} \times R_{CdSe}$ is larger than 225 \AA^2 for electron transfer (126 \AA^2 for hole transfer). When the through-space charge transfer mechanism dominates for large QDs, the details of the bridge chemistry are not important, unless they perturb the electronic structure of the QDs.

Consequences of electron transfer and hole transfer rate differences for charge separation schemes in QD assemblies. The electron transfer and hole transfer rates for

fixed edge-to-edge QD distances are not generally equal. In QD solar cells with both CdSe and CdTe photo absorbers, the ratio of electron transfer and hole transfer rates influences the charge-separation efficiency.^{137–139} We calculated this rate ratio using the tight-binding analysis, and provided a design principle for tuning the rate ratio by modifying the QD sizes. For example, the electron transfer and hole transfer rates can be tuned to be very similar and thus optimize solar cell performance (e.g., when $R_{CdTe}/R_{CdSe} \approx 1.3$), or the electron transfer and hole transfer rates can be tuned to be very different (e.g., when $R_{CdTe}/R_{CdSe} \ll 1.3$ the electron transfer rate is much larger than the hole transfer rate).

3. Charge-influenced Through-solvent and Through-bridge Electron Transfer Between Linked Quantum Dots

In this chapter, we theoretically study the charge influences on the through-solvent and through-bridge donor-acceptor couplings between linked quantum dots. This work is based on a collaborative project with Peng Zhang.

3.1 Introduction

Electron transfer is an essential process in nanoparticle (NP) and quantum dot (QD) implications like QD solar cell,^{38,39,68,140,141} QD light-emitting diode (QLED),^{142–144} nanoparticle-based battery,¹⁴⁵ photocatalysis,^{146,147} QD-based biotechnology,^{3,148–150} QD integrated circuits,^{151,152} and photodetectors.^{153,154} Controlling the charge transfer rates in the QDs is critical to the development of these QD related technologies. For example, the relative high charge recombination rates in the QD solar cell as compared to the charge separation rates limit the QD solar cell performance.^{45,46,48,50,57} In previous studies, it is found that through-solvent (TS) donor (D)-acceptor (A) couplings can be comparable to through-bridge (TB) couplings in QD-QD charge transfer systems, although TS contribution to charge transfer coupling in most donor-bridge-acceptor (D-B-A) systems is much weaker than TB couplings.^{155,156,157} Our calculations of size-dependent electron transfer (ET) in QD dyads suggest that TS coupling is larger than TB coupling if the product of the two QD radii is large ($>225 \text{ \AA}^2$ for the CdTe-CdSe dyad).¹⁵⁸ Larger through-solvent coupling is found to arise from direct interactions between QD surface atoms in the QD-QD contact, and the number of these atoms grows with QD radius. These findings suggest that the TS coupling can be comparable to the TB coupling, depending on the

conditions like D-A distance and system sizes. In such systems, the TS and TB coupling contributions should both be considered.

Strong QD-QD coupling is required in QD solids to evolve from carrier hopping to high-mobility band-like charge transport in delocalized and extended QD solid states.^{10,159} Weak QD-QD coupling should be maintained in the QLED devices so that the electron and hole wave functions are localized within the QDs, and thus the devices provide high electroluminescence efficiency.^{10,144,160,161} The QD-QD couplings need to be controlled in QD solar cells so that the couplings for the charge separation processes are strong while the couplings for the charge recombination processes are weak.^{45,46,48,50,57} In addition, controlling the dominant the D-A coupling mechanism (the through-solvent (TS) or through-bridge (TB) channels) might be important for some QD implications. For example, chiral induced spin selectivity (CISS) was found in charge transfer through chiral molecules like DNA chain.¹⁶²⁻¹⁶⁶ QD dyad linked by chiral molecular bridge may also have CISS effects. To improve the spin selectivity yield, charge transfer between two QDs should occur exclusively through the spin selected through-chiral bridge channel, and vice versa. These requirements in controlling the QD-QD coupling strength and the dominate coupling mechanism (TS and TB mechanisms) motivate us to study the possible manipulation of the QD-QD electronic couplings.

It is known that external electric field can perturb the energetic and wave functions of the molecular system, therefore changing the electron tunneling barrier and tunneling pathways. We propose that the charge group in the molecular bridge that links the two QDs

can influence the D-A coupling strength and tune the dominance between through-bridge and through-solvent D-A coupling mechanism.

The influence of the external charge on the TS and TB charge transfer couplings are not well understood and the results are controversial. A theoretical study shows that the amino acid mediated ET coupling between two ethylene can be influenced by the charge on the amino acid, however, the charge induced effect on the D-A coupling is small.¹⁶⁷ Similarly, a semi empirical quantum-chemical calculation in conjugated oligomers shows that the external field produce negligible effects on the charge transport in organic semiconductor even with a relatively strong field (10^8 V/m).¹⁶⁸

In this study, we introduce a charge into the bridge region between two QDs by replacing a neutral group in the molecular bridge with a charged group. We use $-\text{NH}_3^+$ to replace $-\text{NH}_2$ R group and $-\text{COO}^-$ to replace $-\text{COOH}$ R group in the extended alkyl dithiols $\text{HS}(\text{CH}_2)_n\text{CH}(\text{R})(\text{CH}_2)_n\text{HS}$ ($n = 1, 2, 3, 4$). We first describe a tight-binding model that includes through-solvent and through-bridge couplings between the QDs in a linked QD dyad. We then systematically examine the changes in the QD, solvent and bridge molecular frontier orbital energies in the presence of a charged species. With the charge influenced energy parameters, we use the tight-binding model to calculate the TS and TB coupling strengths for QD dyads linked by neutral and charged dithiols. We lastly investigate the charge influenced TS and TB coupling dependences on the QD size and on the QD surface-to-surface distance.

3.2 Theoretical models and computational details

Tight-binding models for TS and TB couplings. CdTe-CdSe QD dyad is often used as a charge separation and energy harvesting unit in QD solar cells, and the two QDs in the dyad are usually linked by an extended molecular like dithiol.^{37,38,88,169,170} The type-II CdTe-CdSe dyad with band edge energy alignment for donor and acceptor allows electron transfer through the conduction bands and hole transfer through the valence bands. We proposed a tight-binding model to describe the through-solvent and through-bridge couplings between the two QD as illustrated in Figure 16. In the QD-linker-QD system, the donor (CdTe), bridge (B) and acceptor (CdSe) units are surrounded by water solvent (S), and their electronic properties are treated by a tight-binding Hamiltonian.

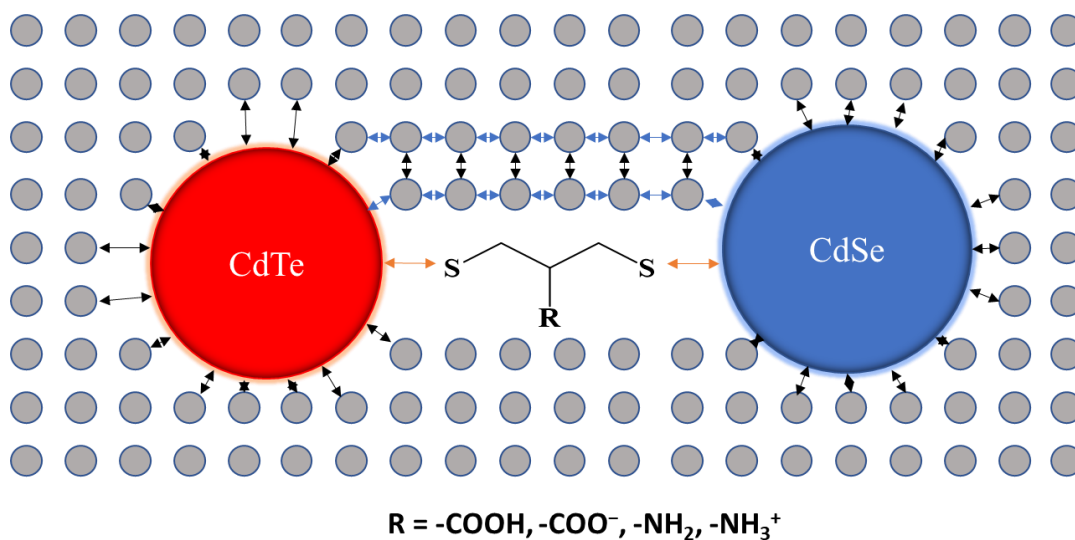


Figure 16: Through-solvent and through-bridge coupling tight-binding model scheme. 3D lattice model of two QDs (large red and blue circles) coupled through solvent molecules (gray circles) and a bridge molecule $\text{HS}(\text{CH}_2)_n\text{CH}(\text{R})(\text{CH}_2)_n\text{HS}$ ($n = 1, 2, 3, 4$; $\text{R} = -\text{COOH}, -\text{COO}^-, -\text{NH}_2, -\text{NH}_3^+$). Only $n = 1$ case is shown. The sulfur atoms of the dithiol link the QDs. The solvent molecules near the QD surfaces couple (black

arrows) to the QDs, and each solvent molecule couples (blue arrows) to its nearest neighbors.

The Hamiltonian of the whole system is,

$$H = H_D + H_B + H_S + H_A + H_{DB} + H_{DS} + H_{AB} + H_{AS} \quad (3.1)$$

Here H_k ($k = D, B, S, A$) is the Hamiltonian for the donor QD, bridge molecule, solvent molecules, and the acceptor QD. H_{lm} ($l=D, A; m=S, B$) describes their mutual interactions. We assume that there is no direct interaction between the QDs because of their large separation (the smallest QD-QD distance studied is ~ 1 nm, and the QD-QD through-vacuum coupling at this distance is on the order of 10^{-8} eV, which are much smaller than the solvent and bridge mediated couplings between the QDs). Also, we neglect direct charge transfer between solvent and the bridge because of the much weaker water-bridge coupling as compared to the water-water interaction. When a water molecule placed perpendicular to the HSCH₂CH(COOH)CH₂HS backbone and ~ 5 Å away, the coupling between their lowest unoccupied molecular orbitals (LUMO) is $\sim 10^{-2}$ eV, which is much smaller than the water-water coupling 0.45 eV used in this study.

QD tight-binding model H_D and H_A . For QDs, we use a tight-binding model developed previously. The details of this tight-binding treatment of the CdTe and CdSe QDs are discussed elsewhere.^{33,158} In this model, each atom in the QD is treated as a charge hopping site and has two effective orbitals (for conductance and valence band respectively). The QD atomic positions are determined by the geometry of a QD cut out of bulk zinc blende structure. Each atom in the QD couples to four (unless for surface sites, which have less than four) nearest atoms, and the site (orbital) energy and atom-atom

coupling values are fitted to reproduce the experimentally^{33,158} derived QD band-edge energies as a function of the QD radius. The parameters in H_D and H_A is listed in Ref. 5.

Tight-binding model for solvent molecules H_S . Each solvent molecule is treated as a charge hopping site. The site energy and their interactions are parameterized using molecular dynamics simulations combined with *ab initio* computations. The details of the parameterization are presented in Sec. III. Specifically, the solvent Hamiltonian H_S is

$$H_S = \sum_i^N \varepsilon_i |i\rangle\langle i| + \sum_i^N \sum_j v_s (|i\rangle\langle j| + |j\rangle\langle i|) \quad (3.2)$$

where N is the number of solvent molecules in the system and v_s is the solvent-solvent coupling. Index i (j) denotes the i^{th} (j^{th}) solvent molecule in the 3D lattice model. In this model, we place each water into the 3D cubic lattice. The distance between two lattice point is 3.1 Å, representing an average water-water shortest distance.¹⁷¹ We only consider the nearest-neighbor interaction, $v_s = 0.45$ eV (see Sec. III). The site energy ε_i is the same for N solvent sites if the QD-linker-QD system is neutral. When a charged group is introduced into the bridge, ε_i changes according to the distance between the water and charge centers. We assume that the solvent-solvent coupling is less sensitive to the introduced bridge charge. For two water molecules placed 3.1 Å (O-O distance) away, their LUMO-LUMO coupling variation by an external charge is ~ 0.01 eV, or $\sim 0.5\%$ of their LUMO energy shifts. Note, the point charge is placed 5 Å away to both water molecules.

The QD-solvent interaction H_{lS} ($l = D$ and A).

$$H_{lS} = \sum_i \sum_j v_{ij} (|i\rangle\langle j| + |j\rangle\langle i|) \quad (3.3)$$

where index i represents a QD surface atom and index j denotes a solvent molecule. We assume the QD can only interact with the water molecules when the distance between the

water O atom to the nearest QD surface atom is not larger than 5 Å. We further assume a constant interaction between water and the QD surface atom. In our calculation we choose $v_{ij} = 0.45$ eV, which is the same as the water-water interaction. This is an adjustable parameter in our calculations, and the choice of this value assumes that the non-covalent water-water and water-QD interactions are on the similar order of magnitude. Variation of this parameter will not change the qualitative nature of our conclusions on the charge induced through-solvent coupling change.

Molecular bridge model. The CdTe and CdSe QDs are linked by dithiols $\text{HS}(\text{CH}_2)_n\text{CH}(\text{R})(\text{CH}_2)_n\text{HS}$ ($n = 1, 2, 3, 4$; $\text{R} = -\text{COOH}, -\text{COO}^-, -\text{NH}_2, -\text{NH}_3^+$) with the QD-QD distance determined by the number of alkyl units $2n$. The charged R groups are used to introduce charges into the bridge region between the QDs. Note, dithiol molecules can attach either covalently or noncovalently to the QD.^{37,120,121} For calculational convenience, we non-covalently link the QDs with the bridging molecules, and the D-B and B-A couplings are relatively weak. The general conclusions related to the charge influenced through-bridge coupling do not likely depend on this linkage chemistry. When $n = 1$, the surface-to-surface distance between the QDs is 10 Å. The bridge Hamiltonian H_B is constructed using the Kohn-Sham matrix computed using B3LYP/6-31G*. We further assume that only the S valence atomic orbitals (3s, 3p) couple to the nearest QD atom. The coupling strength is also chosen to be 0.45 eV. This choice was made because both the water and the bridge interact with the QDs non-covalently and the O atom in water and the S atoms in dithiol have similar electronic properties. Our qualitative conclusions will not be sensitive to the choice of this value.

Block-diagonalization method computed TS and TB couplings. Since there is no direct interaction between the bridge and solvent, we can dissect the D-A coupling into the TS and TB contributions respectively. For the TS coupling, the D-S-A system can be defined from the system Hamiltonian in eq 3.1, i.e., $H_I = H_D + H_A + H_S + H_{DS} + H_{SA}$. In the current system, electron transfer between the QDs occurs through the tunneling mechanisms, because the energy disparity between the QD band edge energies and the water (bridge) HOMO/LUMO energy is large (deep tunneling). In this scenario, the D-S-A system Hamiltonian matrix is divided into matrix blocks corresponding to D, S and A,

$$H_1 = \begin{pmatrix} H_{DD} & H_{DS} & \mathbf{0} \\ H_{SD} & H_{SS} & H_{SA} \\ \mathbf{0} & H_{AS} & H_{AA} \end{pmatrix} \quad (3.4)$$

and is block-diagonalized to

$$H_1' = \begin{pmatrix} E_D & V_{DS} & \mathbf{0} \\ V_{SD} & E_S & V_{SA} \\ \mathbf{0} & V_{AS} & E_A \end{pmatrix} \quad (3.5)$$

using

$$T = \begin{pmatrix} C_{DD} & \mathbf{0} & \mathbf{0} \\ \mathbf{0} & C_{SS} & \mathbf{0} \\ \mathbf{0} & \mathbf{0} & C_{AA} \end{pmatrix} \quad (3.6)$$

and $H_1' = T^{-1}HT$. In eqs 3.4-3.6, the secular equations $H_{kk}C_{kk} = E_k C_{kk}$ ($k = D, S, A$) are solved for the individual donor, solvent and acceptor in the D-S-A electron transfer system. $E_{D/A}$ represents the D/A QD band structure, and the corresponding eigenstate wave functions are $C_{DD/AA}$. The coupled solvent molecules, as a whole, have a band structure in E_S and C_{SS} is the corresponding eigenstate wave functions.

The solvent-mediated LUMO-LUMO coupling is then:^{122,123}

$$V_{DA,s} = \sum_l \frac{V_{DS}^l V_{SA}^l}{E - E_S^l} \quad (3.7)$$

Here E is the tunneling energy, which is estimated as the average band edge energies of the donor (E_D) and acceptor (E_A) QDs, i.e. $E = (E_D + E_A)/2$. Index l represents the l^{th} solvent band state. V_{DS}^l (V_{SA}^l) is the interaction between the donor (acceptor) LUMO and the l^{th} solvent band state.

Similarly, the bridge-mediated electronic coupling is approximated:^{122,123}

$$V_{DA,b} = \sum_l \frac{V_{DB}^l V_{BA}^l}{E - E_B^l} \quad (3.8)$$

where $E = (E_D + E_A)/2$. Index l represents the l^{th} bridge molecular orbital. V_{DB}^l (V_{BA}^l) is the interaction between the donor (acceptor) LUMO and the l^{th} bridge molecular orbital.

Charge perturbation to the TS and TB couplings. When a charged group is introduced into the bridge, the bridge molecular orbital energies (E_B), the solvent band structures (E_S), and the band edge energies of the QDs ($E_{D/A}$) will be changed. The relative energy variations between E_B , E_S and $E_{D/A}$ change the effective tunneling barriers in the D-S-A ($E - E_S$ in eq 7) and the D-B-A ($E - E_B$ in eq 3.8) systems. The E_B change magnitude depends on the electronic property of the bridge molecule and the change become small as the dithiol alkyl unit (dithiol length) increases. The water and QD energy changes (E_S and $E_{D/A}$) depend on their distance to the charge center and the solvent dielectric property. As the QD size grows, the QD wave functions dilute and thus the $E_{D/A}$ change magnitude is expected to decay as well. For positive charge, E_B , E_S and $E_{D/A}$ becomes lower and the negative charge raise these energies.

Upon the charge perturbation placed at the center of the bridge molecule, the bridge molecular orbital wave functions are redistributed among the constituting atoms. When replacing the neutral R group to the negatively charged R group, the two terminal –SH groups of the dithiol bridge have more wave function amplitudes. Therefore, the donor (acceptor)-bridge interaction increases (V_{DB} and V_{BA} in eq 3.8). In contrast, when R is replaced by a positively charged one in the dithiol bridge, the two terminal –SH groups will have less wave function amplitudes, and the donor (acceptor)-bridge interaction decreases. These effects also apply to the solvent eigenstates.

When a charged group is introduced into the bridge, if the charge-perturbed tunneling barrier ($E - E_B$ or $E - E_S$) is comparable to the donor-bridge/solvent and bridge/solvent-acceptor interactions, the deep tunneling conditions are invalid. In this scenario, we should also consider the D-A coupling enhancement due to the resonance tunneling contribution. However, this will alter the specific magnitude of the D-A coupling enhancement, and our general conclusions on the charge effects still hold.

3.3 Parameterization of the charge induced solvent and QD energy changes

Water HOMO and LUMO energy changes in the presence of an external charge.

We used classical molecular dynamic (MD) simulation combined with quantum chemistry calculations to compute the charge effects on the water HOMO and LUMO energies. We solvated CH_3COO^- (NH_4^+) in an explicit 15.0 Å TIP3P water box and added counterion Na^+ (Cl^-) to neutralize the system charge. We used GAFF force field parameters of CH_3COO^- (NH_4^+). We performed MD simulations in the NPT ensemble (constant pressure

at 1 atm, temperature at 300K) molecular dynamics with periodic bound-conditions using AMBER14.¹⁷² The MD was performed for 2 ns with 1 fs time step. The temperature was controlled using the Langevin thermostat with collision frequency 2.0 ps^{-1} . The initial velocities were randomly generated. After the system reached thermodynamic equilibrium, we selected 2000 MD snapshots (separated by every 200 MD steps). For each MD snapshot, we performed quantum mechanics/molecular mechanics (QM/MM) calculations to parameterize the water HOMO and LUMO energy responses to the external charge at selected charge-water distances L ($4 \text{ \AA} - 23 \text{ \AA}$).

In the QM/MM calculations, the QM part consisted of the ion, the counterion and a water molecule. The geometry center-to-center distance between this water and the ion was set as L . The MM part contained other water molecules represented by point charges (TIP3P water model). HF/6-31G* was used for the QM calculations. The water HOMO and LUMO energies were calculated with a block-diagonalization method. In this method, we treated the water molecule as the D block and the ion-counterion as the A block, respectively. For each snapshot, we averaged the water HOMO (LUMO) energies within a spherical shell ($L \pm 0.5$) \AA around the ion center.

The average water HOMO and LUMO energies in eV as a function of the distance L from the NH_4^+ are $-11.2/L - 13.7$ and $-10.8/L + 5.7$, respectively. For CH_3COO^- , the average distance-dependent water HOMO and LUMO energies in eV are $10.8/L - 13.7$ and $9.9/L + 5.7$, respectively. The average HOMO and LUMO energies and the fitted functions are shown in Figure 17. Additional MD and QM/MM calculations have been carried to check the convergence of the derived distance-dependent water HOMO and LUMO energy

variations. From Figure 17, the charge induced energy variations decay fast as L increases. When $L > 17 \text{ \AA}$, the energy change magnitude decreases to less than 15% as compared to that for $L \sim 4 \text{ \AA}$.

Water-water interaction (v_s in eq 4.2). The water LUMO-LUMO coupling without the charge perturbation was computed between two water molecules with the O-O distance fixed at 3.1 \AA . The coupling was obtained by averaging the mutual orientations of the two water molecules. We used HF/6-31G* to perform the quantum chemistry computations along with the block diagonalization method. The averaged LUMO-LUMO coupling is 0.45 eV . The HOMO-HOMO coupling computed in the same way is 0.07 eV .

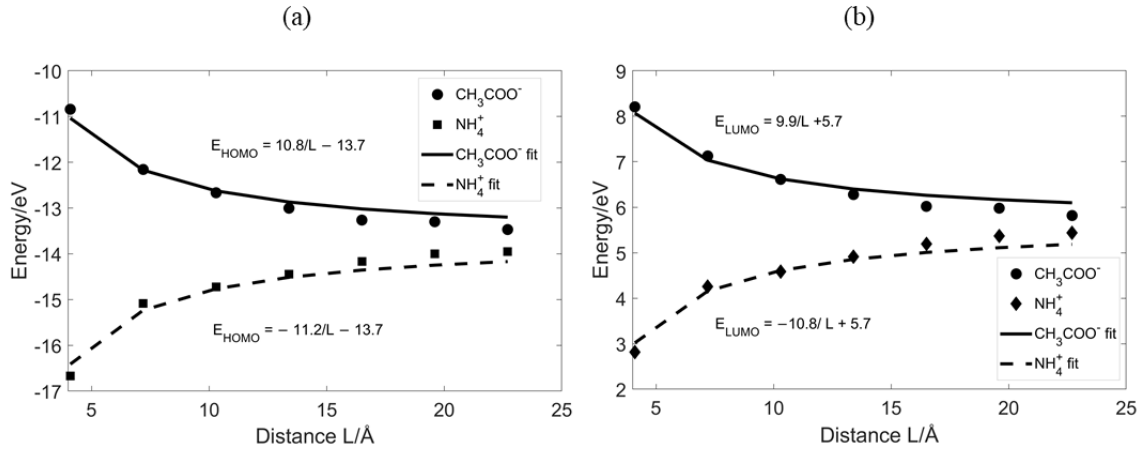


Figure 17: Charge-influenced water frontier orbital energetics. Water HOMO (a) and LUMO (b) energies as a function of distances between the water molecule and the NH_4^+ and CH_3COOH^- ions.

QD band edge energy changes in the presence of external charge. We used $\text{Cd}_{33}\text{Te}_{33}$ and $\text{Cd}_{33}\text{Se}_{33}$ QDs to parameterize the charge perturbed QD band edge energy. The electronic properties of the ^{126,173–176} and $\text{Cd}_{33}\text{Se}_{33}$ QDs were well studied both experimentally and theoretically. They could be calculated with affordable computational

resources, so their charge influenced band edges were used as references for parameterizing size- and distance-dependent band edge energy shifts of the CdTe-CdSe QD dyads. The band edge energy shifts of larger QDs were obtained using energy corrections to the site energies in the tight-bind model (H_D and H_A) based on the Coulomb's law.

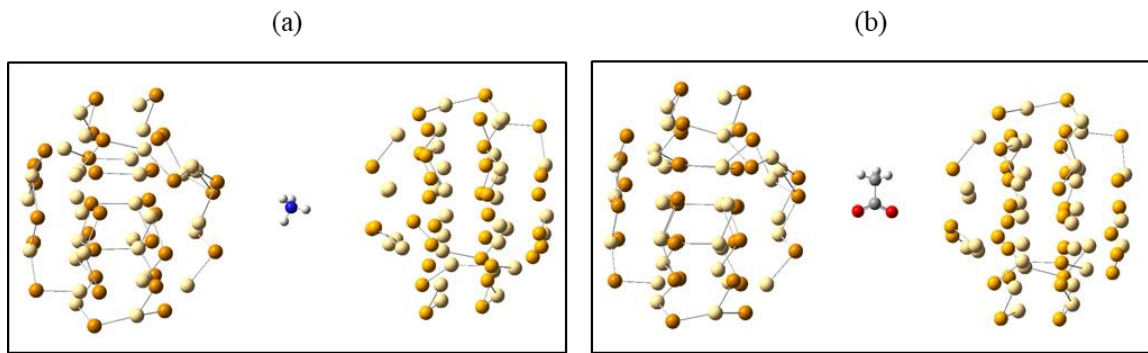


Figure 18: Cd₃₃Te₃₃ and Cd₃₃Se₃₃ dyads with (a) NH₄⁺ and (b) CH₃COO⁻ in between. The ions are 5 Å to each QD surfaces. Water and counterion are not shown.

We used MD simulations to sample the water, QD, and counter-ion configurations. The Cd₃₃Te₃₃ and Cd₃₃Se₃₃ QDs (separated by 1 nm surface-to-surface distance) were fixed in the MD simulation. The NH₄⁺ (CH₃COO⁻) ion was placed midway and fixed between two QDs. (Figure 18) The geometries of the Cd₃₃Te₃₃ and Cd₃₃Se₃₃ QDs were optimized with B3LYP/LANL2DZ level of theory and the geometries of the NH₄⁺ or CH₃COO⁻ ions were optimized with B3LYP/6-31G(d, p) level of theory using Gaussian 16.¹⁷⁷ The QD-ion-QD system was solvated in an explicit 15.0 Å TIP3P water box, and the counterion (Na⁺ for CH₃COO⁻ and Cl⁻ for NH₄⁺) was added randomly. Note, the force field for CdTe and CdSe QDs had not been well established, so that all Cd, Te and Se atoms were replaced with C atoms (hydrogen atoms were used to passivate the surface C atoms) and the general force field for C-H-O-N systems were used. Since the QD atom positions were fixed in the

MD simulations, and only the water and counterion coordinates were necessary in the evaluation of QD HOMO and LUMO energies, this force field replacement produces negligible influence on the evaluation of the QD HOMO and LUMO energy shifts. We performed MD simulations in the NPT ensemble (constant pressure at 1 atm, temperature at 300K) molecular dynamics with periodic bound-conditions using AMBER14.¹⁷² The MD was performed for 1 *ns* with 1 *fs* time step. The temperature was controlled using the Langevin thermostat with collision frequency 2.0 ps^{-1} . The system coordinates were saved every 50 steps for electronic structure calculation after the system reached thermodynamic equilibrium (the final 1000 snapshots were saved).

The system electronic structure was calculated using the QM/MM approach with HF/LANL2DZ QM method. The QM part consisted of the QDs, ion and counterion represented by point charges (TIP3P water model). The total charges were constrained to reside on the ions with the constraint HF method in Q-Chem.^{178,179} The individual QD band edge energies were calculated with a block-diagonalization method similar to eqs 4.4-4.6, but only the HOMO and LUMO energies in the E_D and E_A blocks in eq 4.5 would be needed if the ion and counterion are put into the solvent block of eq 4.4. HOMO and LUMO energies were obtained by averaging over all the MD snapshots.

The valence band edge (HOMO) and conduction band edge (LUMO) energy shifts (ΔE) of $\text{Cd}_{33}\text{Te}_{33}$ and $\text{Cd}_{33}\text{Se}_{33}$ QDs were calculated as the energy differences between QD dyads with and without CH_3COO^- and NH_4^+ (and counterions), and the averaged results are shown in Table 3. The cation raises the HOMO and LUMO energies by $\sim 0.50 \text{ eV}$ and the anion decreases the HOMO and LUMO energies by $\sim 0.25 \text{ eV}$, consistent with the

water results that the negative charge destabilizes the HOMO and LUMO energies and the positive charge stabilizes them. An important factor is the averaged positions of the counter ions because if a positive (negative) ion decreases (increases) the HOMO and LUMO energies, its counterion increases (decreases) them. In the MD simulations of the QD-ion-QD-counterion system, the Cl^- stays $\sim 17 \text{ \AA}$ to the QD centers on average, or $\sim 10 \text{ \AA}$ to the QD surfaces, which is much larger than the 5 \AA ion-QD surface distance. Therefore, the influence from NH_4^+ to the QD energies is much more significant than the influence from Cl^- . For QD- CH_3COO^- -QD systems, the counterion Na^+ stays $\sim 22 \text{ \AA}$ to the QD centers on average, so the influence from CH_3COO^- to the QD energies is also much larger than the influence from Na^+ . In addition, the Na^+ -QD distance is larger than the Cl^- -QD distance, and thus the CH_3COO^- increases the QD energies more than the NH_4^+ decreases the QD energies. The smaller volume of Na^+ compared to Cl^- leads to the differences between the Na^+ -QD distance and the Cl^- -QD distance. As we increase the MD simulation time to 1 ns , the average counterion-QD distances converge.

Table 3: $\text{Cd}_{33}\text{Te}_{33}$ and $\text{Cd}_{33}\text{Se}_{33}$ HOMO and LUMO energy shifts ΔE induced by CH_3COO^- and NH_4^+ ; calculated with HF/LANL2DZ

	$\text{Cd}_{33}\text{Te}_{33}$ HOMO (eV)	$\text{Cd}_{33}\text{Te}_{33}$ LUMO (eV)	$\text{Cd}_{33}\text{Se}_{33}$ HOMO (eV)	$\text{Cd}_{33}\text{Se}_{33}$ LUMO (eV)
CH_3COO^-	0.56	0.51	0.52	0.43
NH_4^+	-0.27	-0.33	-0.23	-0.20

Charge influenced QD band-edge energy change as a function of QD radius with fixed charge-QD distance. We treated the charge group as a point charge, and we placed it 5 Å away from the QD surface. The QD electronic structure was treated with the tight-binding model described in Ref. 5. Because of the charge perturbation, we assumed the site energy for each QD atom was shifted according to the Coulomb's law. We further assumed the atom-atom nearest-neighbor coupling was not changed by the external charge. With this charge perturbed H_D and H_A , we obtained the QD size-dependent band energy changes induced by the external charge. The band energy changes were shifted by corresponding constant energies to reproduce the quantum chemistry computation derived band energy shifts (Table 3) for the $\text{Cd}_{33}\text{Te}_{33}$ and $\text{Cd}_{33}\text{Se}_{33}$ QDs. The pre-shifted band energy changes are shown in Figure 19a. Roughly, the logarithm of the band edge energy change magnitude is linear to the QD radius and the slope is -0.043 \AA^{-1} . Therefore, the QD band edge energy change as a function of QD radius r is $\Delta E_r = \exp(-0.043r + c_1)$, where the constant c_1 values are listed in Table 4.

Table 4: c_1 and c_2 values in calculating the charge-influenced QD band edge energy shifts $\Delta E_r = \exp(-0.043r + c_1)$ ($d = 5 \text{ \AA}$) and $\Delta E_d = \exp(-0.028d + c_2)$ ($r = 8.2 \text{ \AA}$ for CdTe, 7.7 \AA for CdSe) by an external charge

c_1, c_2	CdTe HOMO	CdTe LUMO	CdSe HOMO	CdSe LUMO
-1 charge	-0.23, -0.44	-0.32, -0.53	-0.32, -0.51	-0.51, -0.70
+1 charge	-0.96, -1.17	-0.76, -0.97	-1.14, -1.33	-1.28, -1.47

Charge influenced QD band-edge energy change as a function of the charge-QD surface distance with fixed QD size. Similar to the treatments in obtaining the charge

influenced QD band-edge energy change as a function of the QD radius, the charge influence on the CdTe (radius 8.2 Å) and CdSe QD (radius 7.7 Å) band-edge energy change as a function of the charge-QD surface distance d is $\Delta E_d = \exp(-0.028d + c_2)$, where the constant c_2 values are listed in Table 2.

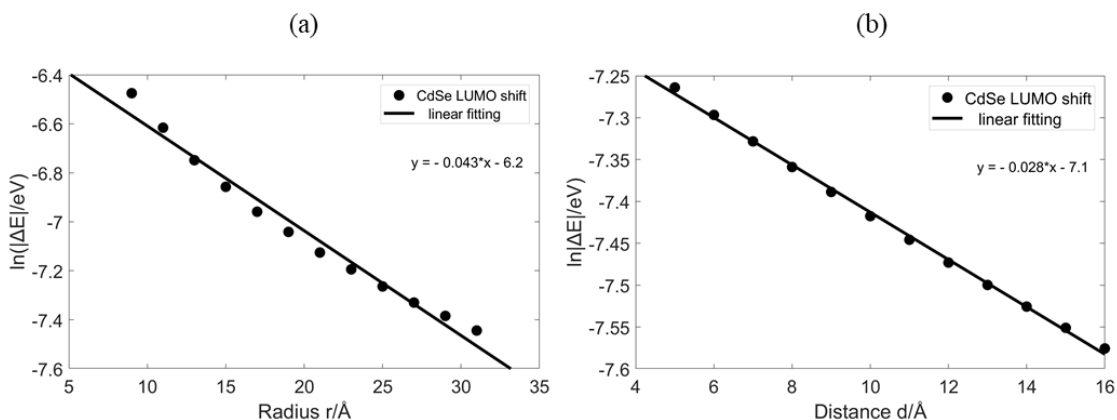


Figure 19: Charge-induced QD band edge shifts calculated using the Coulomb's law as a function of QD radius (a) and the distance (b) from the QD surface to the external charge.

3.4 Results and discussion

With the tight-binding models in eqs 4.1-4.8 and the parameters obtained in Sec III, we first investigated the charge influenced through-solvent and through-bridge couplings for a CdTe-CdSe QD dyad with fixed sizes (CdTe radius is 8.2 Å and CdTe radius is 7.7 Å). This QD pair (QD pair I) approximates the Cd₃₃Te₃₃-Cd₃₃Se₃₃ dyad whose charge transfer couplings have been studied previously.¹⁵⁸ The QDs are linked by the HS(CH₂)_nCH(R)(CH₂)_nSH ($n = 1$; R = -COOH, -COO⁻, -NH₂, -NH₃⁺) dithiol, which sets the QD surface-to-surface distance to be ~ 1 nm. We then investigated the QD distance dependences of the charge influenced TS and TB couplings by varying the dithiol molecule

length (n varies from 1 to 4). We further explored the QD size dependence of the charge-influenced TS and TB coupling. We also discuss the implications on perturbing the charge transfer coupling strength between two QDs by using charged molecular bridges.

3.4.1 Charge induced TS coupling in a QD dyad with fixed QD sizes

Charge effects on TS coupling. The TS coupling between QD pair I was calculated with the tight-binding model described in Sec. II. The surface to surface distance between QDs is 10 Å. The QDs are surrounded by water molecules represented by a lattice. The shortest distance between the QD surfaces and the water lattice edge is 10 Å, with the nearest neighbor water-water distance of 3.1 Å.¹⁷¹ The water lattice size is large enough because the TS coupling plateaus with further increase of the water lattice size. The water LUMO energy under the positive charge (negative charge) as a function of the distance L between the water and the charge center varies as $-10.8/L + 5.7$ eV ($9.9/L + 5.7$ eV). Without charge, the water LUMO energy is 5.7 eV. The water LUMO energy (5.7 eV) and nearest-neighbor coupling (0.45 eV) produce through water coupling decay constant of 0.85 Å^{-1} , which is consistent with typical through-water ET coupling characteristic decay constant of about 0.8 to 0.85 Å^{-1} .¹⁸⁰

The computed TS couplings $|V_{DA,s}|$ between CdTe and CdSe are 8.4×10^{-6} eV (without charge), 3.8×10^{-5} eV (with a positive charge, increased by 350%) and 7.4×10^{-6} eV (with a negative charge, reduced by 12%). These results are listed in Table 5. We define the effective tunneling barrier E_T as the energy difference between the averaged QD LUMO energy and the lowest energy of the solvent band.

Table 5: Tight-binding QD band edges and through-solvent and through-bridge couplings for dithiol with $-\text{COO}^-$, neutral, and $-\text{NH}_3^+$ groups at 5 Å to both QD surfaces; E_T is $E_B - 0.5 * (E_D + E_A)$, where D is CdTe, A is CdSe and B is water (column 4) or dithiol (column 6).

	CdTe LUMO (eV)	CdSe LUMO (eV)	Water solvent band edge (eV)	Though solvent coupling $ V_{DA,s} $ (eV)	Dithiol LUMO (eV)	Through-bridge coupling $ V_{DA,b} $ (eV)
$-\text{COO}^-$	-1.88	-2.22	3.52 $E_T = 5.57$	7.4×10^{-6}	3.53 $E_T = 5.58$	4.4×10^{-6}
neutral	-2.39	-2.65	3.15 $E_T = 5.67$	8.4×10^{-6}	-COOH: 1.46 $E_T = 3.98$ -NH ₂ : 1.26 $E_T = 3.78$	-COOH: 1.0×10^{-5} -NH ₂ : 7.1×10^{-6}
$-\text{NH}_3^+$	-2.72	-2.85	1.23 $E_T = 4.02$	3.8×10^{-5}	-0.86 $E_T = 1.93$	3.5×10^{-6}

Without charge on the bridge, the effective tunneling barrier E_T is 5.67 eV. With the positive charge, E_T decreases to 4.02 eV. The CdTe (CdSe) QD LUMO energy decreases from -2.39 eV (-2.65 eV) to -2.72 eV (-2.85 eV), while the water band edge energy decreases from 3.15 eV to 1.23 eV. The reduced E_T is responsible for the enhanced TS coupling (eq. 9). For an effective through N solvent tunneling pathway, the coupling is approximated by eq 4.9.¹⁸¹ In eq 4.9, V_{DI} and V_{NA} are interactions between D and the solvent site (coupled to D), and between the solvent site (coupled to A) and A, respectively.

V_s is the solvent-solvent nearest neighbor interaction. Inspecting the wave functions of the low energy states in the solvent band structure, we found the low energy TS pathways are mainly formed by the water molecules closed to the positive charge. These pathways are localized around the shortest path (in parallel to the bridge molecule backbone) between two QDs. V_{DI} and V_{NA} values are determined by the v_{ij} values in eq 4.3 and the QD wave function amplitudes and are roughly independent of the external charge.

$$V_{DA,s}' = \frac{V_{D1}V_{NA}}{V_s} \left(\frac{V_s}{E_T}\right)^N \quad (4.9)$$

With the negatively charged bridge, E_T decreases to 5.57 eV compared to the 5.67 eV value for the neutral bridge. In this case, the CdTe (CdSe) QD LUMO energy increases from -2.39 eV (-2.65 eV) to -1.88 eV (-2.22 eV), while the water band edge energy increases from 3.15 eV to 3.52 eV. These two energy increases are very close and the net change in E_T is small, -0.1 eV. However, the computed TS coupling is decreased by the negative charge, although the tunneling barrier E_T is lowered by 0.1 eV. Inspecting the wave functions of the low energy states in the solvent band structure, we found the low energy TS pathways are mainly formed by the water molecules far away from the negative charge. These pathways (detoured pathway) connecting the D and A require more tunneling steps (N in eq 4.9 is large) as compared to pathways localized around the bridge. Since the negative charge is placed in the middle of the molecular bridge, the energy of the water in the short pathways near the molecular bridge is significantly increased, contributing negligibly to the D-A coupling. For the negatively charge bridge, the tunneling steps N is increased and thus is responsible for the decreased TS coupling. The

consequences of the detoured pathways will also affect the QD TS coupling size and distance dependences.

Compared to the neutral bridge system, the TS coupling strength change (reduced by 12%) with negatively charged bridge is weaker than the TS coupling strength change (increased by 350%) with positively charged bridge. This is caused by the cancellation effect between the reduced effective tunneling barrier E_T (enhance the coupling strength) and increased effective tunneling distance (reduce the coupling strength) in the presence of the negative charge.

The change in E_T for the negatively charged bridge is sensitive to the QD LUMO energy change. For small QDs, the QD LUMO energy is highly dependent on the QD geometrical structure. Therefore, it is possible that the increased amounts in the LUMO energies of the QDs are smaller than the increased amount of the dithiol LUMO energy in the presence of a negative charge. In such case, E_T will be increased by the negative charge. The effects of the negative bridge on the effective tunneling barrier and effective tunneling distance will then both decrease the coupling strength, which means the TS coupling strength reduction will be much larger than 12%. In contrast, if the increased amounts in the LUMO energies of the QDs are much larger than the increased amount of the dithiol LUMO energy in the presence of a negatively charged bridge, E_T will be significantly decreased. The effect of the reduced effective tunneling barrier, which enhances the coupling strength, will be much more important than the effect of the increased effective tunneling distance which reduces the coupling strength. In such case, the TS coupling will be strengthened by the negatively charged bridge.

Charge influence on the TS coupling Distance dependence. The TS coupling as a function of the QDs surface-to-surface distance d_s is explored with the tight-binding model. We use the same dyad system as in xxx. The positive and negative charge is placed in the middle position of the molecular linking bridge ($d_s/2$). The computed couplings as a function of d_s for different bridge conditions are shown in Figure 20a. In all distances, the TS coupling in the presence of a positive charge is larger than the TS coupling in the neutral case, which is also larger than the TS coupling in the negative charge case. The differences between the TS coupling strength among the three systems grow as d_s increases. For the neutral QD dyad, the computed coupling distance decay constant β_s dyad 0.85 \AA^{-1} . For the positively and negatively charged bridges, β_s are 0.78 \AA^{-1} and 0.89 \AA^{-1} , respectively. For the super exchange tunneling mechanism, the coupling distance decay constant can be approximated by,

$$\beta_s = -\frac{1+\delta}{d} \ln \left| \frac{V_s}{E_T} \right| \quad (4.10)$$

where $\delta = \frac{d_{eff}}{d_s} - 1$, and $d_{eff} = Nb$. N is the solvent site number in eq 4.9 and b is the distance between two adjacent solvent sites. For the positively charged bridge, $d_{eff} \approx d_s$, so that $\delta \approx 0$. The positive charge lowers the effective tunneling barrier E_T , therefore weaken β_s . For the negatively charged bridge, the dominant tunneling pathways are far away from the charge center, so that the effective pathway length $d_{eff} \gg d_s$ or $\delta > 0$. Therefore, the negatively charged bridge has larger β_s , compared to the neutral and positively charged bridges.

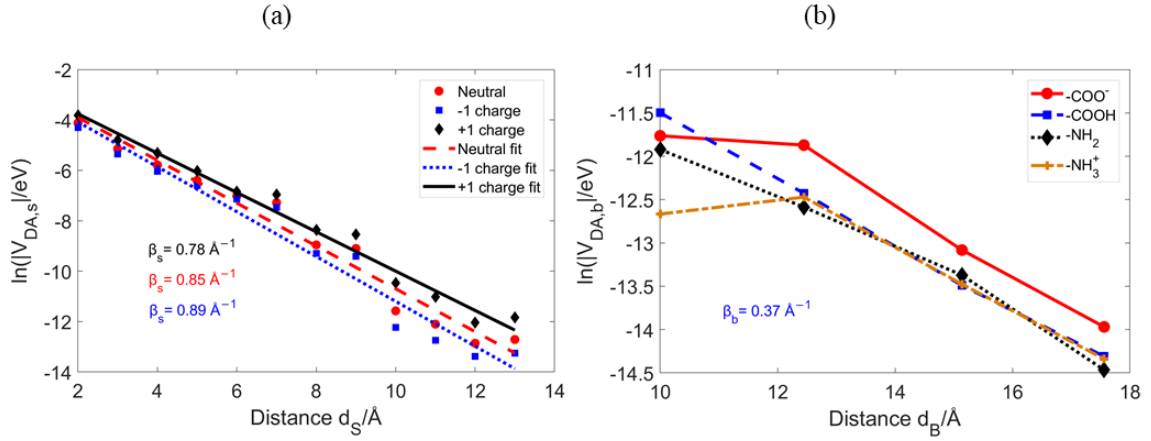


Figure 20: Charge influenced distance-dependent through-solvent and through-bridge QD-QD couplings . Through-solvent (a) and through-bridge (b) coupling as a function of the surface-to-surface distance between two QDs. The radii of the CdTe and CdSe QDs are 8.2 Å and 7.7 Å, respectively. The dithiols used in (b) are $\text{SH}(\text{CH}_2)_n\text{CH}(\text{R})(\text{CH}_2)_n\text{SH}$ ($n = 1, 2, 3, 4$; $\text{R} = -\text{COOH}, -\text{COO}^-, -\text{NH}_2, -\text{NH}_3^+$).

3.4.2 Charge induced TB coupling in a QD dyad with fixed QD sizes

Charge influence on the TB coupling. We computed the through-bridge coupling between the CdTe and CdSe QDs as a function of the surface-to-surface distance d_s . The variation of d_s is achieved by changing the length (n) of the bridging dithiols $\text{SH}(\text{CH}_2)_n\text{CH}(\text{R})(\text{CH}_2)_n\text{SH}$ ($n = 1, 2, 3, 4$; $\text{R} = -\text{COOH}, -\text{COO}^-, -\text{NH}_2, -\text{NH}_3^+$). The same CdTe and CdSe QDs as above were used. The computed $\ln|V_{DA,b}|$ for different bridges as a function of d_s are shown in Figure 20b. In general, the TB donor-acceptor coupling between the QDs linked by the negatively charged dithiols is larger than the coupling between the QDs linked by the neutral bridge and positively charged dithiol, except for the short bridge length ($n = 1$). For $n > 1$, The computed distance decay constant β_b values are similar for neutral and charged bridges. These results are caused by the opposite contributions to the D-A TB coupling from the charge induced the tunneling barrier

($E_T = E - E_B$) changes and from the D-B and B-A interaction changes (V_{DB} and V_{BA}). (see eq 4.8)

At the small d_S ($n = 1$), the computed charge influenced TB coupling values and the effective tunneling barrier E_T are shown in the last two columns of Table 5. E_T is defined by the energy difference between the dithiol LUMO energy (E_B) and the average QD LUMO energy (E). By changing the substituent group from $-\text{COOH}$ to $-\text{COO}^-$, the through-bridge coupling $|V_{DA,b}|$ is decreased from 1.0×10^{-5} eV to 4.4×10^{-6} eV (by 56%); Similarly, $|V_{DA,b}|$ is decreased from 7.1×10^{-6} eV to 3.5×10^{-6} eV (by 51%) by changing the substituent group from $-\text{NH}_2$ to $-\text{NH}_3^+$. Replacing $-\text{COOH}$ to $-\text{COO}^-$ increases the bridge LUMO energy from 1.46 eV to 3.53 eV, while the CdTe (CdSe) LUMO energy is increased from -2.39 eV (-2.65 eV) to -1.88 eV (-2.22 eV). Thus, effective tunneling barrier E_T increases from 3.98 eV to 5.58 eV. The increased E_T weakens the TB D-A coupling (eq 4.8). On the other hand, the negatively charge group on the bridge pushes the bridge electronic wave functions towards two $-\text{SH}$ terminals, enhancing the donor (acceptor) - bridge interactions (V_{DB} and V_{BA} terms in eq 4.8). The increased V_{DB} and V_{BA} interactions strengthen the TB D-A coupling (eq 4.8). The overall charge induced effects on the TB D-A coupling are determined by the relative contributions from the increased tunneling barrier and the enhanced donor (acceptor) - bridge interactions. For the short dithiol bridge ($n = 1$), the electrostatic interactions between the $-\text{COO}^-$ group and the $-\text{SH}$ terminals are strong. The increased tunneling barrier by these electrostatic interactions has more impact on the TB coupling than the enhanced donor (acceptor) - bridge interactions.

For the long dithiol bridges ($n > 1$), the electrostatic interactions between the $-\text{COO}^-$ group and the $-\text{SH}$ terminals are weak, and the wave function redistribution effects have more influence on the TB coupling than the tunneling barrier change.

When changing $-\text{NH}_2$ to $-\text{NH}_3^+$, similar analysis can be made for the tunneling barrier change and the V_{DB} and V_{BA} interaction changes. The $-\text{NH}_3^+$ substituent decreases the tunneling barrier and pulls the bridge electronic wave functions away from the two $-\text{SH}$ terminals, weakening the V_{DB} and V_{BA} interactions. The relative contributions of the decreased tunneling barrier and the weakened donor (acceptor) - bridge interactions to the overall TB coupling strength determine the positively charged bridge effects on the TB coupling strength change. (eq 4.8)

The electronic polarizability of the QDs and the linker molecule under the electric field generated by the charged group on the linker molecule determines the tunneling barrier change and the donor (acceptor)- bridge interaction change. The charge induced TB coupling thus depends on the electronic properties of the QDs and linker molecules in different QD dyads. For bridge linked QD dyads in which the tunneling barrier increase contribution is less than the donor (acceptor)- bridge interaction increase contribution, the TB coupling between the QDs will increase.

The computed coupling distance decay constant β_b values in the CdTe-CdSe QD dyad are found to be independent of the charge on the dithiol bridge. The derived β_b value is $\sim 0.37 \text{ \AA}^{-1}$, which is consistent with the β_b in our previous study.⁵ The tunneling barrier (E_T) change and the charge induced dithiol unoccupied orbital wave function redistribution impose opposite influences on the TB coupling change as the D-A distance varies. As the

bridge length increases, the change in E_T and the change in the dithiol wave function redistribution both decrease because the charged group has less influence on the longer dithiol backbone and the QDs compared to the shorter one. Therefore, the β_b values of the QD dyads with the charged bridges have negligible differences compared to the β_b values of the QD dyads with the neutral bridges. Note, the β_b values also depend on the specific QDs and the linker molecule used to construct the QD dyad.

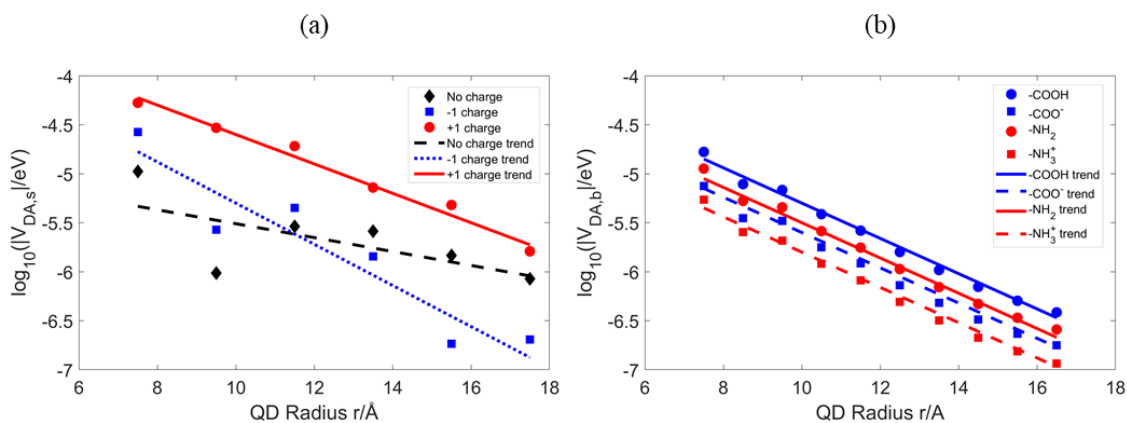


Figure 21: Charge influenced QD size-dependent through-solvent and through-bridge QD-QD couplings . Left panel for TS and right panel for TB.

3.4.3 QD size-dependent TS and TB couplings influenced by charged bridges

Charge influence on the QD size dependent TS coupling. We investigated the TS coupling between two QDs of varying sizes at a fixed QD surface-to-surface distance 10 Å using the tight-binding model described in Section II. The two QDs have the same radius and are connected by the neutral or charged dithiols molecules mentioned above. The computed through-solvent coupling $\log_{10}|V_{DA,s}|$ for different bridge charge conditions as a function of the QD radius r are shown in Figure 21a.

For the positively charged molecular bridges, the computed TS coupling strengths between the two QDs decrease as the QD radii r increases from 7.5 Å to 17.5 Å, and the coupling strength is always larger than that of the QDs linked by the neutral bridge. The TS coupling strength difference between the positively charged dithiol system and the neutral dithiol system decreases as the QD size grows. These results are caused by different changes in the effective tunneling barrier and the tunneling pathway for different bridge charge conditions as the QD size grows. The QD conduction band edge (LUMO) energy decreases as the QD size grows. Therefore, the through solvent tunneling barrier increases (eq. 7), resulting in the decreased D-A coupling, as the QD size grows. The bridge charge perturbation to the solvent molecule energetics is limited by the solvent-charge distance (see Fig. 4b). For large QDs, there are more contributions to the D-A coupling from solvent pathways whose tunneling barriers are weakly perturbed by the distant charge localized on the molecular bridge. Therefore, as the QD size grows, the TS coupling is no longer dominated by the pathways around the molecular bridge, and all the solvent molecules between the whole contact region (between the two facing hemispheres of the QDs) contribute to the D-A coupling. The portion of low-energy pathways in the total pathway becomes small. Therefore, the increase in the D-A coupling strength becomes smaller as the QD size grows.

For two QDs linked by a negatively charged molecular bridge, the QD-QD TS coupling is stronger for small QDs ($r < 12$ Å) and becomes weaker for large QDs ($r > 12$ Å) as compared to the TS coupling between two QDs linked by a neutral molecular bridge. In contrast to the positive charge influence on the D-A TS coupling, the negative charge

influenced tunneling barrier and tunneling pathway changes may contribute oppositely to the D-A TS coupling, depending on the QD size. The overall D-A TS coupling is mainly determined by the charge influenced tunneling barrier as the QDs size varies.

For small QDs, the tunneling barrier reduction due to the negative charge influence contributes positively to the D-A coupling. However, these low tunneling barrier pathways have long tunneling distance (detoured pathways, much longer than the QD surface-to-surface distance, see Sec. III.1), contributing negatively to the D-A coupling. In our calculations, for small QDs studied in this section, the barrier reduction effects on the D-A coupling change dominate, therefore the D-A coupling becomes stronger when replacing the neutral bridge to a negatively charged bridge. For general QDs, whether the D-A coupling is enhanced or weakened depends on the dominance of the tunneling barrier reduction and the increased tunneling distance. This is different from positive charge perturbations to the D-A coupling, where the D-A coupling is enhanced.

As QDs size grows, the QD conduction band edge (LUMO) energy decreases, thus the tunneling barrier reduction becomes small, and eventually the through solvent tunneling barrier may become larger than that of the neutral bridge. Therefore, the contribution to the D-A coupling strength variation caused by the tunneling barrier change becomes negative as the QD sizes grow. At the same time, for large QDs, there are more solvent tunneling pathways which have comparable tunneling distances to the QD surface-to-surface distance and have tunneling barriers weakly perturbed by the negative charge. Compared to the small QD case, the negative contribution to the D-A coupling caused by the increased tunneling distance becomes small. Nevertheless, both the tunneling barrier

and distance changes contribute negatively to the D-A coupling, resulting in a steeper D-A coupling decay (as QD sizes increase) compared to the case with a neutral molecular bridge. The specific coupling decay rate depends on the relative electronic responses of the solvent and QDs to the external charge and their mutual distances. For large D-A distances, the bridge charge influence on the D-A coupling QD size dependence becomes small.

Charge influenced TB coupling size dependence. We computed the through-bridge donor-acceptor coupling for the CdTe-CdSe QD dyad linked by the $\text{HS}(\text{CH}_2)_n\text{CH}(\text{R})(\text{CH}_2)_n\text{SH}$ bridge when $n = 1$ ($\text{R} = -\text{COOH}, -\text{COO}^-, -\text{NH}_2, -\text{NH}_3^+$). For each of the four dithiols, the computed TB coupling as a function of the QD radius with fixed QD surface-to-surface distance is shown in Figure 21b. Two QDs have the same radii in the plots. The TB coupling value $|V_{DA,b}|$ drops with the increasing QD radius r and the TB coupling QD size dependence is insensitive to the bridge charge. Both the positively and negatively charged substituent in the dithiol bridge decrease $|V_{DA,b}|$ for all r .

As we discussed earlier, the TS D-A coupling change is regulated by two effects: the tunneling barrier shift and the wave function redistribution of the bridge unoccupied orbitals induced by the bridge charged substituent group. The two effects contribute oppositely to the D-A coupling changes (see discussions in Sec. III.1). For short molecular bridges ($n=1$), we found the D-A couplings are reduced for both charged bridges. The slope of the $\log_{10}|V_{DA,b}|$ vs. r is mainly determined by the reduced QD wave function amplitude on each constituent atom as the QD sizes grow. In our tight-binding model, one atom from the donor QD and one atom from the acceptor QD couple to the bridge molecule. Therefore, as the QD sizes grow, V_{DB} and V_{BA} (see eq 8) decrease. The $\log_{10}|V_{DA,b}|$ vs. r

function is not necessary linear, because the QD wave functions are not exponential functions of r . The specific decay rate depends on the composition of the QDs and the bridge molecules.

3.4.4 Tuning QD-QD charge transfer couplings using charge influenced TS and TB couplings

In the experiments, dithiols like 1,3-benzenedithiol are often used to link the QDs to obtain closely packed QD assemblies, where the QD surface-to-surface distance is ~ 1 nm.¹⁸² This distance corresponds to the surface-to-surface distance in the CdTe-CdSe QD dyad linked by HSCH₂CH(R)CH₂SH (R = -COOH, -COO⁻, -NH₂, -NH₃⁺) in this study.

D-A coupling strength influenced by charged groups in the molecular bridge for small QDs. Our current calculations showed that changing R in the HSCH₂CH(R)CH₂SH dithiol from neutral to charged group (-NH₂ to -NH₃⁺ and -COOH to -COO⁻) can enhance the overall D-A coupling strength for small QDs (QD radii $r < 12$ Å). The enhancement magnitude is more pronounced in smaller QDs. For example, for the CdTe ($r = 11.5$ Å) and CdSe ($r = 11.5$ Å) QD dyad, the overall D-A coupling strengths for the QD dyad linked by positively and negatively charged bridges are all one order of magnitude larger than that of the corresponding neutral bridges (positive group : 1.1×10^{-6} eV vs 1.8×10^{-5} eV; negative group: 2.7×10^{-7} eV vs 3.3×10^{-6} eV). The D-A coupling enhancements are contributed by the increased TS couplings due to the charge perturbations. In both cases the TB coupling strength are reduced by the charge perturbations.

D-A coupling strength influenced by charged groups in the molecular bridge for large QDs. For large QDs ($r > 12$ Å), replacing the neutral R group in the

HSCH₂CH(R)CH₂SH dithiol neutral with a positively charged one can enhance the D-A coupling, while the change of a neutral R group to a negatively charged group can weaken the D-A coupling. The positive charge induced D-A coupling enhancement becomes weaker as the QD size grows. In contrast, the negative charge induced D-A coupling reduction will be more pronounced in larger QDs. For example, for the CdTe ($r = 17.5 \text{ \AA}$) and CdSe ($r = 17.5 \text{ \AA}$) QD dyad, the overall D-A coupling strength for the QD dyad linked by positively (negatively) charged bridge is 70% larger (smaller) than that of the corresponding neutral bridges (positive group : $9.9 \times 10^{-7} \text{ eV}$ vs 1.7×10^{-6} ; negative group: $1.1 \times 10^{-6} \text{ eV}$ vs $3.2 \times 10^{-7} \text{ eV}$). The positively charged group induced D-A coupling enhancement arises from the larger contribution from the increased TS coupling strength than from the decreased TB coupling strength by the positive charge perturbation. The negatively charged group induced D-A coupling decrease is caused by the decreased TS and TB coupling due to the negative charge perturbation.

TS and TB coupling dominance switch as the QD size change. We found in our previous study¹⁵⁸ that the TB D-A coupling strength in the CdTe-CdSe QD dyad separated by a surface-to-surface distance $\sim 1 \text{ nm}$ decays faster than the TS D-A coupling strength as the QD sizes grow. We found that the TS and TB coupling mechanisms switch their dominance when the CdTe and CdSe QD radius $r_{switch} \sim 15 \text{ \AA}$ (although the overall D-A coupling decreases as the QD sizes grow). The TB coupling strength can be one order of magnitude larger than the TS coupling strength when $r < 15 \text{ \AA}$. In contrast, the TS coupling strength can be one order of magnitude larger than the TB coupling strength $r > 15 \text{ \AA}$. The switch of the dominant coupling mechanism arises from the fact that the increasing surface

area of the QD partially compensates for the wave function dilution effect for the TS coupling.

In the current calculations, we found the coupling mechanism switch occurs at a smaller QD size when a positively charged R group replaces the neutral one, because of the increased through-solvent coupling for all size QDs. In our calculation, the r_{switch} reduces from 12 Å to a value smaller than 7.5 Å. The specific r_{switch} value depends on the specific system, but the feature that the mechanism switch occurs at smaller QDs could be general. For the negatively charged group, the coupling mechanism switch occurs at a larger QD size compared to the neutral R group case, because the negatively charged group in the bridge increase the TS coupling strength decay rate as the QD sizes grow. In our calculations, r_{switch} increases from 12 Å to 16 Å when replacing COOH with -COO^- .

Tuning the relative strength between the TS and TB couplings can be important when we want to control ET through selected mechanism (TS or TB). For example, to improve the chiral induced spin selectivity (CISS) effect,¹⁶²⁻¹⁶⁶ it is important to exclude the electron transfer contributions from non-spin selectivity channels to the total electron transfer rates. Often electron transfer through chiral bridge is responsible for the CISS effect, thus it is advantageous to reduce the TS coupling strength and enhance the TB coupling. Our calculations suggest that a negatively charged group in the bridge can change the ratio of TB to TS coupling strength from 34% to 126% for two QDs with radii ~ 16 Å when the bridge changes from $\text{HSCH}_2\text{CH}(\text{COOH})\text{CH}_2\text{HS}$ to $\text{HSCH}_2\text{CH}(\text{COO})\text{CH}_2\text{HS}^-$. For longer dithiols, the TB to TS coupling strength ratio change may be larger since the -COO^- group in longer dithiols increases the TB coupling strength

(while it decreases the TB coupling strength for the short dithiol HSCH₂CH(COOH)CH₂HS). (Figure 20b)

Solvent impact. Water is used as the solvent in our calculations. The screening effect of the high dielectric constant of water limits the charge influence on the frontier orbital energies of the water molecules which are distant from the bridge charge center. For less-polar solvents with low dielectric constant, the charge influence on the solvent frontier orbital energies can be stronger and can extend to longer distances. While the low dielectric constant effect on the effective tunneling barrier depends on the relative frontier orbital energy changes of the QDs and the solvent molecules, its effect on tunneling pathway can be more significant. Therefore, the less-polar solvents might magnify the charge effects on the D-A coupling on large QDs.

3.5 Summary

We built a tight-binding model to investigate the charge influenced through-solvent (TS) and through-bridge (TB) electron transfer couplings between the CdTe and CdSe QDs linked by neutral and charged dithiols HS(CH₂)_nCH(R)(CH₂)_nSH bridge ($n = 1, 2, 3, 4$; R = -COOH, -COO⁻, -NH₂, -NH₃⁺). We studied the charge induced D-A coupling changes and their dependences on the QD size and on the QD surface-to-surface distance.

We found that the positively charged group -NH₃⁺ in the dithiol bridge increases the overall computed QD-QD coupling strength by up to 1 order of magnitude for all QD sizes and QD surface-to-surface distances. -NH₃⁺ influenced D-A coupling strength decays faster than -NH₂ as the QD sizes grow with fixed QD surface-to-surface distance. And -

NH_3^+ lowers the D-A coupling distance decay constant. These influences of $-\text{NH}_3^+$ charge on D-A coupling properties arise from the TS contribution perturbed by the positive charge. The positive charge influenced TS coupling strength is up to 1 order of magnitude larger than the TS coupling strength for the neutral bridge. In contrast, the $-\text{NH}_3^+$ group in the molecular bridge has negligible influence on the TB coupling strength for long dithiols ($n > 1$) and decreases the TB coupling by $\sim 50\%$ for the short dithiol ($n = 1$), independent of the QD sizes. As a result of the relative changes in TS and TB coupling strengths induced by the positive charge, the TB to TS dominance switch occurs at smaller QD sizes as compared to the neutral molecular bridge.

We found that the effects of the negatively charged group $-\text{COO}^-$ in the dithiol on the overall computed D-A coupling strength depend on the CdTe and CdSe QD sizes. For small QDs (radius $< 12 \text{ \AA}$), when the charged group in the dithiol bridge changes from $-\text{COOH}$ to $-\text{COO}^-$, the strength change in the D-A coupling strength is sensitive to the QD radii; for large QDs (radius $> 12 \text{ \AA}$), the $-\text{COO}^-$ in the dithiol decreases the D-A coupling strength between the QDs by up to 70%. The $-\text{COO}^-$ influenced D-A coupling strength decays faster than $-\text{COOH}$ group as the QD sizes grow with fixed QD surface-to-surface distance. And the $-\text{COO}^-$ increases the D-A coupling distance decay constant. These impacts of $-\text{COO}^-$ charge on the D-A coupling properties are from the TS coupling contributions perturbed by the negative charge. The negative charge influenced TS coupling strength is sensitive to the QD radii when the QD radii are $< 12 \text{ \AA}$ and can be ~ 1 order of magnitude smaller than the TS coupling strength for neutral bridge linked QDs

when the QD radii are $> 12 \text{ \AA}$. In contrast, the $-\text{COO}^-$ influenced TB coupling strength between the QDs is $\sim 50\%$ less than the TB coupling for the neutral bridge when dithiol is short ($n = 1$); for the long dithiols ($n > 1$), the $-\text{COO}^-$ group increase the TB coupling strength by $\sim 50\%$. Because of the relative changes in TS and TB coupling strengths induced by the negative charge, the TB to TS dominance switch occurs at larger QD sizes as compared to the neutral molecular bridge.

For the through-solvent QD-QD coupling, the bridge charge induced strength change is a consequence of the relative contributions from the tunneling barrier shift and from the effective pathway length change because of the charge in the bridge. For the through-bond coupling, the bridge charge induced strength change is a result of the relative contributions from the tunneling barrier shift and from the donor (acceptor)-bridge interaction change induced by the bridge charge. The charge induced donor (acceptor)-bridge interaction change arises from the QD unoccupied orbital wave function redistribution under the electric field generated by the bridge charge.

We suggest that the charged substituents can be used to tune the QD-QD coupling strength and the dominant charge transfer mechanism in the QD dyad linked by a bridging molecule. Specifically, the $-\text{NH}_3^+$ substituent can be used to strengthen the D-A coupling between the QDs separated by 1,3-propanedithiol. For the CdTe-CdSe QD dyad separated by the same dithiol, the $-\text{COO}^-$ substituent can be used to strengthen the D-A coupling for small QDs and to weaken the coupling for large QDs. Both the $-\text{NH}_3^+$ and the $-\text{COO}^-$ substituent groups can be used to switch the charge transfer mechanism from through-

bridge dominant to through-solvent dominant tunneling in small CdTe-CdSe QD dyads linked by 1,3-propanedithiol. These findings provide strategies to control the charge transfer rates, charge recombination rates and their mechanisms in QD solar cells, NP-based batteries and QD-based photoelectrochemical sensors using charged linker species.

4. Solar Cell Performance Using Quantum Dot Triad Charge-separation Engines

In this chapter, we use kinetic modeling to explore the solar cell performance of quantum dot dyads and triads based solar cells. This collaborative work with Peng Zhang (Duke University), Brian P. Bloom (University of Pittsburgh) and David H. Waldeck (University of Pittsburgh) has been published on *J. Phys. Chem. C*, 2018, 122 (11), pp 5924–5934.

4.1 Introduction to kinetics in QD dyad and triad

While the size-tunable physical and electronic properties of semiconductor quantum dots (QDs) make them attractive for potential solar cell applications, QD-based photovoltaics remain limited by charge recombination processes that compete with the transduction of the initial photogenerated exciton into photocurrent.^{10,17,19,183} One design strategy to improve efficiencies is to engineer the band energetics to promote charge separation. Here, we explore the use of higher-order assemblies of QDs, namely QD triads, to realize improvements in device performance. The proposed triad motif has two QDs in contact with the electrodes (one with the anode and one with the cathode) and a third intervening QD to enhance the charge separation efficiency. The three QDs are designed to have a cascading band-edge energy alignment (see Figure 22a) that promotes both electron transfer (ET) and hole transfer (HT).^{184–189}

Simpler two layer QD assemblies have been used for QD solar-cell architectures and have led to efficiencies of 10.6%.^{87,190} In a two-layer CdTe-CdSe QD solar cell design, both QDs act as light absorbers and produce charge carriers, where an ~ 5 nm CdTe QD

has a band gap of ~ 1.8 eV, and an ~ 4 nm CdSe QD has a band gap of ~ 2.1 eV.^{33,38,88,91,191–194} Absorption of light in dyad systems can cover a wider range of the solar spectrum, compared to single QD-sensitized solar cells. Type-II energy band alignment (Figure 22b) for the QDs enhances ET from a photoexcited CdTe QD to a CdSe QD and HT from a photoexcited CdSe QD to a CdTe QD. Type II band alignment also slows back electron transfer, compared to the case for type-I band alignment.^{38,89,192,195} For a CdSe QD electron acceptor, the energy difference between its conduction band and the valence band of a CdTe QD is more favorable for charge recombination in type-II QDs than for type-I QDs because the non-radiative charge recombination is disfavored by the Marcus inverted effect in type-I heterojunctions.^{96,196} Nevertheless, charge recombination is believed to limit the power conversion efficiency of QD solar cells^{197,198,199} and can dominate over the device advantages of type-II architectures, which arise from the large forward charge transfer rates and the small differences between electron and hole transfer rate constants. The ET rates, HT rates and their differences in the type-II architectures can be controlled by tuning the ligand structure and the QD sizes, which determine the electronic energy landscape.¹⁵⁸

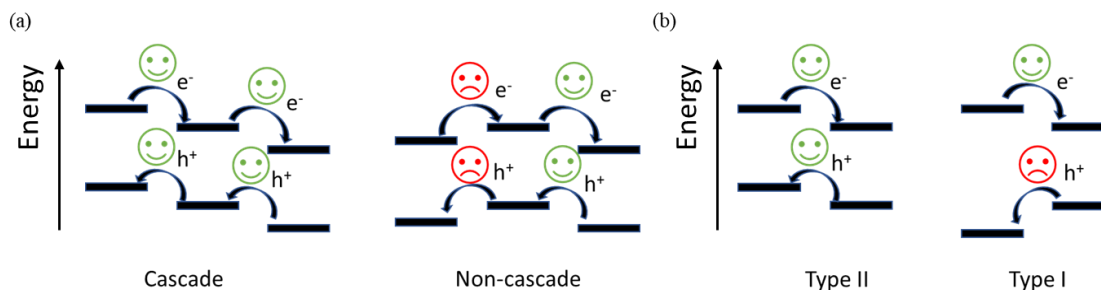


Figure 22: Band alignment between CdTe and CdSe QDs . Cascade versus non-cascade energy landscapes for (a) QD triads and (b) QD dyads. All ET and HT processes are thermodynamically favored in the cascade energy alignment scheme. In the non-cascade scheme, at least one of the ET and HT processes is

thermodynamically unfavorable. Panel (b) shows Type-II vs Type-I energy landscapes for dyads. Both ET and HT are thermodynamically favored for Type-II energy alignment, while one charge-transfer step is thermodynamically disfavored for-Type I energy alignment.

Multi-layered QD thin-film solar cells typically exhibit increased energy-conversion efficiencies compared to single-layer cells.^{78,94,193,194,200,201} The high efficiency of multilayered QD thin-films is usually explained by the large short-circuit current that results from the large number of QD absorbers in the device.^{193,201} For example, a tandem-layered QD triad solar cell structure was found to produce a 3.0% power conversion efficiency, as compared to the 1.65% efficiency for a single layer large band gap QD solar cell.¹⁹⁴ Multi-chromophore organic solar cells²⁰² were found to have short-circuit currents that changed from 2.5 mA/cm² to 4.5 mA/cm² when a donor platinum tetra-benzoporphyrin was linked to an organic dye acceptor with an unsaturated bridge. Molecular triad architectures were also shown to have larger ET yields than the yield found in molecular dyad systems.^{203–208} In a trilayer organic solar cell, with an ET energy cascade but a flat valence band profile, an ~ 2-fold increase in power conversion efficiency was observed. The increase in efficiency was mostly realized in the short-circuit current.²⁰⁹

The open-circuit photo-voltage deficit, or the gap between the experimentally measured and the theoretically estimated open-circuit photo-voltages, is believed to be the main cause of the diminished performance of most QD solar cells.^{87,95,190,210–215} This deficit is caused primarily by charge recombination at the interfaces, via surface states that lie in the energy gap between the conduction and valence bands. Strategies to reduce these charge recombination effects are needed to increase the open-circuit photo-voltage and to

further improve QD solar cell performance. Inspired by multi-layer solar cell designs and by a need for strategies to reduce charge recombination, we studied the effect of introducing a third QD in a CdTe/CdSe QD heterojunction. The general design principles that we explore are: (1) introduce a middle QD that absorbs light and generates charge carriers, in addition to the absorption and carrier generation provided by the outer CdTe and CdSe QDs of the triad; (2) use the middle QD to slow charge recombination because of the additional spatial separation it provides between the photogenerated and separated electron and hole; and (3) use the electron/hole spatial separation to weaken the electron–hole Coulomb attraction, lowering the exciton binding energy and enhancing the free carrier generation efficiency. The middle QD, which benefits the overall charge separation, however, can slow the overall rate of charge flow in the cell because of the increased inter-electrode distance associated with adding the third QD. It is thus important to attain a balance between these opposite effects to produce improved device performance.

In this chapter, we analyze the properties of QD dyad and QD triad charge transfer structures between electrodes. The dynamics are analyzed using a master equation approach, akin to that applied earlier to organic photovoltaic solar cells.^{216–218} In the earlier studies, electron donor-acceptor systems were embedded in a photovoltaic cell and steady-state currents and powers were analyzed as a function of bias voltage. The open-circuit photo-voltage (U_{OC}) was found to decrease as the charge recombination rate increased.²¹⁸ Using detailed balance constraints, U_{OC} values in those studies were found to depend on the ratio of the temperature and the ‘sun temperature’ (given by the sun’s blackbody temperature).^{218,219} The non-radiative recombination rates and the exciton binding energy

decrease the open-circuit voltage to an extent that depends on the electronic energies of the donor and acceptor. We analyze how adding a third QD (moving from a dyad to a triad) can suppress charge recombination and enhance the overall charge-transfer yield. The dyad and triad QD systems studied have more electronic states than are included in simple dyad organic solar-cell models.^{216,218} We investigate the current and power characteristics of the dyad and triad structures to determine the power conversion efficiencies. The charge flux produced by the photo-excitation drives charge separation across the electrodes, and input/output powers are calculated using steady-state analysis. The influences of non-radiative charge recombination and of QD energy band alignment on the currents and power conversion efficiencies are explored.

4.2 Theory and kinetic models for QD dyad and triad systems

4.2.1 Master equations in QD dyad and triad

The QD solar cell dyad model includes a left QD (L), a right QD (R), and two electrodes (cathode Λ and anode Y , see Figures 23a,b). The QD triad model (Figure 23a) has an additional QD (M) that is located between the L and R QDs. Each QD has four accessible states: neutral (L, M, R), excited (L^* , M^* , R^*), positively charged (L^+ , M^+ , R^+), and negatively charged (L^- , M^- , R^-). Thus, each QD dyad has 16 possible states (4^2) and each QD triad has 64 possible states (4^3). Excitation, radiative decay, electron transfer, hole transfer, charge injection to and from the electrodes, and non-radiative charge recombination are included in the model. However, we assume that charge transfer only

occurs between nearest-neighbor QDs. For example, the kinetic equation governing the population of the L^+R^* state of the QD dyad (Figure 23c) is

$$\begin{aligned} \frac{d [L^+R^*]}{d t} = & -(k_{Rd} + k_{RLe} + k_{L\Lambda h} + k_{RLc} + k_{RYe}) [L^+R^*] \\ & + k_{Rex}[L^+R] + k_{LRe}[L^*R^+] + k_{ALh}[LR^*] + k_{YRe}[L^+R^+] \end{aligned} \quad (4.1)$$

where k_{Rd} is the radiative decay rate constant of R, k_{Rex} is the excitation rate constant of R, k_{RLe} (k_{LRe}) is the electron transfer rate constant from R to L (L to R), $k_{L\Lambda h}$ (k_{ALh}) is the hole transfer rate constant from L to Λ (Λ to L), k_{RYe} (k_{YRe}) is the electron transfer rate constant from R to Y (Y to R). The intrinsic non-radiative decay rate of a single QD is incorporated in k_{RLc} . The kinetic equation for L^+M^*R in the QD triad system is:

$$\begin{aligned} \frac{d [L^+M^*R]}{d t} = & -(k_{YRe} + k_{L\Lambda h} + k_{MLc} + k_{MLE} + k_{MRe} + k_{MRh} + k_{Md} + k_{Rex}) [L^+M^*R] \\ & + k_{Mex}[L^+MR] + k_{LMe}[L^*M^+R] + k_{RMh}[L^+M^-R^+] + k_{Rd}[L^+M^*R^*] \\ & + k_{ALh}[LM^*R] + k_{RYe}[L^*M^*R^-] + k_{RMe}[L^+M^+R^-] \end{aligned} \quad (4.2)$$

k_{MLc} is the charge recombination rate constant from M to L, k_{MLE} (k_{LMe}) is the electron transfer rate constant from M to L (L to M), k_{MRe} (k_{RMe}) is the electron transfer rate constant from M to R (R to M), k_{MRh} (k_{RMh}) is the hole transfer rate constant from M to R (R to M), and the other rate constants are defined in analogy with those in eq 4.1. The other 15 kinetic equations for the dyad and the other 63 kinetic equations for the triad are constructed in analogy with eqs 4.1 and 3.2. See the Appendix A for the equations governing the dyad.

4.2.2 Charge transfer rates in QD dyad and triad systems

CT rates. The ET and HT rate constants (k_{ct}) between two states in the charge-transfer network are modeled using the non-adiabatic ET rate in the high-temperature (Marcus) limit^{108,109}:

$$k_{ct} = \frac{2\pi}{\hbar} |V_{DA}|^2 \frac{1}{\sqrt{4\pi\lambda_{ct}k_B T}} \int dE g(E) \exp\left(-\frac{(\Delta_r G + E + \lambda_{ct})^2}{4\lambda_{ct}k_B T}\right) \quad (4.3)$$

where E is the electron energy relative to the acceptor band edge, \hbar is Planck's constant divided by 2π , k_B is Boltzmann's constant, T is the temperature, V_{DA} is the electronic coupling between two QDs, λ_{ET} is the reorganization energy, $\Delta_r G$ is the reaction free energy, and $g(E)$ is the density of electronic states for the acceptor QD, approximated using

$$g(E) = (Volume) \frac{(2m^*)^{\frac{3}{2}}}{2\pi} \sqrt{E} \quad (4.4)$$

In eq 4.4, m_p is the effective mass of the transferred charge; $m^* = m_e^*$ for electron transfer and $m^* = m_h^*$ for hole transfer. $\Delta_r G$ is taken as the energy difference between the relevant QD band edges (HOMO and LUMO positions) under zero-bias conditions. The reorganization energy λ_{ct} is calculated using the Marcus two-sphere model,¹⁰⁸ and it is ~ 0.15 eV for the CdTe and CdSe QDs in Figure 23b, where the free energy for ET is ~ 0.26 eV and for HT is ~ 0.52 eV, which means that both ET and HT are in the normal Marcus region. Note that detailed balance between the forward and reverse charge transfer rates is guaranteed by eq 4.3, so it is used to compute the rate constants in eqs 4.1 and 3.2.

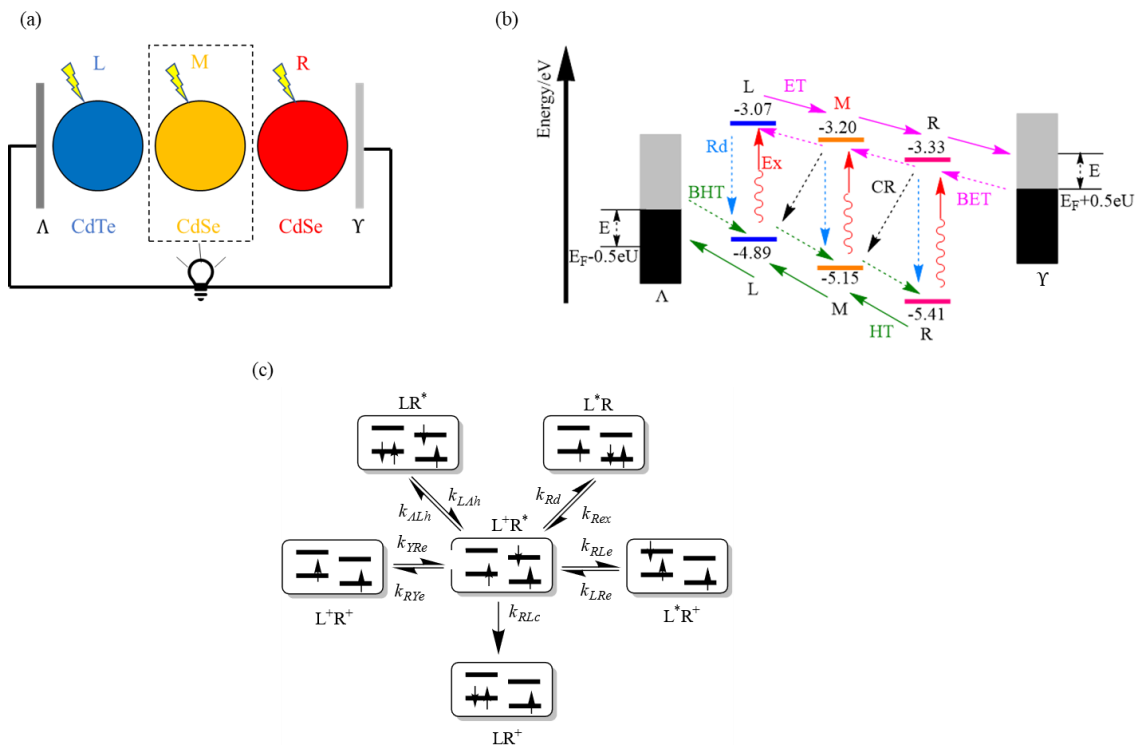


Figure 23: Schemes of charge transfer network in CdTe-CdSe based solar cell
(a) Schematic diagram of a QD triad architecture. (b) The energy diagram for the triad structure in (a) and for all of the photo-excitation (Ex)/radiative decay (Rd), ET/back ET (BET), HT(BHT), and charge recombination (CR) processes in the triad solar cell of the QD triad system. The HOMO and LUMO energies of the L and R QDs are indicated for a 5.5 nm CdTe QD and a 4.5 nm CdSe QD.^{33,38} The middle (M) QD is modeled to have LUMO and HOMO energies equal to the average values of the corresponding L and R QD energies and a 5.0 nm diameter. The Fermi energies of the electrodes are shifted symmetrically by external applied potentials U , so that each electrode has an $0.5eU$ energy shift. (c) Kinetic schemes for the states and ET steps associated with the $L+R^*$ state in the QD dyad.

The QD triad energy landscape is shown in Figure 23b. A QD dyad solar cell similar to ITO-CdTe-CdSe-Al is used as a reference in our analysis. The metal electrodes are assumed to have an equal Fermi energy (of -4.1 eV), for simplicity. The QD triad has the same energetics for the L and R QDs as in the dyad, but it also contains a middle CdSe QD, M, with a 5.0 nm diameter (unless stated otherwise). In addition, we assume that the

M QD has its band-edge energies tuned by its capping ligands.^{54,87} Note that chemical composition, QD radius, and capping ligands can all be used to tune the band energetics. The photoexcitation rate (Ex), radiative decay rate (Rd), ET/back ET (BET) rates, HT/back HT (BHT) rates, and charge recombination (CR) rate for the triad cell are indicated in Figure 23b. The rate constants for these processes in the dyad system are shown in Figure 23c.

The hole-transfer rate from the HOMO of L to the left electrode Λ is modeled as,¹⁸¹

$$k_{L\Lambda h} = \frac{v_{\Lambda}}{\sqrt{4\pi\lambda_{\Lambda}k_{BT}}} \int dE f(E) \exp\left[-\frac{(\Delta_r G + E + \lambda_{\Lambda})^2}{4\lambda_{\Lambda}k_{BT}}\right] \quad (4.5)$$

with

$$f(E) = \frac{1}{[\exp(\frac{E}{k_{BT}}) + 1]} \quad (4.6)$$

and the term $v_{\Lambda} = \frac{2\pi}{\hbar} |V_{L\Lambda}|^2$, where $V_{L\Lambda}$ is an effective electronic coupling between L and the electronic states of electrode Λ . The contributions to $\Delta_r G$ from the electronic energies are calculated using the HOMO energy for L and the applied chemical potential (the Fermi level, E_F , plus the bias voltage U) of Λ . E is the energy difference between a hole state of the HOMO of L and the Fermi edge of electrode Λ . λ_{Λ} is the reorganization energy for hole transfer from L to the left electrode and is estimated with the Marcus two-sphere model with the radius of the left electrodes set to infinity. The HT rate for the reverse process has $f(E)$ replaced by $[1 - f(E)]$ in eq 4.5, and $(\Delta_r G + E)$ replaced by $-(\Delta_r G + E)$. For ET from R to the right electrode Y , $f(E)$ in eq 4.5 is replaced with $[1 - f(E)]$ and v_{Λ} is replaced with v_Y .

The rate of QD photoexcitation is $k_{ex} = A_s n_s(x_s)$, where $n_s(x_s) = 1/[\exp(x_s) - 1]$ is the Bose-Einstein distribution for the photons and $x_s = E_g/k_B T_s$, where $E_g = E_{LUMO} - E_{HOMO}$, T_s is the sun's black-body temperature, and A_s is the Einstein A coefficient for absorption.²²⁰ The corresponding radiative decay rate, $k_{Rd} = A_s[1 + n_s(x_s)]$, satisfies a relationship that is similar to a detailed balance condition under constant solar radiation, and is characterized by the T_s value defined above,²²¹

$$\frac{k_{ex}}{k_d} = \exp[-(E_{LUMO} - E_{HOMO})/k_B T_s] \quad (4.7)$$

Charge Recombination rates. Effective charge recombination at the QD-QD interfaces are assumed to occur from the M QD to the L QD with a rate of k_{MLc} , and from the R QD to the M QD with a rate of k_{RMc} in the triad. For the dyad, only charge recombination from the R QD to the L QD with a rate constant of k_{RLc} is included. The effective rates include the intrinsic non-radiative decay in a single QD and other charge recombination via surface states in k_{RLc} , k_{MLc} and k_{RMc} . Nearest-neighbor charge recombination rates depend mainly on surface states, and we assume that the nearest-neighbor charge recombination rate k_{RLc} for the dyad and the nearest-neighbor charge recombination rates for the triad, k_{MLc} and k_{RMc} , are similar. The specific values of the solar cell current, voltage, and power conversion efficiencies will change depending on mismatches among the three rate constants, but the general conclusion that a M QD can improve the QD dyad solar cell performance is robust. The charge recombination rates depend on the reorganization energy, the localized surface states, and the reaction free

energy. These values are held fixed in our simulations. We use one effective rate constant (two rate constants in the triad) to describe charge recombination.

4.2.3 Dyad and triad-based cell properties

We normalize the population of all states (e.g., the states in Figure 23c) to 1, and the steady-state master equations are written as $Ac=0$, where c is the vector for the populations of all states and A is the coefficient matrix for the master equations. Solving the equation $Ac=0$ is to solve the null space of matrix A , which is done by using the *null* function of MATLAB. The steady-state populations of the states of the R QD and Y electrode are $c_1, c_2, c_i...c_n$ and the associated ET rate constants are $k_1, k_2, k_i...k_n$. Here i denotes an ET process. The steady-state circuit current (I_c) is defined as the net current from the QD dyad/triad system to the electrode,

$$I_c = \sum_{i=0}^n (-1)^s c_i k_i \quad s = 0, 1 \quad (4.8)$$

The integer $s=0$ represents the current from the R QD to Y , and $s = 1$ represents the current from Y to the R QD.

The photo-induced excitation current (I_{ex}) is calculated by summing the transition ‘current’ from the HOMO to the LUMO levels for each QD. If the concentrations for the ground state QDs (e.g., LM^+R and LMR^-) is $g_1, g_2, g_3...g_m$, and the rate constants for these states to be photoexcited are $k_{ex1}, k_{ex2}, k_{ex3}...k_{exm}$ (ex indicates excitation),

$$I_{ex} = \sum_{i=0}^m g_i k_{exi} \quad (4.9)$$

For example, g_1 corresponds to the LMR^+ state of the triad, and k_{Ex1} corresponds to the excitation rate of the $LMR^+ \rightarrow L^*MR^+$ process. The excitation power P_{ex} is defined as,

$$P_{ex} = \sum_{i=0}^m g_i k_{Exi} \Delta E_i \quad (4.10)$$

where ΔE_i is the energy of the i th excited states.

Steady-state power conversion efficiency (PCE). Using the kinetic equations described above, steady-state photocurrents and photo-voltages can be calculated (see SI for details). The maximum output power P_{max} of the system is defined as the maximum of the product of the photocurrent I_c and the chemical potential difference between the electrodes, $U = E_A - E_Y$, where E_A and E_Y are the chemical potentials of the A and Y electrodes, respectively. The external quantum efficiency (EQE) is defined by the ratio of P_{max} to the input power P_{in} :

$$\eta_{ex} = \frac{P_{max}}{P_{in}} \times 100\% = \frac{\max(I_c \cdot U)}{P_{in}} \times 100\% = \frac{I_{SC} \cdot U_{OC} \cdot FF}{P_{in}} \times 100\% \quad (4.11)$$

Here, I_{SC} is the short-circuit current, U_{OC} is the open-circuit voltage, and FF is the fill factor. EQE is a measure of the light to electrical energy power conversion efficiency. In our analysis, the input power P_{in} is taken to be constant, and we compare the values of P_{max} for dyads and triads, namely $\frac{\eta_{ex,dyad}}{\eta_{ex,triad}} = \frac{P_{max,dyad}}{P_{max,triad}}$. Assuming that all QDs have an equal probability of photoexcitation, P_{in} of the triad systems is 50% larger than that for the dyad because of the additional QD. Thus, we normalize I_{SC} and P_{max} for system size.

We also study the internal quantum efficiency η_{in} , which is the ratio of the maximum output power to the photo-excitation power in the case of maximum output power,

$$\eta_{in} = \frac{P_{max}}{P_{ex}} \times 100\% \quad (4.12)$$

Here, P_{ex} is the power associated with light absorption. This parameter represents the efficiency of energy conversion from the photoexcited QDs to electrical power in the circuit.

System parameters. To calculate the current-voltage values for the solar cells, we use the parameters in Table 6. Since the dielectric constant of the bare CdTe and CdSe QDs is ~ 7 and the dielectric constant of 1,2-ethanedithiol is approximately 41,²²² we use an intermediate value of 20 for the assembly. The dielectric constant determines the reorganization energy and thus impacts the charge transfer rates (see SI for further discussion). The influence of the dielectric constant on I_{SC} , U_{OC} , P_{max} , and on efficiencies is examined by varying the ET and charge recombination rates. As we explore the influence of the band-edge (HOMO and LUMO) energies for the M QD on I_{SC} , U_{OC} , P_{max} and on the efficiencies, the parameters in Table 6 will change as described.

Table 6: Parameters used in the current-voltage, output power-voltage, and efficiency calculations.

	Value	Notes
ϵ_s	20	Dielectric constant of the QD assembly; arbitrarily estimated as the average dielectric constant of the complex of the CdTe/CdSe QDs and surface ligands.
r_{DA}	1 nm	Surface to surface distance between neighboring QDs; about the end-to-end distance of the extended SH(CH ₂) ₂ SH molecule

R_L , R_M , R_R	2.75 nm, 2.50 nm, 2.25 nm	Radii of L, M and R QDs, respectively
E_A	$(-4.1 - 0.5e\Delta U)$ eV	Left electrode potential; -4.1 is the Fermi energy of the left A metal electrode; ΔU is the applied external potential and e is the magnitude of the electron charge.
E_Y	$(-4.1 + 0.5e\Delta U)$ eV	Right electrode potential; -4.1 is the Fermi energy of the right Y electrode;
V_{DA} and V_{ED}	10^{-4} eV	Electronic coupling between $\text{Cd}_{33}\text{Te}_{33}$ and $\text{Cd}_{33}\text{Se}_{33}$ QDs linked by $\text{SH}(\text{CH}_2)_2\text{SH}$; surface to surface distance ~ 1 nm
ν_S	10^8 s^{-1}	Inverse of the characteristic time scale for QD excitation and decay
ν_Y, ν_A	$10^8 \text{ eV} \cdot \text{s}^{-1}$	$2\pi/\hbar$ coupling ² value for ET/HT between QD and electrodes
T	300 K	Room temperature
T_s	6000 K	‘Sun surface temperature’
m_e^*	0.1 a.u.	Effective electron mass of CdTe and CdSe ^{127,223,224}
m_h^*	0.1 a.u.	Effective hole (light) mass of CdTe and CdSe ¹²⁷

4.3 Solar cell performance of QD dyad and triad systems.

We first describe the current-voltage (I - U) relations for dyads and triads as the charge recombination rate is varied and the HOMO (LUMO) energy of M is fixed at the average value of the HOMO (LUMO) energies of L and R. The I - U characteristics enable the calculation and analysis of the open-circuit voltages, the short-circuit currents, and the power-voltage (P - U) curves. The maximum output powers are also extracted from the P - U relations. Next, the internal quantum efficiencies for the dyad and triad systems are analyzed as a function of the charge recombination rates. The dependence of the external and internal quantum efficiency on the middle QD energetics, effective hole mass (see SI), and quantum dot radii are explored. Finally, we relate our findings to recent investigations aimed at improving the open-circuit voltage for PbS-based QD solar cells.

4.3.1 I - U and P - U characteristics of QD assemblies

The characteristic I_c - U and P - U relations that are computed for QD dyad and triad systems follow the predictions of the Shockley diode model,^{225,226} and behave more ideally (i.e., like an ideal diode²²⁶) than is found in experiments^{36-38,83} (see Figure 24). The current changes modestly as the voltage increases from 0 V to ~ 1.2 V, but drops to 0 nA (and then to negative values) as the voltage increases to ~ 1.5 V. See SI section SI.4 for discussion of the decrease in I_c as U increases. Figure 23b indicates that the energy difference between the LUMO of R and the HOMO of L is 1.56 eV, and that the open-circuit voltage is ~ 1.5 V, consistent with other theories and models.^{218,221,227,228} The output power P_{out} initially increases with the applied potential, but decreases rapidly when the external potential continues to rise. P_{max} decreases as the charge recombination rate increases from 10^7 s^{-1}

to 10^{12} s^{-1} ; the value of the potential where P_{max} occurs also changes with the charge-recombination rates. As the nearest-neighbor charge-recombination rate for both the dyad and triad increases, the peak position of P_{out} shifts to the left on the voltage axis first, and then shifts back to the right on the voltage axis, for both the dyad and triad. The peak position of P_{out} first shifts left due to the increase in charge recombination rates because the I_c-U curves in Figure 24a shift left (U_{OC} decreases) as the recombination rate increases; the peak position of P_{out} shifts right as the charge recombination rate increases because the I_c-U curves in Figure 24a shift down and the flattening tails of the I_c-U curves disappear as the recombination rate constant increases. Note that the nature of the I_c-U curves is different for the dyad and triad systems; the triad has a larger efficiency than the dyad regardless of the recombination rate.

The short-circuit current (I_{SC}), the open-circuit voltage (U_{OC}), the maximum output power (P_{max}), and the power conversion efficiency (η_{in}) are extracted from the I_c-U and $P-U$ curves and plotted in Figure 26.

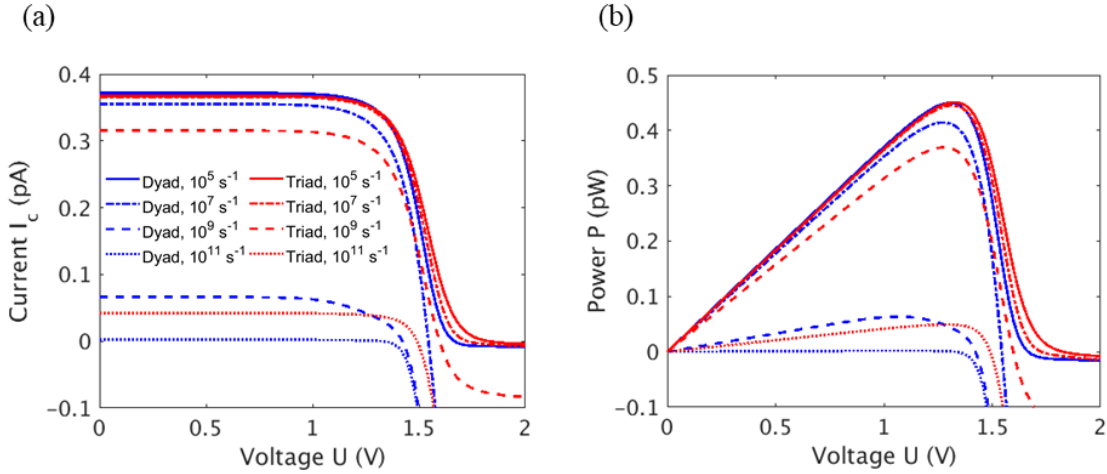


Figure 24: Current-Voltage and Power-Voltage curves. (a) $I_c - U$ and (b) $P - U$ curves for the QD dyad (blue) and triad (red) systems with different charge recombination rates, 10^5 s^{-1} (solid), 10^7 s^{-1} (dash-dot), 10^9 s^{-1} (dashed), and 10^{11} s^{-1} (dotted). The current and output power are normalized by factors of 2 and 3 for the dyad and triad, respectively. See Figure 25 for details of the $I_c - U$ curves near the open-circuit voltage.

When the charge recombination rate is large ($>10^7 \text{ s}^{-1}$), the current I_c drops rapidly and then nearly linearly to zero as the voltage approaches the open circuit voltage. However, when the charge recombination rate is small ($<10^7 \text{ s}^{-1}$), the current I_c has an exponentially decaying tail. Charge recombination dominates the processes that reduces the positive current generated by ET and HT. As the voltage increases, the backward current increases. If the CR rate is large, the net current I_c drops rapidly to zero as the voltage increases. If the CR rate is small, the net current I_c drops slowly to zero as the voltage increases. In experiments, the charge recombination rates are usually large compared to the ET and HT rates, and only the former case is observed.

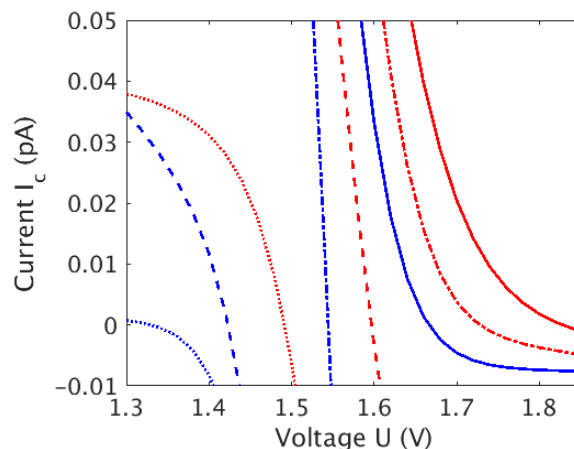


Figure 25: Detailed current-voltage curve near open-circuit voltage. Enlarged I - U characteristic curves near the open-circuit condition for QD dyad (blue) and triad (red) systems for different charge recombination rates, 10^5 s^{-1} (solid), 10^7 s^{-1} (dash-dot), 10^9 s^{-1} (dashed), and 10^{11} s^{-1} (dotted).

4.3.2 Short-circuit current I_{SC} , Open-circuit voltage U_{OC} , Maximum output power, P_{max} and Internal efficiency η_{in}

Short-circuit current I_{SC} . As the charge recombination rate increases, the I_{SC} (Figure 26a) decreases from picoamps to femtoamps, consistent with theoretical estimates of Einax et al.²¹⁸ based on similar kinetic analysis of organic solar cells. If we use a 5 nm QD to define the device area, the current densities for the dyad and triad are $\sim 40 \text{ mA/cm}^2$ and 150 mA/cm^2 , respectively. Increasing the charge recombination rate reduces the charge flux to the electrodes and thus decreases I_{SC} . The dyad has slightly larger I_{SC} values than the triad when the charge recombination rate is less than 10^6 s^{-1} . The addition of the M QD decreases the nearest neighbor ET and HT rates compared to those of the dyad because the corresponding processes involve a reduced $\Delta_r G$ for each step in the triad. Therefore, the improvement of the current caused by the presence of the M QD is not caused by an enhancement of individual ET and HT rates. The M QD adds another step in the ET and

HT chains, which slows the overall charge transfer between the electrodes. If the charge recombination rate is sufficiently small ($< 10^6 \text{ s}^{-1}$), the current in the system will depend mainly on the ET and HT rates, and the dyad will have a slightly larger external efficiency (see Figure 26c). If the charge recombination rate is large enough ($> 10^7 \text{ s}^{-1}$) however, it will reduce the current in the dyad more than it does for the triad. In this limit, the additional QD slows the charge recombination more than it slows the ET and HT rates. Hence, the triad system has a larger short-circuit current. The value of the charge recombination rate at which the short circuit current of the dyad and triad systems switch (the intersection point in Figure 26a) is $\sim 5 \times 10^7 \text{ s}^{-1}$, which is significantly less than the ET and HT rates ($\sim 10^{10} \text{ s}^{-1}$). The maximum improvement in I_{SC} for the triad vs. the dyad is around 0.25 pA (378%) and occurs when the charge recombination rate is $\sim 10^9 \text{ s}^{-1}$. This indicates that the additional QD in the triad system is most useful when the charge recombination rate is of the order of the ET and HT rates; reducing the charge recombination rate always increases the short-circuit current.

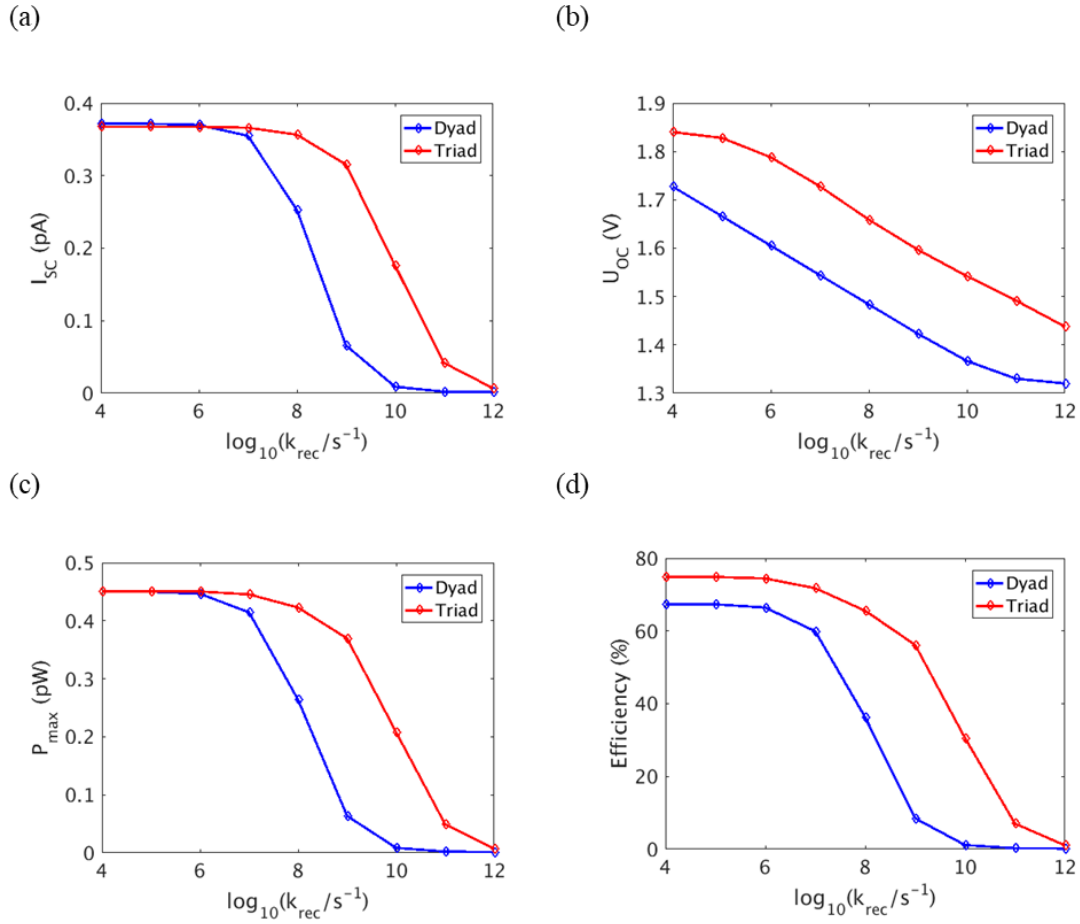


Figure 26: Solar cell performance comparisons between QD dyad and QD triad based solar cells. (a) Short-circuit current, (b) open-circuit voltage, (c) maximum output power, and (d) internal quantum efficiency η_{in} for the QD dyad (blue) and triad (red) solar cell systems as a function of the log of the charge recombination rate, k_{rec} . This analysis uses $k_{rec} = k_{RLc} = k_{MLc} = k_{RMc}$.

Open-circuit voltage U_{OC} . The open-circuit voltage U_{OC} also decreases with an increase in the charge recombination rate (see Figure 26b). The triad U_{OC} decreases from 1.85 V to 1.44 V, and the dyad U_{OC} decreases from 1.73 V to 1.32 V as the charge recombination rate changes from $10^4 s^{-1}$ to $10^{12} s^{-1}$. The computed U_{OC} is relatively large compared to the experimental results.^{36,38,192} Note that U_{OC} correlates positively with the

energy difference between the LUMO of R and the HOMO of L, which is 1.56 eV. This value is derived from the optical gaps of single CdTe and CdSe QDs, and is overestimated compared to electrochemical measurements.³³ A comparison of the dependence of U_{OC} on the charge recombination rate between the dyad and triad finds that the QD triad system always has a higher open-circuit voltage than that of the QD dyad, by ~ 0.18 V (13%). The middle QD in the triad system reduces the effective non-radiative charge recombination rate in the system between the two outer QDs, which increases the open-circuit voltage independent of k_{RLC} .^{216,218} A 13% improvement in U_{OC} is obtained with the parameters in Figure 26b for the triad compared to the dyad, however larger improvements for the triad vs. dyad can be expected for other donor-acceptor systems with different band-edge energy levels for L and R.

Maximum output power, P_{max} . The maximum output power as a function of the recombination rate (Figure 26c) resembles the short-circuit current as a function of the recombination rate. Both P_{max} of the dyad and triad decrease with increasing charge recombination rates, and P_{max} of the dyad and triad are equal to each other when the charge recombination rate is $< 10^6$ s⁻¹, which is slightly smaller than the charge recombination rate value that is found for the scenario when I_{SC} of the dyad and triad are equal to each other, because the triad U_{OC} value is always larger than that of the dyad. If the charge recombination rate is $\sim 10^9$ s⁻¹ (close to the ET and HT rate), P_{max} for the triad is more than four times larger than that of the dyad. As with the I_{SC} , decreasing the charge recombination rate when it is near the ET/HT rate is an effective way to increase P_{max} ; however, once the charge recombination rate is below 10^6 s⁻¹ (below 1% of the HT and

ET rates), it has little influence on the maximum power. P_{max} determines the EQE (see eq 4.11) for fixed P_{in} , and thus the QD triad systems are more efficient than the QD dyad systems when the charge recombination rate is comparable to the charge-separation rates. The improvement in the EQE can be very dramatic if the charge-recombination rate is comparable to the charge-transfer rates.

Internal efficiency η_{in} . Figure 26d shows the internal quantum efficiency η_{in} as a function of the recombination rate. η_{in} has a sigmoidal dependence on the logarithm of the recombination rate and decreases as the charge recombination rate increases for both the triads and dyads. A smaller charge recombination rate leads to a larger number of charge carriers moving to the electrodes, so η_{in} increases as the charge recombination rate decreases. The theoretical limit for η_{in} is determined by the excitation and decay rates, or by the energy gaps of the QDs. The value of η_{in} for the triad is always larger than the value for the dyad. For example, if the charge recombination rate is 10^9 s^{-1} , the triad η_{in} is 56% and the dyad η_{in} is 8%; if the charge recombination rate is 10^{10} s^{-1} , the triad η_{in} is 31% and the dyad η_{in} is 1%. When the charge recombination rate is close to the ET/HT rates, using a QD triad architecture is a particularly effective strategy to slow the overall recombination and raise the internal quantum efficiency.

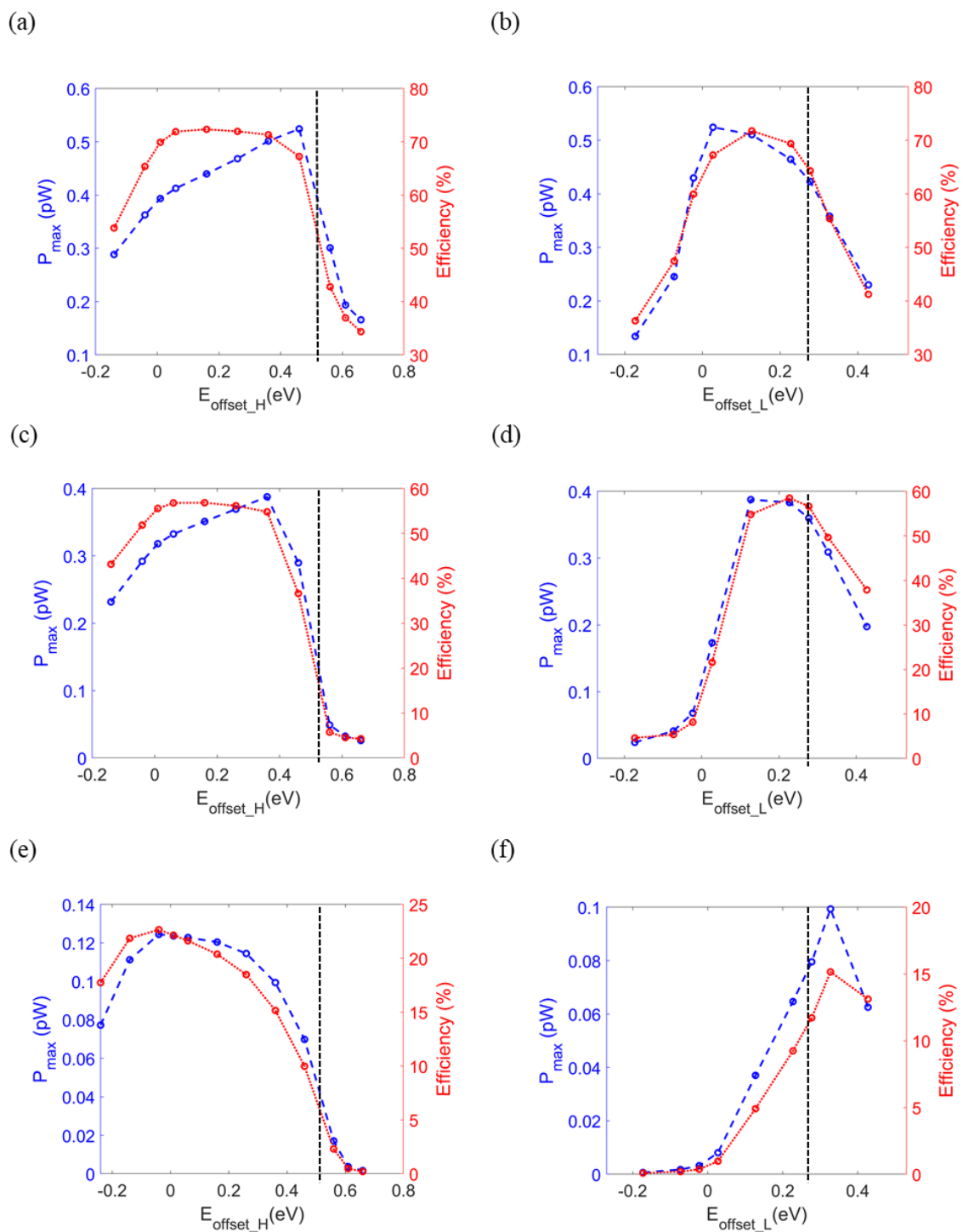


Figure 27: Effects of mediate QD band edge energies on PCE . Maximum output power (blue and dashed, left vertical axis) and internal quantum efficiency (red and dotted, right vertical axis) as a function of the HOMO (a, c and e) and LUMO (b, d and f)

(b, d and f) energy offsets of the middle QD relative to the HOMO and LUMO energies of the R QD. For (a) and (b), the charge recombination rate is 10^5 s^{-1} ; for (c) and (d), the charge recombination rate is 10^9 s^{-1} ; for (e) and (f), the charge recombination rate is 10^{11} s^{-1} . The HOMO and LUMO band edge offsets of the L QD with respect to the R QD are shown by the vertical lines in the figures.

4.3.3 Effects of the M QD energy offsets (HOMO and LUMO) on the triad performance

The cascading energy band alignment of the triad shown in Figure 22b is used in the above analysis, and the HOMO and LUMO energy levels of M were fixed in the previous simulations to examine how the solar cell performance changes as the charge recombination rates vary. Changing the HOMO and LUMO energies of M alters the excitation/decay rates, the charge transfer rates, and the backward charge transfer rates that modify the triad performance. We studied how the band edge energies of M influence P_{max} and η_{in} for three given charge recombination rates: 10^5 s^{-1} , 10^9 s^{-1} , and 10^{11} s^{-1} . The HOMO (LUMO) energy of M was varied in ranges centered on the fixed HOMO (LUMO) energies of the L and R QDs. The HOMO (LUMO) energies of the L and R QDs were taken at -4.89 eV (-3.07 eV) and -5.41 eV (-3.33 eV), respectively, so that the HOMO (LUMO) energy offset of L with respect to R is 0.52 eV (0.26 eV).

Figures 27a, c, and e show the maximum output power (P_{max} , eq. 3.11) and internal quantum efficiency (η_{in} , eq. 3.12) as a function of the HOMO energy offset (E_{offset_H}) of M. Figures 27b, d, and f show P_{max} and η_{in} as a function of the LUMO energy offset (E_{offset_L}) of M. As the E_{offset_H} value increases from -0.2 eV to 0.6 eV , or as the E_{offset_L} value increases from -0.2 eV to 0.4 eV , P_{max} and η_{in} first increase and then decrease. P_{max} reaches a maximum when E_{offset_H} is $\sim 0.46 \text{ eV}$ and E_{offset_L} is $\sim 0.03 \text{ eV}$, while η_{in} reaches a

maximum when E_{offset_H} is ~ 0.16 eV and E_{offset_L} is ~ 0.13 eV for a charge recombination rate of 10^5 s^{-1} (Figure 27a). As the charge recombination rate increases (from 10^5 s^{-1} to 10^{11} s^{-1}), P_{max} and η_{in} have their largest values for lower E_{offset_H} values and larger E_{offset_L} values. The charge recombination rates are taken to be energy independent. However, changes in band-edge offsets change the overall ET rates from L to R and the overall HT rates from R to L. The maximum in the P_{max} and η_{in} values with respect to the E_{offset_H} of the M QD arise because the HT rate from R to M and the HT rate from M to L change in opposite directions as E_{offset_H} varies. Similarly, the maximum in the P_{max} and η_{in} values with respect to the M QD E_{offset_L} value arises because the ET rate from L to M and the ET rate from M to R vary in opposite directions as E_{offset_L} grows.

In our model (eq. 3.3), the overall HT rate through the triad is determined by $k_{RMh}k_{MLh}/(k_{RMh}+k_{MLh})$, and the dependence of the rate constants (k_{RMh} and k_{MLh}) on the acceptor QD's density of states (eq. 3.4) make the overall HT rate sensitive to the energy band offsets. A decrease (increase) of the band edge energy difference between L and M (between M and R) increases (decreases) the acceptor density-of-states, so it increases (decreases) the HT rate. While P_{max} depends on the net current between QDs, η_{in} depends on the ratio of the net current between QDs to the photoexcitation rate. Thus, these parameters depend somewhat differently on the excitation and decay rates of M, and they have maximum values at slightly different E_{offset_H} values. A similar behavior is apparent for the overall ET rates $k_{LMe}k_{MRe}/(k_{LMe}+k_{MRe})$ and the dependences of P_{max} and η_{in} on E_{offset_L} .

As the recombination rate increases (Figures 27c through 27e), similar plot shapes are obtained, and the origins of the trends are the same as for the case of slow recombination

rates (Figures 27a and 27b). However, the maxima of P_{max} and η_{in} occur at smaller E_{offset_H} and larger E_{offset_L} values compared to the case when the recombination rate is small, as mentioned above. For the dependences of P_{max} and η_{in} on the M QD E_{offset_H} value, the ET and HT processes determine P_{max} and η_{in} if the charge recombination rate is very small. The two HT rates, k_{RMh} and k_{MLh} , must be similar to prevent a blockade in the hole transfer through the triad. If the charge recombination rate is large, however, it is more important to reduce the charge recombination to obtain large P_{max} and η_{in} values. For example, k_{MLh} is one order of magnitude larger than k_{RMh} when E_{offset_H} is 0.01 eV, so the hole moves rapidly through the HOMO of M compared to the charge recombination time. The inference that $k_{MLh} > k_{RMh}$ produces larger P_{max} and η_{in} values than when $k_{MLh} < k_{RMh}$ is confirmed by the unsymmetrical plots of P_{max} and η_{in} vs. E_{offset_H} in Figure 27. That is, the left portions of the plots correspond to the $k_{MLh} > k_{RMh}$ regime and the right portions correspond to the $k_{MLh} < k_{RMh}$ regime. That is, P_{max} and η_{in} are more sensitive to the M QD E_{offset_H} when $k_{MLh} < k_{RMh}$ than when $k_{MLh} > k_{RMh}$. For the dependences of P_{max} and η_{in} on the M QD E_{offset_L} value, a similar analysis finds that the P_{max} and η_{in} values reach their maxima as a function of the M QD E_{offset_L} for similar reasons.

Figures 26c and 26d show that the QD triad improves the external and internal power conversion quantum efficiencies, especially when the charge recombination rates are comparable to the ET and HT rates. If we adjust the M HOMO and LUMO energies simultaneously, additional improvements in P_{max} and η_{in} can be realized (Figures 27c and 27d). For charge recombination rates of 10^9 s^{-1} , maximum values of P_{max} (0.39 pW) and η_{in} ($\sim 58\%$) occur when E_{offset_H} and E_{offset_L} of M are set to 0.36 eV and 0.13 eV,

respectively. These parameters give an I_{SC} value of 0.33 pA, representing a $\sim 400\%$ improvement over the dyad architecture, and a U_{OC} value of 1.59 V, representing a $\sim 12\%$ improvement over the dyad architecture. When the charge recombination rate is 10^5 s^{-1} , the largest P_{max} (0.52 pW) and η_{in} ($\sim 72\%$) values occur at electronic state energies with E_{offset_H} of 0.46 eV and E_{offset_L} of 0.03 eV for M. In the high charge recombination rate limit, I_{SC} , U_{OC} , P_{max} , and η_{in} are not significantly changed by M and are insensitive to its band edge energies.

The results of optimizing P_{max} by tuning the M QD band-edge energies are summarized in Table 7. The case of a dyad is compared with the case of two triad systems; Triad 1 has the M QD band-edge midway between that of the L and R QDs and Triad 2 has band-edge energy offsets tuned to optimize P_{max} . The advantages in performance of the triad over the dyad architecture becomes more significant as the recombination rate grows. When the recombination rate becomes larger than the ET and HT rates, however, the E_{offset_H} (E_{offset_L}) values for M that produce the maxima of P_{max} and η_{in} are outside of the energy range bounded by the HOMO (LUMO) energy offsets of the L and R dots (Figures 27e and 27f), breaking the type II alignment in Figure 22a. Table 7 shows that the upper bound of U_{OC} is not limited by the energy difference between the LUMO of the R QD and the HOMO of the L QD; U_{OC} cannot be larger than the largest band gap of the QDs in the dyad/triad system.

Table 7: Performance of QD dyad and triad systems I . The I_{sc} , U_{oc} , P_{max} , and η_{in} values for the QD dyad and triad systems (5.5 nm CdTe and 4.5 nm CdSe, $m\hbar^* = 0.1$ a.u.) are calculated with two charge recombination rates, 10^9 s^{-1} and 10^5 s^{-1} .

	$k_{RLc} = k_{MLc} = k_{RMc} = 10^9 \text{ s}^{-1}$			$k_{RLc} = k_{MLc} = k_{RMc} = 10^5 \text{ s}^{-1}$		
	Dyad	Triad 1	Triad 2	Dyad	Triad 1	Triad 2
P_{max} (pW)	0.064	0.37	0.38	0.45	0.45	0.52
η_{in} (%)	8.5	56	55	67	75	67
I_{sc} (pA)	0.066	0.32	0.33	0.37	0.37	0.45
U_{oc} (V)	1.42	1.60	1.59	1.67	1.83	1.60

Table 7 shows that η_{in} , I_{sc} , and U_{oc} depend on the energetics of the M QD, but the values are not at their maximum values for the HOMO and LUMO energies for Triad 2. We are interested in the open-circuit voltage U_{oc} as a function of the M QD E_{offset_H} and E_{offset_L} . The U_{oc} values can be scanned in the same way as P_{max} (described above), and it reaches a maximum when $E_{offset_H} = 0.06 \text{ eV}$ and $E_{offset_L} = 0.28 \text{ eV}$ if the charge recombination rate is close to the ET and HT rates (10^9 s^{-1}). Figure 28a is plotted for $E_{offset_L} = 0.28 \text{ eV}$, and Figure 28b is plotted for $E_{offset_H} = 0.06 \text{ eV}$. Although a maximum U_{oc} value is reached, U_{oc} is nearly independent of the M QD E_{offset_H} value and U_{oc} only changes from 1.66 V to 1.67 V as the E_{offset_H} varies from 0.81 eV to 0.01 eV. U_{oc} is sensitive, however, to the M QD E_{offset_L} value and U_{oc} changes from 1.32 V to 1.68 V as E_{offset_L} changes from -0.17 eV to 0.43 eV . The LUMO gap between the L and R QDs is 0.26 eV in this case, which is much smaller than the HOMO gap between the L and R QDs 0.51 eV. Therefore, the electron populations in the three LUMOs is more evenly distributed

than the hole population is among the three HOMOs at steady-state. The electron energy is more sensitive to the M QD LUMO energy than the hole energy is to the M QD HOMO energy.

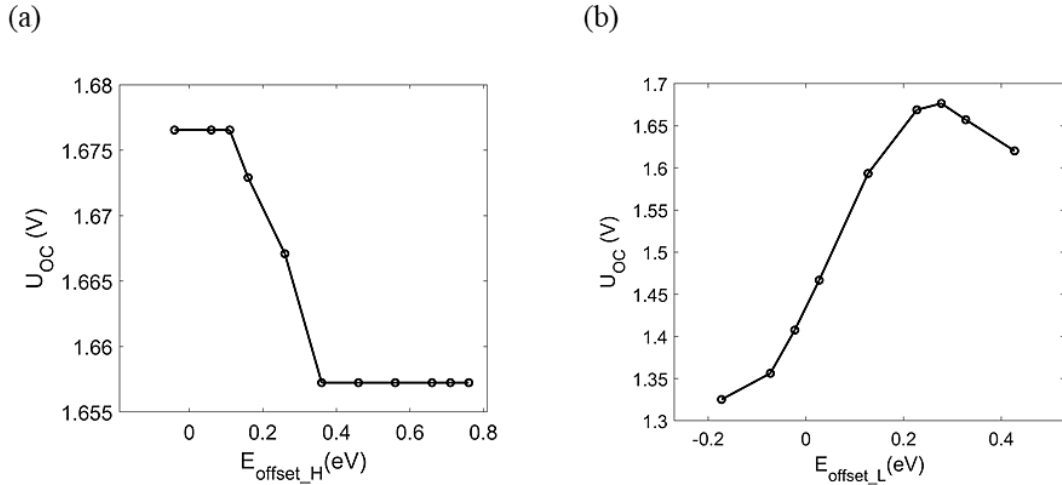


Figure 28: Mediate QD-dependent open-circuit voltage in QD triad systems . Open-circuit voltage as a function of (a) HOMO band edge offset E_{offset_H} and (b) LUMO band edge offset E_{offset_L} of the M QD. The charge recombination rates are set to 10^9 s^{-1} , which is the same order as the ET and HT rates.

4.3.4 Effects of QD absorber number on triad performance

In the above analysis, we assumed that all three QDs could be photoexcited. We also explore the case where only one QD (L, M, or R) may absorb light in the QD triad. This can be viewed as analogous to heterojunctions involving non-absorbing electron and hole transport layers, as are typically used in devices. Our simulations find that the I_{SC} , U_{OC} , P_{max} , and η_{in} values for the triad are larger than those of the dyad when the charge recombination rate is large ($> 10^8 \text{ s}^{-1}$). These values can be further improved by varying the M QD band edge offsets (Figures 27 and 28). These results agree with the three-QD-

absorber model and confirm our analysis on the M band energy dependences of P_{max} and η_{in} .

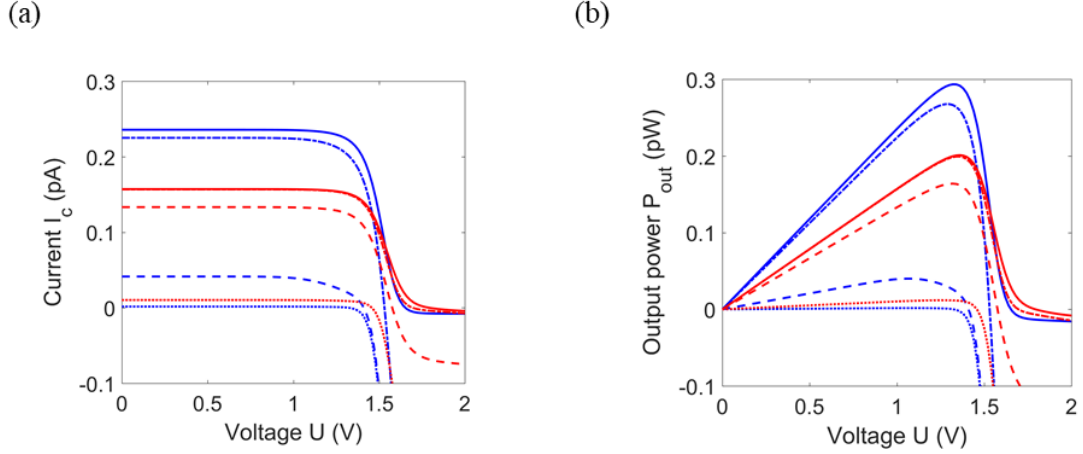


Figure 29: I-U and P-U curves with L QD as light absorber. I-U (a) and P-U (b) characteristic curves for QD dyad (blue) and triad (red) systems for different charge recombination rates, 10^5 s^{-1} (solid), 10^7 s^{-1} (dash-dot), 10^9 s^{-1} (dashed) and 10^{11} s^{-1} (dotted). Only the L QD is photo excited and effective hole mass is 0.1 a.u.

In the one-QD-absorber system, the computed output power and current are not normalized by the number of QDs. The $I-U$ and $P-U$ curves and the I_{SC} , U_{OC} , FF , P_{max} and η_{in} values are similar to the case found with the three QD absorber system. (Figures 29 and 30) This observation indicates that our conclusions are not limited by the number of photo-absorbing QDs. A noteworthy difference in the I_{SC} is that, for the one-QD-absorber model, I_{SC} is larger than the normalized I_{SC} value for the three-QD-absorber model. This arises because the three QDs have different excitation and decay rates. A large difference in P_{max} and η_{in} vs. band-edge energies in the one-QD-absorber case for the triad occurs when we compare the effects of varying the middle QD energetics. If only L can be excited, the P_{max} and η_{in} vs. E_{offset_L} curves are very similar to Figures 27b and 27d, but the plots of P_{max} and η_{in} vs. E_{offset_H} are different in the limit of low HOMO energy for M. The P_{max} and η_{in} vs.

E_{offset_H} plots plateau as E_{offset_H} decreases (Figure 31). If only L is photoexcited, the most important processes are hole transfer from the L HOMO to the left electrode, the ET chain ($L \rightarrow M \rightarrow R \rightarrow Y$), and charge recombination from the M LUMO to the L HOMO. The transport processes are not affected by the M HOMO energy, as long as its value is lower in energy than the L HOMO. The charge recombination from the R LUMO to the M HOMO and the HT from the M HOMO to the L HOMO are also important for determining P_{max} and η_{in} . The HT rate (k_{MLh}) increases more slowly as E_{offset_H} decreases, because the L density of states has a square root dependence on energy (eq 4.4). Similarly, if only R is photoexcited, the P_{max} and η_{in} vs. E_{offset_H} plots have shapes analogous to the plots in Figures 27a and 27c, but the P_{max} and η_{in} vs. E_{offset_L} plots will plateau as E_{offset_L} grows. In the case where only the M QD is photoexcited, P_{max} and η_{in} vs. E_{offset_L} and P_{max} and η_{in} vs. E_{offset_H} plots should resemble the three-QD-absorber model, based on the above analysis.

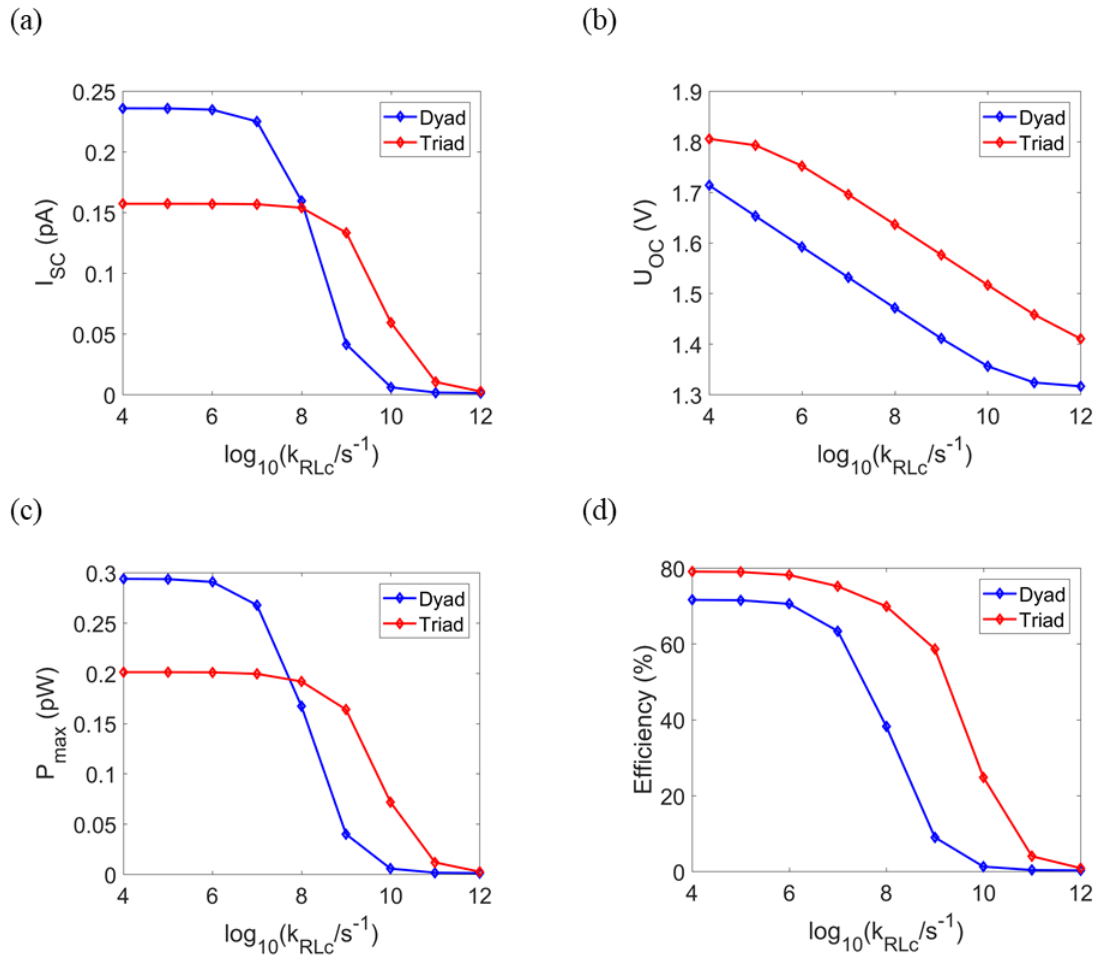


Figure 30: Solar cell performance for QD triad with L QD as light absorber . (a) open-circuit voltage, (b) short-circuit current, (c) maximum output power, and (d) fill factor for the QD dyad (blue) and triad (red) solar cell systems as a function of the charge recombination rate, k_{RLC} . Only the L QD can be photoexcited.

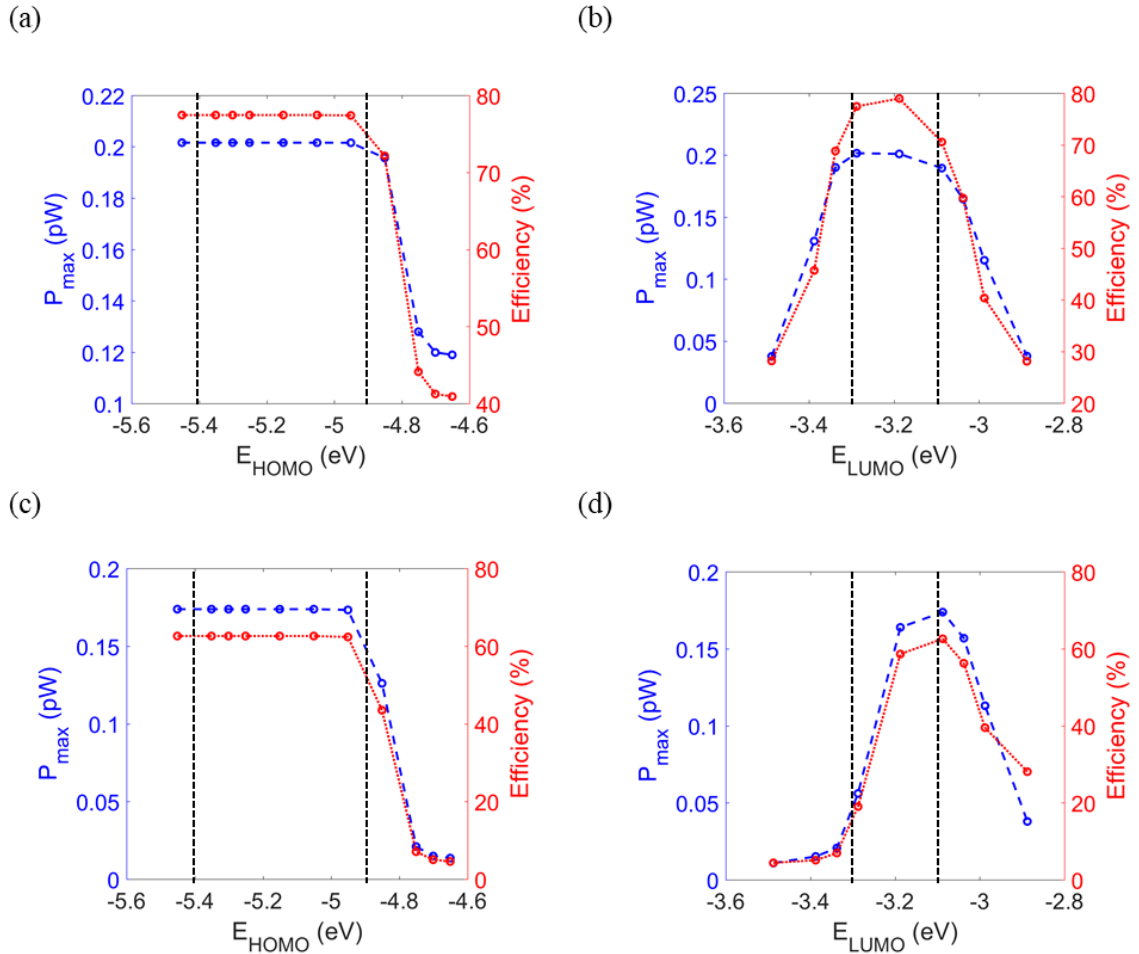


Figure 31: Mediate QD energetics influences on PCE for QD triad with L QD as light absorber . Maximum output power (blue and dashed, left vertical axis) and internal quantum efficiency (red and dotted, right vertical axis) as a function of the HOMO (a, c and e) and LUMO (b, d and f) energies of the middle QD. For (a) and (b), k_{RLC} is 10^5 s^{-1} ; for (c) and (d), k_{RLC} is 10^9 s^{-1} . The HOMO (LUMO) energies of the L and R QDs are taken as -4.89 eV (-3.07 eV) and -5.41 eV (-3.33 eV), respectively. The HOMO and LUMO positions of the L and R QDs are indicated by the vertical lines in the figures. Only the L QD can be photoexcited.

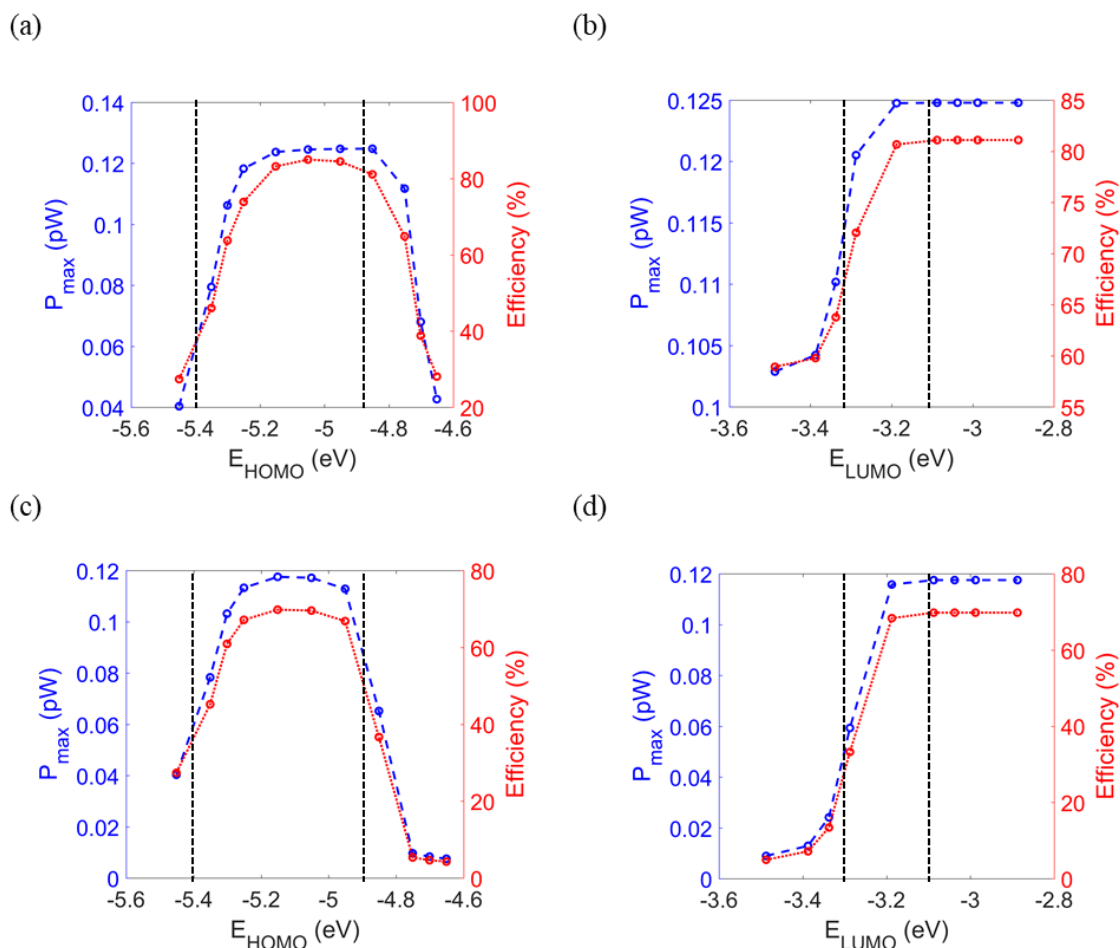


Figure 32: Mediate QD energetics influences on PCE for QD triad with R QD as absorber . Maximum output power (blue and dashed, left vertical axis) and internal quantum efficiency (red and dotted, right vertical axis) as a function of the HOMO (a, c and e) and LUMO (b, d and f) energies of the middle QD. For (a) and (b), k_{RLc} is 10^5 s^{-1} ; for (c) and (d), k_{RLc} is 10^9 s^{-1} . The HOMO (LUMO) energies of the L and R QDs are taken as -4.89 eV (-3.07 eV) and -5.41 eV (-3.33 eV), respectively. The HOMO and LUMO positions of the L and R QDs are indicated by the vertical lines in the figures. Only the R QD can be photoexcited.

4.3.5 Effects of quantum dot size on triad performance

The HT and ET rate constants depend on the QD sizes, since the QD band edge, DOS, and reorganization energies are all functions of the QD radii. The experimentally measured band edges of CdTe and CdSe QD are fitted as exponential functions of the QD diameters.³³ In the above analysis, we presented the solar cell performance for a 5.5 nm CdTe QD ($E_{HOMO} = -4.89$ eV, $E_{LUMO} = -3.07$ eV) and 4.5 nm CdSe QD ($E_{HOMO} = -5.40$ eV, $E_{LUMO} = -3.33$ eV) dyad (pair I, L QD size > R QD size). We also compared the results for different donor and acceptor QD sizes of 4.5 nm CdTe ($E_{HOMO} = -4.93$ eV, $E_{LUMO} = -3.00$ eV) and 5.5 nm CdSe ($E_{HOMO} = -5.38$ eV, $E_{LUMO} = -3.38$ eV) (pair II, L QD size < R QD size). The largest difference between pair I and pair II is that the LUMO-LUMO band offset of pair II is much larger than that of pair I. The I_{SC} , U_{OC} , P_{max} and η_{in} values for pair II are shown in Table 8. Varying the M QD band edge offsets improve the maximum value of P_{max} for the pair II-based triad system, but this value is smaller than the values of the pair I based triad system when the charge recombination rate is small ($\sim 10^5$ s⁻¹). Comparing the increase of the maximum value from dyad to triad, we found that the improvement is larger in the pair II-based system than in the pair I based system.

Maximum P_{max} values are obtained by varying the band edge offset of M QD in pair II-based triad. The I_{SC} , U_{OC} and η_{in} values of pair II are calculated when P_{max} maximizes. They are shown in Table 8. When the recombination rate is 10^5 s⁻¹, use of a triad affects I_{SC} , P_{max} , and η_{in} very little, but it increases U_{OC} from 1.65 V to 1.94 V (18%); when the recombination rate is 10^9 s⁻¹, the triad enhances I_{SC} , P_{max} , and η_{in} considerably

and the U_{OC} increases from 1.41 V to 1.65 V (17%). When the charge recombination rate is very large (compared to charge transfer rates), the energy difference between the R QD LUMO and the L QD HOMO becomes more important and limits U_{OC} . When the charge recombination rate is very small (10^5 s^{-1} , about 100 times smaller than the charge transfer rates), U_{OC} is determined mainly by the ET and HT rates and their differences, which could make the U_{OC} larger than the energy difference between the R QD LUMO and the L QD HOMO.

Table 8: Performance of QD dyad and triad systems II. The I_{SC} , U_{OC} , P_{max} and η_{in} values for the QD dyad and triad systems (4.5 nm CdTe and 5.5 nm CdSe, $m_h^* = 0.1$ a.u.) are calculated with two charge recombination rates, 10^9 s^{-1} and 10^5 s^{-1} .

	$k_{RLc} = k_{MLc} = k_{RMc} = 10^9 \text{ s}^{-1}$		$k_{RLc} = k_{MLc} = k_{RMc} = 10^5 \text{ s}^{-1}$	
	Dyad	Triad	Dyad	Triad
P_{max} (pW)	0.059	0.38	0.42	0.43
η_{in} (%)	8.2	58	66	71
I_{SC} (pA)	0.062	0.32	0.35	0.35
U_{OC} (V)	1.41	1.65	1.65	1.94

4.3.6 Effects of hole effective hole mass on triad performance

We used the light hole effective mass $m_h^* = 0.1$ a.u. in the above modeling. The hole effective mass depends on the QD structure, position on the Brillouin zone, and surface structure.¹²⁷ The heavy hole m_h^* is about 1 a.u. for CdTe and CdSe (Table 9). This parameter affects the HT rates between the QD HOMOs, and the HT rates are rescaled by a constant $10^{3/2}$ when we change the hole effective mass. In this case, the three-QD-

absorber model and the band-edge energies of M in the third column of Table 9 were used to compute the I_{SC} , U_{OC} , P_{max} , and η_{in} values.

Table 9: Performance of QD dyad and triad systems III . The I_{SC} , U_{OC} , P_{max} and η_{in} values for the QD dyad and triad systems (5.5 nm CdTe and 4.5 nm CdSe, $m_h^* = 1$ a.u.) are calculated with two charge recombination rates, 10^9 s^{-1} and 10^5 s^{-1} .

	$k_{RLc} = k_{MLc} = k_{RMc} = 10^9 \text{ s}^{-1}$		$k_{RLc} = k_{MLc} = k_{RMc} = 10^5 \text{ s}^{-1}$	
	Dyad	Triad 2	Dyad	Triad 2
P_{max} (pW)	0.064	0.37	0.45	0.45
η_{in} (%)	8.5	56	67	75
I_{SC} (pA)	0.066	0.32	0.37	0.37
V_{OC} (V)	1.42	1.60	1.67	1.83

When the charge recombination rates are 10^5 s^{-1} , the I_{SC} and U_{OC} values are nearly unchanged (Table 8), but the P_{max} and η_{in} values are slightly smaller than in the systems with light holes. The larger discrepancy between the HT and ET rates, compared to the cases where we use the light hole effective mass, produces higher trapped charge carrier concentration, more charge recombination, and exciton decay events become more important, leading to lower P_{max} and η_{in} values. When the charge recombination rates are 10^9 s^{-1} , I_{SC} , U_{OC} , P_{max} , and η_{in} are larger than in systems with the light hole. If charge recombination between QDs is significant, increasing the ET/HT rates will have the same effect as decreasing the relative charge-recombination rates. Because the heavy hole mass is ten times larger than the light hole mass, the performance of the QD solar cell models

for both heavy and light holes will behave more like the models with only heavy holes, but the general analysis above for light holes remains valid.

4.3.7 Implications for PbS QD solar cells.

A large recent improvement in QD-based solar cell performance was achieved by using a PbS QD dyad system as the photoactive material. However, these PbS QD solar cells suffer from a small open-circuit voltage that is believed to arise from charge recombination between donor and acceptor QDs.^{87,190,210,211,229} The discussion above on U_{OC} shows that its value is sensitive to charge recombination rates and can be influenced by using a third QD, creating a triad system. In either the pair I or pair II systems, the maximum U_{OC} change found was ~ 0.4 V, consistent with the open-circuit voltage deficit values found in PbS QD solar cell systems. In a PbS-EDT (1,2-ethanedithiol) /PbS-TBAI (tetrabutylammonium iodide) photovoltaic device design, eliminating the sub-bandgap states should provide a larger performance improvement than other methods that optimize interfacial charge transfer to reduce the U_{OC} deficit.²¹¹ A cascade band edge energy architecture, derived from using different ligands, was shown to lead to high U_{OC} and FF values, which improved the device efficiency.⁸⁷ In a PbS/ZnO colloidal QD heterojunction solar cell, a mixed ligand treatment to passivate surface traps was shown to reduce the U_{OC} deficit from ~ 0.7 V to ~ 0.5 V.²¹⁰ Solution-based passivation in the PbS-EDT/PbS-MAI QD solar cell produces a 12.5% I_{SC} improvement and gives a record 10.6% cell efficiency.¹⁹⁰ These findings are consistent with the analysis performed above, which examines the influence of charge recombination rates and solar cell architecture on the

photovoltaic performance. In particular, we find that the inclusion of a middle QD can decrease the U_{oc} deficit (Figure 28b) by as much as 0.3 V.

4.4 Summary and conclusions

We used a master equation approach with steady-state analysis to model the current-voltage, power-voltage, and related photovoltaic performance properties of QD dyad and triad systems. The triad systems show predicted improvements in U_{oc} , I_{sc} , P_{max} , and η_{in} compared to the corresponding dyad systems when the charge recombination rates are large. However, when the charge recombination rates are small, the middle QD can reduce I_{sc} and slightly decrease P_{max} . The performance improvements of the triad over the dyad can be as large as 17% in U_{oc} , 400% in I_{sc} , 540% in P_{max} , and 600% in η_{in} (see Table 8 in 9) when the charge-recombination rates are comparable to the charge-transfer rates. A small improvement in preventing charge recombination (if its rate is comparable to the charge transfer rate) can greatly enhance I_{sc} , P_{max} , and η_{in} values while U_{oc} is only mildly affected. The performance of the triad system is less sensitive to charge recombination rates than is the performance of the dyad system. The increased performance of the triad system over the dyad is attributed to inhibition of the direct charge recombination between the QDs near the two electrodes.

Tuning the HOMO and LUMO energies of the middle QD in the triad perturbs P_{max} and η_{in} , and strategies to tune these energies depend on whether the charge recombination rates are large or small compared to the ET and HT rates. In our cascade energy alignment case, the M QD HOMO should be tuned to enhance the hole transfer processes when the charge recombination rates are negligible and should be tuned to reduce the charge

recombination from the R QD LUMO to the M QD HOMO when the charge recombination rates are significant. The M QD LUMO should be tuned to slow the back ET from R to L when the charge recombination rates are slow and should be tuned to inhibit the charge recombination between the M and L QDs when the charge recombination rates are large. Correctly positioning the M QD LUMO is the most important parameter for overall cell performance (as demonstrated by a greater than five-fold improvement in internal and external quantum efficiencies) in the regime where competing charge recombination degrades the device performance.

5. Conclusion

In this dissertation, we described several tight-binding models to study the electronic properties of CdTe and CdSe QDs, the donor-acceptor electronic couplings and the charge transfer rates of CdTe-CdSe QD dyads and used the computed charge transfer rates to analyze the solar cell properties of QD dyad and triad based solar cells. The theoretical findings suggest novel design strategies to control the charge transfer rates between QDs and thus to improve the QD solar cell power conversion efficiencies. In addition, our findings of the QD size-dependent electron transfer mechanisms between QDs also shed light on methods to select charge transfer channels in various charge transfer systems.

In chapter 2, we used a tight-binding model originally built in our work to calculate the electronic structure of the CdTe-CdSe dyad linked by a dithiol bridge molecule and to study the QD size-dependent charge transfer rates in the dyads. It is found that both the electron and hole transfer rates decrease as the donor QD radius increases, but may decrease, show a peak or increase as the acceptor QD radius increases, depending on the QD size dependences of the acceptor density of states, electronic couplings between two QDs and the reaction activation energy. The dependences of charge transfer rates on the acceptor QD radius reproduce the consequences of the reaction free energy inverted effects on the dependences of charge transfer rates on the reaction free energy. Balanced electron and hole transfer rates are obtained when the CdTe

and CdSe radius ratio is ~ 1.3 . We also showed that the charge transfer dominating mechanism depends on the product of the CdTe and CdSe radii. For large (small) radii products, the through space (bridge) charge transfer mechanism dominates.

In chapter 3, we further studied into the through space/solvent and through-bridge charge transfer mechanisms in QD dyad systems, focusing on the bridge charge influence on the QD-QD electronic couplings. We found that the positively (negatively) charged group in the molecule bridge stabilizes (destabilizes) the frontier orbital energies of the bridge and solvent molecules and the band edge energies of the QDs, compared to the neutral bridges. The bridge charge also changes the localization of the bridge orbitals and the through-solvent pathway contributions from the high and low energy pathways to the total through-solvent donor-acceptor couplings. These bridge charge effects on the electron tunneling barrier and pathway result in that replacing the neutral group in the bridge with the positively charged group increases the donor-acceptor coupling, but replacing the neutral group with the negatively charged group can either increase, decrease or have little effect on the donor-acceptor couplings, depending on the electronic responses of the QDs, solvent and bridge molecules. We also shown that the through-solvent and through-bridge mechanism dominance switch by varying the QD sizes can be significantly tuned by the bridge charge.

Finally, in chapter 4, we focused on the performance of QD solar cells based on QD dyads and triads, using the QD size-dependent charge transfer properties obtained in

the previous chapters. We found that the short-circuit current, open-circuit voltage, maximum output power (representing the external power conversion efficiency) and internal power conversion efficiency decrease as the charge recombination rates between two nearest-neighbor QDs increase. The QD triad based solar cells have better performance than the QD dyad based solar cells, especially when the charge recombination rates are comparable to the charge transfer rates. We also shown that the mediate QD band edge energy offsets can be tuned to further improve the performance of the QD triad system.

We did not consider the explicit surface capping ligands on the QDs in this dissertation, but the capping ligand effects on the CdSe QD electronic structures can be found in the last paper listed in the biography section. In this dissertation, we mainly focused on QD size-dependent properties, because the QD size-induced quantum confinement effects are what most QD applications base on.

Appendix A

$$\begin{aligned} \frac{d [L^+R^*]}{d t} = & -(k_{Rd} + k_{RLe} + k_{L\Lambda h} + k_{RLc} + k_{RYe}) [L^+R^*] \\ & + k_{Rex}[L^+R] + k_{LRe}[L^*R^+] + k_{\Lambda Lh}[LR^*] + k_{YRe}[L^+R^+] \end{aligned} \quad (A 1)$$

$$\begin{aligned} \frac{d [L^+R^-]}{d t} = & -(k_{RLe} + k_{L\Lambda h} + k_{RLc} + k_{RYe}) [L^+R^-] \\ & + k_{LRe}[L^*R] + k_{\Lambda Lh}[LR^-] + k_{YRe}[L^+R] \end{aligned} \quad (A 2)$$

$$\begin{aligned} \frac{d [L^+R]}{d t} = & -(k_{Rex} + k_{LRh} + k_{L\Lambda h} + k_{YRe}) [L^+R] \\ & + k_{Rd}[L^+R^*] + k_{RLh}[LR^+] + k_{\Lambda Lh}[LR] + k_{RYe}[L^+R^-] \end{aligned} \quad (A 3)$$

$$\frac{d [L^+R^+]}{d t} = -(k_{L\Lambda h} + k_{YRe}) [L^+R^+] + k_{\Lambda Lh}[LR^+] + k_{RYe}[L^+R^*] \quad (A 4)$$

$$\begin{aligned} \frac{d [L^-R^*]}{d t} = & -(k_{Rd} + k_{\Lambda Lh} + k_{RYe}) [L^-R^*] + k_{Rex}[L^-R] + k_{L\Lambda h}[L^*R^*] + k_{YRe}[L^-R^+] \\ & \end{aligned} \quad (A 5)$$

$$\frac{d [L^-R^-]}{d t} = -(k_{\Lambda Lh} + k_{RYe}) [L^-R^-] + k_{L\Lambda h}[L^*R^-] + k_{YRe}[L^-R] \quad (A 6)$$

$$\begin{aligned} \frac{d [L^-R]}{d t} = & -(k_{Rex} + k_{LRe} + k_{\Lambda Lh} + k_{YRe}) [L^-R] \\ & + k_{Rd}[L^-R^*] + k_{RLe}[LR^-] + k_{L\Lambda h}[L^*R^*] + k_{YRe}[L^-R^-] \end{aligned} \quad (A 7)$$

$$\begin{aligned} \frac{d [L^-R^+]}{d t} = & -(k_{LRe} + k_{\Lambda Lh} + k_{RLh} + k_{YRe}) [L^-R^+] + k_{RLe}[LR^*] + k_{LRh}[L^*R] + \\ & k_{L\Lambda h}[L^*R^+] + k_{RYe}[L^-R^*] + k_{RLc}[L^*R^*] \end{aligned} \quad (A 8)$$

$$\begin{aligned} \frac{d [L^*R^*]}{d t} = & -(k_{Rd} + k_{Ld} + k_{L\Lambda h} + k_{RLc} + k_{RYe}) [L^*R^*] \\ & + k_{Rex}[L^*R] + k_{Lex}[LR^*] + k_{\Lambda Lh}[L^-R^*] + k_{YRe}[L^*R^+] \end{aligned} \quad (A 9)$$

$$\begin{aligned} \frac{d [L^*R^-]}{d t} = & -(k_{Ld} + k_{LRh} + k_{L\Lambda h} + k_{RLc} + k_{RYe}) [L^*R^-] \\ & + k_{Lex} [LR^-] + k_{RLh} [L^-R^*] + k_{\Lambda Lh} [L^-R^-] + k_{YRe} [L^*R] \end{aligned} \quad (A 10)$$

$$\begin{aligned} \frac{d [L^*R]}{d t} = & -(k_{Ld} + k_{Rex} + k_{L\Lambda h} + k_{LRe} + k_{LRh} + k_{YRe}) [L^*R] \\ & + k_{Lex} [LR] + k_{Rd} [L^*R^*] + k_{RLe} [L^+R^-] + k_{RLh} [L^-R^+] + k_{\Lambda Lh} [L^-R] + \\ & k_{RYe} [L^*R^-] \end{aligned} \quad (A 11)$$

$$\begin{aligned} \frac{d [L^*R^+]}{d t} = & -(k_{Ld} + k_{LRe} + k_{L\Lambda h} + k_{YRe}) [L^*R^+] \\ & + k_{Lex} [LR^+] + k_{RLe} [L^+R^*] + k_{\Lambda Lh} [L^-R^+] + k_{RYe} [L^*R^*] \end{aligned} \quad (A 12)$$

$$\begin{aligned} \frac{d [LR^*]}{d t} = & -(k_{Lex} + k_{Rd} + k_{RLh} + k_{\Lambda Lh} + k_{RLe} + k_{RYe}) [LR^*] \\ & + k_{Ld} [L^*R^*] + k_{Rex} [LR] + k_{LRh} [L^*R] + k_{L\Lambda h} [L^+R^*] + k_{LRe} [L^-R^+] + k_{YRe} [LR^+] \end{aligned} \quad (A 13)$$

$$\begin{aligned} \frac{d [LR^+]}{d t} = & -(k_{Lex} + k_{\Lambda Lh} + k_{YRe}) [LR^+] \\ & + k_{Ld} [L^*R^+] + k_{L\Lambda h} [L^+R^+] + k_{RYe} [LR^*] + k_{RLc} [L^+R^*] \end{aligned} \quad (A 14)$$

$$\begin{aligned} \frac{d [LR^-]}{d t} = & -(k_{\Lambda Lh} + k_{RLe} + k_{RYe} + k_{Lex}) [LR^-] \\ & + k_{LRe} [L^-R] + k_{Ld} [L^*R^-] + k_{L\Lambda h} [L^+R^-] + k_{YRe} [LR] \end{aligned} \quad (A 15)$$

$$\begin{aligned} \frac{d [LR]}{d t} = & -(k_{Rex} + k_{Lex} + k_{\Lambda Lh} + k_{YRe}) [LR] \\ & + k_{Ld} [L^*R] + k_{Rd} [LR^*] + k_{L\Lambda h} [L^+R] + k_{RYe} [LR^-] + k_{RLc} [L^+R^-] \end{aligned} \quad (A 16)$$

References

- (1) Chan, W. C.; Nie, S. Quantum Dot Bioconjugates for Ultrasensitive Nonisotopic Detection. *Science* **1998**, *281*, 2016–2018.
- (2) Chan, W. C. W.; Maxwell, D. J.; Gao, X.; Bailey, R. E.; Han, M.; Nie, S. Luminescent Quantum Dots for Multiplexed Biological Detection and Imaging. *Curr. Opin. Biotechnol.* **2002**, *13*, 40–46.
- (3) Yue, Z.; Lisdat, F.; Parak, W. J.; Hickey, S. G.; Tu, L.; Sabir, N.; Dorfs, D.; Bigall, N. C. Quantum-Dot-Based Photoelectrochemical Sensors for Chemical and Biological Detection. *ACS Appl. Mater. Interfaces* **2013**, *5*, 2800–2814.
- (4) Medintz, I. L.; Uyeda, H. T.; Goldman, E. R.; Mattoussi, H. Quantum Dot Bioconjugates for Imaging, Labelling and Sensing. *Nat. Mater.* **2005**, *4*, 435–446.
- (5) Michler, P.; Kiraz, A.; Becher, C.; Schoenfeld, W. V.; Petroff, P. M.; Zhang, L.; Hu, E.; Imamoglu, A. A Quantum Dot Single-Photon Turnstile Device. *Science* **2000**, *290*, 2282–2285.
- (6) Imamog, A.; Yamamoto, Y.; Others. Turnstile Device for Heralded Single Photons: Coulomb Blockade of Electron and Hole Tunneling in Quantum Confined P-I-N Heterojunctions. *Phys. Rev. Lett.* **1994**, *72*, 210.
- (7) Han, M.; Gao, X.; Su, J. Z.; Nie, S. Quantum-Dot-Tagged Microbeads for Multiplexed Optical Coding of Biomolecules. *Nat. Biotechnol.* **2001**, *19*, 631–635.
- (8) Ho, Y.-P.; Kung, M. C.; Yang, S.; Wang, T.-H. Multiplexed Hybridization Detection with Multicolor Colocalization of Quantum Dot Nanoprobes. *Nano Lett.* **2005**, *5*, 1693–1697.
- (9) Lagerholm, B. C.; Wang, M.; Ernst, L. A.; Ly, D. H.; Liu, H.; Bruchez, M. P.; Waggoner, A. S. Multicolor Coding of Cells with Cationic Peptide Coated Quantum Dots. *Nano Lett.* **2004**, *4*, 2019–2022.
- (10) Kagan, C. R.; Murray, C. B. Charge Transport in Strongly Coupled Quantum Dot Solids. *Nat. Nanotechnol.* **2015**, *10*, 1013–1026.
- (11) Harman, T. C.; Taylor, P. J.; Walsh, M. P.; LaForge, B. E. Quantum Dot Superlattice Thermoelectric Materials and Devices. *Science* **2002**, *297*, 2229–2232.

- (12) Liu, Y.; Sahoo, P.; Makongo, J. P. A.; Zhou, X.; Kim, S.-J.; Chi, H.; Uher, C.; Pan, X.; Poudeu, P. F. P. Large Enhancements of Thermopower and Carrier Mobility in Quantum Dot Engineered Bulk Semiconductors. *J. Am. Chem. Soc.* **2013**, *135*, 7486–7495.
- (13) Ghatak, K. P.; Bhattacharya, S. Thermoelectric Power in Quantum Dot Superlattices Under Large Magnetic Field. In *Thermoelectric Power in Nanostructured Materials*; Springer Series in Materials Science; Springer, Berlin, Heidelberg, 2010; pp. 145–171.
- (14) Nejat, P.; Jomehzadeh, F.; Taheri, M. M.; Gohari, M.; Abd. Majid, M. Z. A Global Review of Energy Consumption, CO₂ Emissions and Policy in the Residential Sector (with an Overview of the Top Ten CO₂ Emitting Countries). *Renewable Sustainable Energy Rev.* **2015**, *43*, 843–862.
- (15) Charlier, D.; Risch, A. Evaluation of the Impact of Environmental Public Policy Measures on Energy Consumption and Greenhouse Gas Emissions in the French Residential Sector. *Energy Policy* **2012**, *46*, 170–184.
- (16) Bilgen, S. Structure and Environmental Impact of Global Energy Consumption. *Renewable Sustainable Energy Rev.* **2014**, *38*, 890–902.
- (17) Kamat, P. V. Quantum Dot Solar Cells. Semiconductor Nanocrystals as Light Harvesters. *J. Phys. Chem. C* **2008**, *112*, 18737–18753.
- (18) Kamat, P. V.; Tvrđy, K.; Baker, D. R.; Radich, J. G. Beyond Photovoltaics: Semiconductor Nanoarchitectures for Liquid-Junction Solar Cells. *Chem. Rev.* **2010**, *110*, 6664–6688.
- (19) Cells, Q. D. S. Harvesting Light Energy with CdSe Nanocrystals Molecularly Linked to Mesoscopic TiO₂ Films Robel, Istvan; Subramanian, Vaidyanathan; Kuno, Masaru; Kamat, Prashant V. *J. Am. Chem. Soc.* **2006**, *128*, 2385–2393.
- (20) Jun, H. K.; Careem, M. A.; Arof, A. K. Quantum Dot-Sensitized Solar Cells—perspective and Recent Developments: A Review of Cd Chalcogenide Quantum Dots as Sensitizers. *Renewable Sustainable Energy Rev.* **2013**, *22*, 148–167.
- (21) Lee, Y.-L.; Lo, Y.-S. Highly Efficient Quantum-Dot-Sensitized Solar Cell Based on Co-Sensitization of CdS/CdSe. *Adv. Funct. Mater.* **2009**, *19*, 604–609.
- (22) Huynh, W. U.; Dittmer, J. J.; Alivisatos, A. P. Hybrid Nanorod-Polymer Solar Cells. *Science* **2002**, *295*, 2425–2427.

- (23) Robel, I.; Subramanian, V.; Kuno, M.; Kamat, P. V. Quantum Dot Solar Cells. Harvesting Light Energy with CdSe Nanocrystals Molecularly Linked to Mesoscopic TiO₂ Films. *J. Am. Chem. Soc.* **2006**, *128*, 2385–2393.
- (24) Tryk, D. A.; Fujishima, A.; Honda, K. Recent Topics in Photoelectrochemistry: Achievements and Future Prospects. *Electrochim. Acta* **2000**, *45*, 2363–2376.
- (25) Hamada, M.; Takenokoshi, N.; Matozaki, K.; Feng, Q.; Murase, N.; Wakida, S.-I.; Nakanishi, S.; Biju, V. In Situ Photochemical Surface Passivation of CdSe/ZnS Quantum Dots for Quantitative Light Emission and Enhanced Photocurrent Response in Solar Cells. *J. Phys. Chem. C* **2014**, *118*, 2178–2186.
- (26) Hodes, G. A Thin-Film Polycrystalline Photoelectrochemical Cell with 8% Solar Conversion Efficiency. *Nature* **1980**, *285*, 29.
- (27) Dalpian, G. M.; Chelikowsky, J. R. Self-Purification in Semiconductor Nanocrystals. *Phys. Rev. Lett.* **2006**, *96*, 226802.
- (28) Hyeon-Deuk, K.; Kim, J.; Prezhdov, O. V. Ab Initio Analysis of Auger-Assisted Electron Transfer. *J. Phys. Chem. Lett.* **2015**, *6*, 244–249.
- (29) Lian, S.; Weinberg, D. J.; Harris, R. D.; Kodaimati, M. S.; Weiss, E. A. Subpicosecond Photoinduced Hole Transfer from a CdS Quantum Dot to a Molecular Acceptor Bound Through an Exciton-Delocalizing Ligand. *ACS Nano* **2016**, *10*, 6372–6382.
- (30) Balberg, I. Electrical Transport Mechanisms in Three Dimensional Ensembles of Silicon Quantum Dots. *J. Appl. Phys.* **2011**, *110*, 061301.
- (31) Talgorn, E.; Gao, Y.; Aerts, M.; Kunneman, L. T.; Schins, J. M.; Savenije, T. J.; van Huis, M. A.; van der Zant, H. S. J.; Houtepen, A. J.; Siebbeles, L. D. A. Unity Quantum Yield of Photogenerated Charges and Band-like Transport in Quantum-Dot Solids. *Nat. Nanotechnol.* **2011**, *6*, 733–739.
- (32) Choi, H.; Santra, P. K.; Kamat, P. V. Synchronized Energy and Electron Transfer Processes in Covalently Linked CdSe-Squaraine Dye-TiO₂ Light Harvesting Assembly. *ACS Nano* **2012**, *6*, 5718–5726.
- (33) Jasieniak, J.; Califano, M.; Watkins, S. E. Size-Dependent Valence and Conduction Band-Edge Energies of Semiconductor Nanocrystals. *ACS Nano* **2011**, *5*, 5888–5902.
- (34) Bester, G.; Wu, X.; Vanderbilt, D.; Zunger, A. Importance of Second-Order Piezoelectric Effects in Zinc-Blende Semiconductors. *Phys. Rev. Lett.* **2006**, *96*,

187602.

- (35) Widmann, F.; Simon, J.; Daudin, B.; Feuillet, G.; Rouvière, J. L.; Pelekanos, N. T.; Fishman, G. Blue-Light Emission from GaN Self-Assembled Quantum Dots due to Giant Piezoelectric Effect. *Phys. Rev. B Condens. Matter* **1998**, *58*, R15989–R15992.
- (36) Yaacobi-Gross, N.; Garphunkin, N.; Solomeshch, O.; Vaneski, A.; Susha, A. S.; Rogach, A. L.; Tessler, N. Combining Ligand-Induced Quantum-Confined Stark Effect with Type II Heterojunction Bilayer Structure in CdTe and CdSe Nanocrystal-Based Solar Cells. *ACS Nano* **2012**, *6*, 3128–3133.
- (37) Graff, B. M.; Bloom, B. P.; Wierzbinski, E.; Waldeck, D. H. Electron Transfer in Nanoparticle Dyads Assembled on a Colloidal Template. *J. Am. Chem. Soc.* **2016**.
- (38) Wang, Y.; Wang, L.; Waldeck, D. H. Electrochemically Guided Photovoltaic Devices: A Photocurrent Study of the Charge Transfer Directionality between CdTe and CdSe Nanoparticles. *J. Phys. Chem. C* **2011**, *115*, 18136–18141.
- (39) Semonin, O. E.; Luther, J. M.; Choi, S.; Chen, H.-Y.; Gao, J.; Nozik, A. J.; Beard, M. C. Peak External Photocurrent Quantum Efficiency Exceeding 100% via MEG in a Quantum Dot Solar Cell. *Science* **2011**, *334*, 1530–1533.
- (40) Exceeding, P. E. P. Q. E. 100% via MEG in a Quantum Dot Solar Cell Semonin. *Octavi E* 1530–1533.
- (41) Mathew, S.; Yella, A.; Gao, P.; Humphry-Baker, R.; Curchod, B. F. E.; Ashari-Astani, N.; Tavernelli, I.; Rothlisberger, U.; Nazeeruddin, M. K.; Grätzel, M. Dye-Sensitized Solar Cells with 13% Efficiency Achieved through the Molecular Engineering of Porphyrin Sensitizers. *Nat. Chem.* **2014**, *6*, 242–247.
- (42) Yang, W. S.; Park, B. W.; Jung, E. H.; Jeon, N. J.; Kim, Y. C. Iodide Management in Formamidinium-Lead-Halide-based Perovskite Layers for Efficient Solar Cells. **2017**.
- (43) Wang, R.; Wu, X.; Xu, K.; Zhou, W.; Shang, Y.; Tang, H.; Chen, H.; Ning, Z. Highly Efficient Inverted Structural Quantum Dot Solar Cells. *Adv. Mater.* **2018**, *30*.
- (44) Lan, X.; Voznyy, O.; Kiani, A.; García de Arquer, F. P.; Abbas, A. S.; Kim, G.-H.; Liu, M.; Yang, Z.; Walters, G.; Xu, J.; *et al.* Passivation Using Molecular Halides Increases Quantum Dot Solar Cell Performance. *Adv. Mater.* **2016**, *28*, 299–304.
- (45) Du, J.; Du, Z.; Hu, J.-S.; Pan, Z.; Shen, Q.; Sun, J.; Long, D.; Dong, H.; Sun, L.;

- Zhong, X.; *et al.* Zn–Cu–In–Se Quantum Dot Solar Cells with a Certified Power Conversion Efficiency of 11.6%. *J. Am. Chem. Soc.* **2016**, *138*, 4201–4209.
- (46) Zhao, K.; Pan, Z.; Mora-Seró, I.; Cánovas, E.; Wang, H.; Song, Y.; Gong, X.; Wang, J.; Bonn, M.; Bisquert, J.; *et al.* Boosting Power Conversion Efficiencies of Quantum-Dot-Sensitized Solar Cells beyond 8% by Recombination Control. *J. Am. Chem. Soc.* **2015**, *137*, 5602–5609.
- (47) Lokteva, I.; Radychev, N.; Witt, F.; Borchert, H.; Parisi, J.; Kolny-Olesiak, J. Surface Treatment of CdSe Nanoparticles for Application in Hybrid Solar Cells: The Effect of Multiple Ligand Exchange with Pyridine. *J. Phys. Chem. C* **2010**, *114*, 12784–12791.
- (48) Zhao, K.; Pan, Z.; Zhong, X. Charge Recombination Control for High Efficiency Quantum Dot Sensitized Solar Cells. *J. Phys. Chem. Lett.* **2016**, *7*, 406–417.
- (49) Mora-Sero, I.; Gimenez, S.; Fabregat-Santiago, F.; Gomez, R.; Shen, Q.; Toyoda, T.; Bisquert, J. Recombination in Quantum Dot Sensitized Solar Cells. *Acc. Chem. Res.* **2009**, *42*, 1848–1857.
- (50) Roelofs, K. E.; Herron, S. M.; Bent, S. F. Increased Quantum Dot Loading by pH Control Reduces Interfacial Recombination in Quantum-Dot-Sensitized Solar Cells. *ACS Nano* **2015**, *9*, 8321–8334.
- (51) Kronik, L.; Ashkenasy, N.; Leibovitch, M.; Fefer, E.; Shapira, Y.; Gorer, S.; Hodes, G. Surface States and Photovoltaic Effects in CdSe Quantum Dot Films. *J. Electrochem. Soc.* **1998**, *145*, 1748–1755.
- (52) Cao, Y.; Stavrinadis, A.; Lasanta, T.; So, D.; Konstantatos, G. The Role of Surface Passivation for Efficient and Photostable PbS Quantum Dot Solar Cells. *Nature Energy* **2016**, *1*, 16035.
- (53) Brown, P. R.; Kim, D.; Lunt, R. R.; Zhao, N.; Bawendi, M. G.; Grossman, J. C.; Bulović, V. Energy Level Modification in Lead Sulfide Quantum Dot Thin Films through Ligand Exchange. *ACS Nano* **2014**, *8*, 5863–5872.
- (54) Bloom, B. P.; Zhao, L.-B.; Wang, Y.; Waldeck, D. H.; Liu, R.; Zhang, P.; Beratan, D. N. Ligand-Induced Changes in the Characteristic Size-Dependent Electronic Energies of CdSe Nanocrystals. *J. Phys. Chem. C* **2013**, *117*, 22401–22411.
- (55) Ibáñez, M.; Zamani, R.; Gorse, S.; Fan, J.; Ortega, S.; Cadavid, D.; Morante, J. R.; Arbiol, J.; Cabot, A. Core–Shell Nanoparticles As Building Blocks for the Bottom-Up Production of Functional Nanocomposites: PbTe–PbS Thermoelectric

- Properties. *ACS Nano* **2013**, *7*, 2573–2586.
- (56) Rawalekar, S.; Kaniyankandy, S.; Verma, S.; Ghosh, H. N. Surface-State-Mediated Charge-Transfer Dynamics in CdTe/CdSe Core-Shell Quantum Dots. *Chemphyschem* **2011**, *12*, 1729–1735.
- (57) Zhu, H.; Song, N.; Lian, T. Controlling Charge Separation and Recombination Rates in CdSe/ZnS Type I Core-Shell Quantum Dots by Shell Thicknesses. *J. Am. Chem. Soc.* **2010**, *132*, 15038–15045.
- (58) Sarkar, S.; Saha, S.; Pal, S.; Sarkar, P. Electronic Structure of Thiol-Capped CdTe Quantum Dots and CdTeQD–Carbon Nanotube Nanocomposites. *J. Phys. Chem. C* **2012**, *116*, 21601–21608.
- (59) Osada, N.; Oshima, T.; Kuwahara, S.; Toyoda, T.; Shen, Q.; Katayama, K. Photoexcited Carrier Dynamics of Double-Layered CdS/CdSe Quantum Dot Sensitized Solar Cells Measured by Heterodyne Transient Grating and Transient Absorption Methods. *Phys. Chem. Chem. Phys.* **2014**, *16*, 5774–5778.
- (60) Vogl, P.; Hjalmarsen, H. P.; Dow, J. D. A Semi-Empirical Tight-Binding Theory of the Electronic Structure of Semiconductors†. *J. Phys. Chem. Solids* **1983**, *44*, 365–378.
- (61) Akinci, Ö.; Gürel, H. H.; Ünlü, H. Semi-Empirical Tight Binding Modelling of CdS/CdTe, ZnSSe/ZnSe and ZnSSe/CdSe Heterostructures. *Thin Solid Films* **2009**, *517*, 2431–2437.
- (62) Frenzel, J.; Joswig, J.-O.; Sarkar, P.; Seifert, G.; Springborg, M. The Effects of Organisation, Embedding and Surfactants on the Properties of Cadmium Chalcogenide (CdS, CdSe and CdS/CdSe) Semiconductor Nanoparticles. *Eur. J. Inorg. Chem.* **2005**, *2005*, 3585–3596.
- (63) Sarkar, S.; Rajbanshi, B.; Sarkar, P. Understanding the Electronic Structure of CdSe Quantum Dot-Fullerene (C60) Hybrid Nanostructure for Photovoltaic Applications. *J. Appl. Phys.* **2014**, *116*, 114303.
- (64) Michos, F. I.; Sigalas, M. M.; Koukaras, E. N. Computational Study of the Excitation Energies of CdSe Nanoparticles with Defects. *IEEE J. Sel. Top. Quantum Electron.* **2017**, *23*, 1–5.
- (65) Kuznetsov, A. E.; Balamurugan, D.; Skourtis, S. S.; Beratan, D. N. Structural and Electronic Properties of Bare and Capped CdnSen/CdnTen Nanoparticles (n = 6, 9). *J. Phys. Chem. C* **2012**, *116*, 6817–6830.

- (66) Azpiroz, J. M.; Infante, I.; De Angelis, F. First-Principles Modeling of Core/Shell Quantum Dot Sensitized Solar Cells. *J. Phys. Chem. C* **2015**, *119*, 12739–12748.
- (67) Chuang, C.-H.; Lo, S. S.; Scholes, G. D.; Burda, C. Charge Separation and Recombination in CdTe/CdSe Core/Shell Nanocrystals as a Function of Shell Coverage: Probing the Onset of the Quasi Type-II Regime. *J. Phys. Chem. Lett.* **2010**, *1*, 2530–2535.
- (68) Tvrđy, K.; Frantsuzov, P. A.; Kamat, P. V. Photoinduced Electron Transfer from Semiconductor Quantum Dots to Metal Oxide Nanoparticles. *Proc. Natl. Acad. Sci. U. S. A.* **2011**, *108*, 29–34.
- (69) Borrelli, N. F.; Hall, D. W.; Holland, H. J.; Smith, D. W. Quantum Confinement Effects of Semiconducting Microcrystallites in Glass. *J. Appl. Phys.* **1987**, *61*, 5399–5409.
- (70) Takagahara, T.; Takeda, K. Theory of the Quantum Confinement Effect on Excitons in Quantum Dots of Indirect-Gap Materials. *Phys. Rev. B Condens. Matter* **1992**, *46*, 15578–15581.
- (71) Lu, Z. H.; Lockwood, D. J.; Baribeau, J.-M. Quantum Confinement and Light Emission in SiO₂/Si Superlattices. **1995**, *378*, 258–260.
- (72) Lee, J. R. I.; Meulenbergh, R. W.; Hanif, K. M.; Mattoussi, H.; Klepeis, J. E.; Terminello, L. J.; van Buuren, T. Experimental Observation of Quantum Confinement in the Conduction Band of CdSe Quantum Dots. *Phys. Rev. Lett.* **2007**, *98*, 146803.
- (73) Yun, H. J.; Paik, T.; Edley, M. E.; Baxter, J. B.; Murray, C. B. Enhanced Charge Transfer Kinetics of CdSe Quantum Dot-Sensitized Solar Cell by Inorganic Ligand Exchange Treatments. *ACS Appl. Mater. Interfaces* **2014**, *6*, 3721–3728.
- (74) Yaacobi-Gross, N.; Garphunkin, N.; Solomeshch, O.; Vaneski, A.; Susha, A. S.; Rogach, A. L.; Tessler, N. Combining Ligand-Induced Quantum-Confined Stark Effect with Type II Heterojunction Bilayer Structure in CdTe and CdSe Nanocrystal-Based Solar Cells. *ACS Nano* **2012**, *6*, 3128–3133.
- (75) Klimov, V. I.; Mikhailovsky, A. A.; Xu, S.; Malko, A.; Hollingsworth, J. A.; Leatherdale, C. A.; Eisler, H.; Bawendi, M. G. Optical Gain and Stimulated Emission in Nanocrystal Quantum Dots. *Science* **2000**, *290*, 314–317.
- (76) Hyun, B.-R.; Zhong, Y.-W.; Bartnik, A. C.; Sun, L.; Abruña, H. D.; Wise, F. W.;

- Goodreau, J. D.; Matthews, J. R.; Leslie, T. M.; Borrelli, N. F. Electron Injection from Colloidal PbS Quantum Dots into Titanium Dioxide Nanoparticles. *ACS Nano* **2008**, *2*, 2206–2212.
- (77) Nagaoka, H.; Colbert, A. E.; Strein, E.; Janke, E. M.; Salvador, M.; Schlenker, C. W.; Ginger, D. S. Size-Dependent Charge Transfer Yields in Conjugated Polymer/Quantum Dot Blends. *J. Phys. Chem. C* **2014**, *118*, 5710–5715.
- (78) Anikeeva, P. O.; Halpert, J. E.; Bawendi, M. G.; Bulović, V. Electroluminescence from a Mixed Red–Green–Blue Colloidal Quantum Dot Monolayer. *Nano Lett.* **2007**, *7*, 2196–2200.
- (79) Chaban, V. V.; Prezhdo, V. V.; Prezhdo, O. V. Covalent Linking Greatly Enhances Photoinduced Electron Transfer in Fullerene-Quantum Dot Nanocomposites: Time-Domain Ab Initio Study. *J. Phys. Chem. Lett.* **2013**, *4*, 1–6.
- (80) Schütz, R.; Malhotra, S.; Thomas, I.; Strothkämper, C.; Bartelt, A.; Schwarzburg, K.; Hannappel, T.; Fasting, C.; Eichberger, R. Dynamics of a Covalently Conjoined FRET Dye Ensemble for Electron Injection into ZnO Nanorods. *J. Phys. Chem. C* **2014**, *118*, 9336–9345.
- (81) Chenu, A.; Scholes, G. D. Coherence in Energy Transfer and Photosynthesis. *Annu. Rev. Phys. Chem.* **2015**, *66*, 69–96.
- (82) Kamat, P. V. Quantum Dot Solar Cells. Semiconductor Nanocrystals as Light Harvester†. *J. Phys. Chem. C* **2008**, *112*, 18737–18753.
- (83) Tan, F.; Qu, S.; Zhang, W.; Wang, Z. Hybrid Morphology Dependence of CdTe:CdSe Bulk-Heterojunction Solar Cells. *Nanoscale Res. Lett.* **2014**, *9*, 593.
- (84) Lan, X.; Masala, S.; Sargent, E. H. Charge-Extraction Strategies for Colloidal Quantum Dot Photovoltaics. *Nat. Mater.* **2014**, *13*, 233–240.
- (85) Einax, M.; Dierl, M.; Schiff, P. R.; Nitzan, A. Multiple State Representation Scheme for Organic Bulk Heterojunction Solar Cells: A Novel Analysis Perspective. *arXiv [cond-mat.mtrl-sci]*, 2013.
- (86) Tan, F.; Qu, S.; Yu, P.; Li, F.; Chen, C.; Zhang, W.; Wang, Z. Hybrid Bulk-Heterojunction Solar Cells Based on All Inorganic Nanoparticles. *Sol. Energy Mater. Sol. Cells* **2014**, *120*, Part A, 231–237.
- (87) Chuang, C.-H. M.; Brown, P. R.; Bulović, V.; Bawendi, M. G. Improved Performance

- and Stability in Quantum Dot Solar Cells through Band Alignment Engineering. *Nat. Mater.* **2014**, *13*, 796–801.
- (88) Wu, M.; Mukherjee, P.; Lamont, D. N.; Waldeck, D. H. Electron Transfer and Fluorescence Quenching of Nanoparticle Assemblies. *J. Phys. Chem. C* **2010**, *114*, 5751–5759.
- (89) Xin, X.; Li, B.; Jung, J.; Yoon, Y. J.; Biswas, R.; Lin, Z. Ab Initio Simulation of Charge Transfer at the Semiconductor Quantum Dot/TiO₂ Interface in Quantum Dot-Sensitized Solar Cells. *Part. Part. Syst. Charact.* **2015**, *32*, 80–90.
- (90) Kim, G.-H.; García de Arquer, F. P.; Yoon, Y. J.; Lan, X.; Liu, M.; Voznyy, O.; Yang, Z.; Fan, F.; Ip, A. H.; Kanjanaboos, P.; *et al.* High-Efficiency Colloidal Quantum Dot Photovoltaics via Robust Self-Assembled Monolayers. *Nano Lett.* **2015**, *15*, 7691–7696.
- (91) Wang, Y.; Xie, Z.; Gotesman, G.; Wang, L.; Bloom, B. P.; Markus, T. Z.; Oron, D.; Naaman, R.; Waldeck, D. H. Determination of the Electronic Energetics of CdTe Nanoparticle Assemblies on Au Electrodes by Photoemission, Electrochemical, and Photocurrent Studies. *J. Phys. Chem. C* **2012**, *116*, 17464–17472.
- (92) Jin, S.; Tagliazucchi, M.; Son, H.-J.; Harris, R. D.; Aruda, K. O.; Weinberg, D. J.; Nepomnyashchii, A. B.; Farha, O. K.; Hupp, J. T.; Weiss, E. A. Enhancement of the Yield of Photoinduced Charge Separation in Zinc Porphyrin–Quantum Dot Complexes by a Bis(dithiocarbamate) Linkage. *J. Phys. Chem. C* **2015**, *119*, 5195–5202.
- (93) Jin, S.; Harris, R. D.; Lau, B.; Aruda, K. O.; Amin, V. A.; Weiss, E. A. Enhanced Rate of Radiative Decay in CdSe Quantum Dots upon Adsorption of an Exciton-Delocalizing Ligand. *Nano Lett.* **2014**, *14*, 5323–5328.
- (94) Shalom, M.; Buhbut, S.; Tirosh, S.; Zaban, A. Design Rules for High-Efficiency Quantum-Dot-Sensitized Solar Cells: A Multilayer Approach. *J. Phys. Chem. Lett.* **2012**, *3*, 2436–2441.
- (95) Zhao, N.; Osedach, T. P.; Chang, L.-Y.; Geyer, S. M.; Wanger, D.; Binda, M. T.; Arango, A. C.; Bawendi, M. G.; Bulovic, V. Colloidal PbS Quantum Dot Solar Cells with High Fill Factor. *ACS Nano* **2010**, *4*, 3743–3752.
- (96) Guldi, D. M.; Luo, C.; Prato, M.; Dietel, E.; Hirsch, A. Charge-Transfer in a π -Stacked Fullerene Porphyrin Dyad: Evidence for Back Electron Transfer in the “Marcus-Inverted” region. *Chem. Commun.* **2000**, 373–374.

- (97) Robel, I.; Kuno, M.; Kamat, P. V. Size-Dependent Electron Injection from Excited CdSe Quantum Dots into TiO₂ Nanoparticles. *J. Am. Chem. Soc.* **2007**, *129*, 4136–4137.
- (98) Chu, I.-H.; Radulaski, M.; Vukmirovic, N.; Cheng, H.-P.; Wang, L.-W. Charge Transport in a Quantum Dot Supercrystal. *J. Phys. Chem. C* **2011**, *115*, 21409–21415.
- (99) Lippens, P. E.; Lannoo, M. Comparison between Calculated and Experimental Values of the Lowest Excited Electronic State of Small CdSe Crystallites. *Phys. Rev. B Condens. Matter* **1990**, *41*, 6079–6081.
- (100) Baskoutas, S.; Terzis, A. F. Size-Dependent Band Gap of Colloidal Quantum Dots. *J. Appl. Phys.* **2006**, *99*, 013708.
- (101) Pokrant, S.; Whaley, K. B. Tight-Binding Studies of Surface Effects on Electronic Structure of CdSe Nanocrystals: The Role of Organic Ligands, Surface Reconstruction, and Inorganic Capping Shells. *Eur. Phys. J. D* **1999**, *6*, 255–267.
- (102) Lee, S.; Jönsson, L.; Wilkins, J. W.; Bryant, G. W.; Klimeck, G. Electron-Hole Correlations in Semiconductor Quantum Dots with Tight-Binding Wave Functions. *Phys. Rev. B Condens. Matter* **2001**, *63*, 195318.
- (103) Logar, M.; Xu, S.; Acharya, S.; Prinz, F. B. Variation of Energy Density of States in Quantum Dot Arrays due to Interparticle Electronic Coupling. *Nano Lett.* **2015**, *15*, 1855–1860.
- (104) Singhal, P.; Ghosh, H. N. Ultrafast Hole/Electron Transfer Dynamics in a CdSe Quantum Dot Sensitized by Pyrogallol Red: A Super-Sensitization System. *J. Phys. Chem. C* **2014**, *118*, 16358–16365.
- (105) Kaniyankandy, S.; Rawalekar, S.; Ghosh, H. N. Ultrafast Charge Transfer Dynamics in Photoexcited CdTe Quantum Dot Decorated on Graphene. *J. Phys. Chem. C* **2012**, *116*, 16271–16275.
- (106) Tafen, D. N.; Prezhdo, O. V. Size and Temperature Dependence of Electron Transfer between CdSe Quantum Dots and a TiO₂ Nanobelt. *J. Phys. Chem. C* **2015**, *119*, 5639–5647.
- (107) Debnath, T.; Maity, P.; Banerjee, T.; Das, A.; Ghosh, H. N. Ultrafast Electron Injection, Hole Transfer, and Charge Recombination Dynamics in CdSe QD Super-Sensitized Re(I)-Polypyridyl Complexes with Catechol and Resorcinol Moiety: Effect of Coupling. *J. Phys. Chem. C* **2015**, *119*, 3522–3529.

- (108) Marcus, R. A. Chemical and Electrochemical Electron-Transfer Theory. *Annu. Rev. Phys. Chem.* **1964**, *15*, 155–196.
- (109) Ratner, M. A. Non-Adiabatic Electron Transfer: Some Dynamical and Electronic Extensions of Standard Rate Expressions. In *Perspectives in Photosynthesis; The Jerusalem Symposia on Quantum Chemistry and Biochemistry*; Springer: Dordrecht, Netherlands, 1990; Vol. 22, pp. 185–210.
- (110) Gao, Y. Q.; Georgievskii, Y.; Marcus, R. A. On the Theory of Electron Transfer Reactions at Semiconductor Electrode/liquid Interfaces. *J. Chem. Phys.* **2000**, *112*, 3358–3369.
- (111) Marcus, R. A. Free Energy of Nonequilibrium Polarization Systems. II. Homogeneous and Electrode Systems. *J. Chem. Phys.* **1963**, *38*, 1858–1862.
- (112) Zhu, H.; Yang, Y.; Hyeon-Deuk, K.; Califano, M.; Song, N.; Wang, Y.; Zhang, W.; Prezhdo, O. V.; Lian, T. Auger-Assisted Electron Transfer from Photoexcited Semiconductor Quantum Dots. *Nano Lett.* **2014**, *14*, 1263–1269.
- (113) Tarafder, K.; Surendranath, Y.; Olshansky, J. H.; Alivisatos, A. P.; Wang, L.-W. Hole Transfer Dynamics from a CdSe/CdS Quantum Rod to a Tethered Ferrocene Derivative. *J. Am. Chem. Soc.* **2014**, *136*, 5121–5131.
- (114) Yamamoto, H.; Waldeck, D. H. Effect of Tilt-Angle on Electron Tunneling through Organic Monolayer Films. *J. Phys. Chem. B* **2002**.
- (115) Napper, A. M.; Liu, H.; Waldeck, D. H. The Nature of Electronic Coupling between Ferrocene and Gold through Alkanethiolate Monolayers on Electrodes: The Importance of Chain Composition, Interchain Coupling, and Quantum Interference. *J. Phys. Chem. B* **2001**, *105*, 7699–7707.
- (116) Wierzbinski, E.; Yin, X.; Werling, K.; Waldeck, D. H. The Effect of Oxygen Heteroatoms on the Single Molecule Conductance of Saturated Chains. *J. Phys. Chem. B* **2013**, *117*, 4431–4441.
- (117) Cave, R. J.; Newton, M. D. Calculation of Electronic Coupling Matrix Elements for Ground and Excited State Electron Transfer Reactions: Comparison of the Generalized Mulliken–Hush and Block *J. Chem. Phys.* **1997**.
- (118) Renger, T.; Marcus, R. A. Variable-Range Hopping Electron Transfer through Disordered Bridge States: Application to DNA. *J. Phys. Chem. A* **2003**, *107*, 8404–8419.

- (119) Zhang, Y.; Young, R. M.; Thazhathveetil, A. K.; Singh, A. P. N.; Liu, C.; Berlin, Y. A.; Grozema, F. C.; Lewis, F. D.; Ratner, M. A.; Renaud, N.; *et al.* Conformationally Gated Charge Transfer in DNA Three-Way Junctions. *J. Phys. Chem. Lett.* **2015**, *6*, 2434–2438.
- (120) Koole, R.; Luigjes, B.; Tachiya, M.; Pool, R.; Vlugt, T. J. H.; de Mello Donegá, C.; Meijerink, A.; Vanmaekelbergh, D. Differences in Cross-Link Chemistry between Rigid and Flexible Dithiol Molecules Revealed by Optical Studies of CdTe Quantum Dots. *J. Phys. Chem. C* **2007**, *111*, 11208–11215.
- (121) Wang, H.; McNellis, E. R.; Kinge, S.; Bonn, M.; Cánovas, E. Tuning Electron Transfer Rates through Molecular Bridges in Quantum Dot Sensitized Oxides. *Nano Lett.* **2013**, *13*, 5311–5315.
- (122) Skourtis, S. S.; Beratan, D. N.; Onuchic, J. N. The Two-State Reduction for Electron and Hole Transfer in Bridge-Mediated Electron-Transfer Reactions. *Chem. Phys.* **1993**, *176*, 501–520.
- (123) Skourtis, S. S.; Beratan, D. N. Theories of Structure–Function Relationships for Bridge-Mediated Electron Transfer Reactions. In *Advances in Chemical Physics*; John Wiley & Sons, Inc., 2007; pp. 377–452.
- (124) Scholes, G. D.; Jones, M.; Kumar, S. Energetics of Photoinduced Electron-Transfer Reactions Decided by Quantum Confinement. *J. Phys. Chem. C* **2007**, *111*, 13777–13785.
- (125) Marcus, R. A. Tutorial on Rate Constants and Reorganization Energies. *J. Electroanal. Chem.* **2000**, *483*, 2–6.
- (126) Kuznetsov, A. E.; Beratan, D. N. Structural and Electronic Properties of Bare and Capped Cd₃₃Se₃₃ and Cd₃₃Te₃₃ Quantum Dots. *J. Phys. Chem. C* **2014**, *118*, 7094–7109.
- (127) Rubio-Ponce, A.; Olguín, D.; Hernandez-Calderon, I. Calculation of the Effective Masses of II-VI Semiconductor Compounds. *Superficies y vacío* **2003**, *16*, 26–28.
- (128) Curtiss*, L. A.; Miller*, J. R. Distance Dependence of Electronic Coupling through Trans Alkyl Chains: Effects of Electron Correlation. *J. Phys. Chem. A* **1998**, *102*, 160–167.
- (129) Korkusinski, M.; Voznyy, O.; Hawrylak, P. Fine Structure and Size Dependence of Exciton and Biexciton Optical Spectra in CdSe Nanocrystals. *Phys. Rev. B*

Condens. Matter **2010**, *82*, 245304.

- (130) Sarkar, S.; Pal, S.; Sarkar, P. Electronic Structure and Band Gap Engineering of CdTe Semiconductor Nanowires. *J. Mater. Chem.* **2012**, *22*, 10716–10724.
- (131) Tvrđy, K.; Kamat, P. V. Substrate Driven Photochemistry of CdSe Quantum Dot Films: Charge Injection and Irreversible Transformations on Oxide Surfaces. *J. Phys. Chem. A* **2009**, *113*, 3765–3772.
- (132) Buhks, E.; Jortner, J. Activationless Electron Transfer Processes in Biological Systems. *FEBS Lett.* **1980**, *109*, 117–120.
- (133) Rips, I.; Jortner, J. Outer Sphere Electron Transfer in Polar Solvents. Activationless and Inverted Regimes. *J. Chem. Phys.* **1987**, *87*, 6513–6519.
- (134) Yu, Q.; Wang, Y.; Yi, Z.; Zu, N.; Zhang, J.; Zhang, M.; Wang, P. High-Efficiency Dye-Sensitized Solar Cells: The Influence of Lithium Ions on Exciton Dissociation, Charge Recombination, and Surface States. *ACS Nano* **2010**, *4*, 6032–6038.
- (135) Ip, A. H.; Thon, S. M.; Hoogland, S.; Voznyy, O.; Zhitomirsky, D.; Debnath, R.; Levina, L.; Rollny, L. R.; Carey, G. H.; Fischer, A.; *et al.* Hybrid Passivated Colloidal Quantum Dot Solids. *Nat. Nanotechnol.* **2012**, *7*, 577–582.
- (136) Fengler, S.; Zillner, E.; Dittrich, T. Density of Surface States at CdSe Quantum Dots by Fitting of Temperature-Dependent Surface Photovoltage Transients with Random Walk Simulations. *J. Phys. Chem. C* **2013**, *117*, 6462–6468.
- (137) Gross, D.; Mora-Seró, I.; Dittrich, T.; Belaidi, A.; Mauser, C.; Houtepen, A. J.; Da Como, E.; Rogach, A. L.; Feldmann, J. Charge Separation in Type II Tunneling Multilayered Structures of CdTe and CdSe Nanocrystals Directly Proven by Surface Photovoltage Spectroscopy. *J. Am. Chem. Soc.* **2010**, *132*, 5981–5983.
- (138) Zhang, X.; Li, W.; Yao, J.; Zhan, C. High-Efficiency Nonfullerene Polymer Solar Cell Enabling by Integration of Film-Morphology Optimization, Donor Selection, and Interfacial Engineering. *ACS Appl. Mater. Interfaces* **2016**, *8*, 15415–15421.
- (139) Lee, C.-T.; Lee, C.-H. Conversion Efficiency Improvement Mechanisms of Polymer Solar Cells by Balance Electron–hole Mobility Using Blended P3HT:PCBM:pentacene Active Layer. *Org. Electron.* **2013/8**, *14*, 2046–2050.
- (140) Jun, H. K.; Careem, M. A.; Arof, A. K. Quantum Dot-Sensitized Solar Cells—perspective and Recent Developments: A Review of Cd Chalcogenide Quantum

- Dots as Sensitizers. *Renewable Sustainable Energy Rev.* **2013**, *22*, 148–167.
- (141) Pattantyus-Abraham, A. G.; Kramer, I. J.; Barkhouse, A. R.; Wang, X.; Konstantatos, G.; Debnath, R.; Levina, L.; Raabe, I.; Nazeeruddin, M. K.; Grätzel, M.; *et al.* *ACS Nano* **4**, 3374 (2010). *CrossRef Google Scholar* **2011**.
- (142) Jun, S.; Lee, J.; Jang, E. Highly Luminescent and Photostable Quantum Dot–Silica Monolith and Its Application to Light-Emitting Diodes. *ACS Nano* **2013**, *7*, 1472–1477.
- (143) Bera, D.; Qian, L.; Tseng, T.-K.; Holloway, P. H. Quantum Dots and Their Multimodal Applications: A Review. *Materials* **2010**, *3*, 2260–2345.
- (144) Coe, S.; Woo, W.-K.; Bawendi, M.; Bulović, V. Electroluminescence from Single Monolayers of Nanocrystals in Molecular Organic Devices. *Nature* **2002**, *420*, 800–803.
- (145) Chang, J.; Huang, X.; Zhou, G.; Cui, S.; Hallac, P. B. Multilayered Si Nanoparticle/Reduced Graphene Oxide Hybrid as a High-Performance Lithium-Ion Battery Anode. *Advanced* **2014**.
- (146) Liu, R.; Huang, H.; Li, H.; Liu, Y.; Zhong, J.; Li, Y.; Zhang, S.; Kang, Z. Metal Nanoparticle/Carbon Quantum Dot Composite as a Photocatalyst for High-Efficiency Cyclohexane Oxidation. *ACS Catal.* **2014**, *4*, 328–336.
- (147) Amirav, L.; Alivisatos, A. P. Luminescence Studies of Individual Quantum Dot Photocatalysts. *J. Am. Chem. Soc.* **2013**, *135*, 13049–13053.
- (148) Nabiev, I.; Mitchell, S.; Davies, A.; Williams, Y.; Kelleher, D.; Moore, R.; Gun'ko, Y. K.; Byrne, S.; Rakovich, Y. P.; Donegan, J. F.; *et al.* Nonfunctionalized Nanocrystals Can Exploit a Cell's Active Transport Machinery Delivering Them to Specific Nuclear and Cytoplasmic Compartments. *Nano Lett.* **2007**, *7*, 3452–3461.
- (149) Wang, Y.; Hu, R.; Lin, G.; Roy, I.; Yong, K.-T. Functionalized Quantum Dots for Biosensing and Bioimaging and Concerns on Toxicity. *ACS Appl. Mater. Interfaces* **2013**, *5*, 2786–2799.
- (150) Sukhanova, A.; Devy, J.; Venteo, L.; Kaplan, H.; Artemyev, M.; Oleinikov, V.; Klinov, D.; Pluot, M.; Cohen, J. H. M.; Nabiev, I. Biocompatible Fluorescent Nanocrystals for Immunolabeling of Membrane Proteins and Cells. *Anal. Biochem.* **2004**, *324*, 60–67.

- (151) Oh, S. J.; Wang, Z.; Berry, N. E.; Choi, J.-H.; Zhao, T.; Gauding, E. A.; Paik, T.; Lai, Y.; Murray, C. B.; Kagan, C. R. Engineering Charge Injection and Charge Transport for High Performance PbSe Nanocrystal Thin Film Devices and Circuits. *Nano Lett.* **2014**, *14*, 6210–6216.
- (152) Kim, D. K.; Lai, Y.; Diroll, B. T.; Murray, C. B.; Kagan, C. R. Flexible and Low-Voltage Integrated Circuits Constructed from High-Performance Nanocrystal Transistors. *Nat. Commun.* **2012**, *3*, 1216.
- (153) Konstantatos, G.; Sargent, E. H. Solution-Processed Quantum Dot Photodetectors. *Proc. IEEE* **2009**, *97*, 1666–1683.
- (154) McDonald, S. A.; Konstantatos, G.; Zhang, S.; Cyr, P. W.; Klem, E. J. D.; Levina, L.; Sargent, E. H. Solution-Processed PbS Quantum Dot Infrared Photodetectors and Photovoltaics. *Nat. Mater.* **2005**, *4*, 138–142.
- (155) Gosztola, D.; Wang, B.; Wasielewski, M. R. Factoring the Contribution of Through-Space and Through-Bond Interactions to Rates of Photoinduced Electron Transfer in Donor-Spacer-Acceptor Molecules Using Ultrafast Transient Absorption Spectroscopy. In *Ultrafast Phenomena X*; Springer, Berlin, Heidelberg, 1996; pp. 230–232.
- (156) Quardokus, R. C.; Lu, Y.; Wasio, N. A.; Lent, C. S.; Justaud, F.; Lapinte, C.; Kandel, S. A. Through-Bond versus Through-Space Coupling in Mixed-Valence Molecules: Observation of Electron Localization at the Single-Molecule Scale. *J. Am. Chem. Soc.* **2012**, *134*, 1710–1714.
- (157) Hush, N. S. Distance Dependence of Electron Transfer Rates. *Coord. Chem. Rev.* **1985**, *64*, 135–157.
- (158) Liu, R.; Bloom, B. P.; Waldeck, D. H.; Zhang, P.; Beratan, D. N. Controlling the Electron-Transfer Kinetics of Quantum-Dot Assemblies. *J. Phys. Chem. C* **2017**, *121*, 14401–14412.
- (159) Lee, J.-S.; Kovalenko, M. V.; Huang, J.; Chung, D. S.; Talapin, D. V. Band-like Transport, High Electron Mobility and High Photoconductivity in All-Inorganic Nanocrystal Arrays. *Nat. Nanotechnol.* **2011**, *6*, 348–352.
- (160) Sun, L.; Choi, J. J.; Stachnik, D.; Bartnik, A. C.; Hyun, B.-R.; Malliaras, G. G.; Hanrath, T.; Wise, F. W. Bright Infrared Quantum-Dot Light-Emitting Diodes through Inter-Dot Spacing Control. *Nat. Nanotechnol.* **2012**, *7*, 369–373.

- (161) Cho, K.-S.; Lee, E. K.; Joo, W.-J.; Jang, E.; Kim, T.-H.; Lee, S. J.; Kwon, S.-J.; Han, J. Y.; Kim, B.-K.; Choi, B. L.; *et al.* High-Performance Crosslinked Colloidal Quantum-Dot Light-Emitting Diodes. *Nat. Photonics* **2009**, *3*, 341.
- (162) Naaman, R.; Waldeck, D. H. Spintronics and Chirality: Spin Selectivity in Electron Transport Through Chiral Molecules. *Annu. Rev. Phys. Chem.* **2015**, *66*, 263–281.
- (163) Göhler, B.; Hamelbeck, V.; Markus, T. Z.; Kettner, M.; Hanne, G. F.; Vager, Z.; Naaman, R.; Zacharias, H. Spin Selectivity in Electron Transmission through Self-Assembled Monolayers of Double-Stranded DNA. *Science* **2011**, *331*, 894–897.
- (164) Michaeli, K.; Kantor-Uriel, N.; Naaman, R.; Waldeck, D. H. The Electron's Spin and Molecular Chirality - How Are They Related and How Do They Affect Life Processes? *Chem. Soc. Rev.* **2016**, *45*, 6478–6487.
- (165) Naaman, R.; Waldeck, D. H. Chiral-Induced Spin Selectivity Effect. *J. Phys. Chem. Lett.* **2012**, *3*, 2178–2187.
- (166) Kumar, A.; Capua, E.; Kesharwani, M. K.; Martin, J. M. L.; Sitbon, E.; Waldeck, D. H.; Naaman, R. Chirality-Induced Spin Polarization Places Symmetry Constraints on Biomolecular Interactions. *Proc. Natl. Acad. Sci. U. S. A.* **2017**, *114*, 2474–2478.
- (167) Berstis, L.; Beckham, G. T.; Crowley, M. F. Electronic Coupling through Natural Amino Acids. *J. Chem. Phys.* **2015**, *143*, 225102.
- (168) Song, P.; Li, Y.; Ma, F.; Pullerits, T.; Sun, M. External Electric Field-Dependent Photoinduced Charge Transfer in a Donor–Acceptor System for an Organic Solar Cell. *J. Phys. Chem. C* **2013**, *117*, 15879–15889.
- (169) Bang, J. H.; Kamat, P. V. Quantum Dot Sensitized Solar Cells. A Tale of Two Semiconductor Nanocrystals: CdSe and CdTe. *ACS Nano* **2009**, *3*, 1467–1476.
- (170) Liang, Y.; Thorne, J. E.; Parkinson, B. A. Controlling the Electronic Coupling between CdSe Quantum Dots and Thiol Capping Ligands via pH and Ligand Selection. *Langmuir* **2012**, *28*, 11072–11077.
- (171) Perkins, S. J. Protein Volumes and Hydration Effects. *Eur. J. Biochem.* **1986**, *157*, 169–180.
- (172) D.A. Case, D.S. Cerutti, T.E. Cheatham, III, T.A. Darden, R.E. Duke, T.J. Giese, H. Gohlke, A.W. Goetz, D. Greene, N. Homeyer, S. Izadi, A. Kovalenko, T.S. Lee, S.

- LeGrand, P. Li, C. Lin, J. Liu, T. Luchko, R. Luo, D. Mermelstein, K.M. Merz, G. Monard, H. Nguyen, I. Omelyan, A. Onufriev, F. Pan, R. Qi, D.R. Roe, A. Roitberg, C. Sagui, C.L. Simmerling, W.M. Botello-Smith, J. Swails, R.C. Walker, J. Wang, R.M. Wolf, X. Wu, L. Xiao, D.M. York and P.A. Kollman. AMBER 2014. *University of California, San Francisco* **2014**.
- (173) Bhattacharya, S. K.; Kshirsagar, A. First Principle Study of Free and Surface Terminated CdTe Nanoparticles. *Eur. Phys. J. D* **2008**, *48*, 355–364.
- (174) Cui, P.; Mayo, M.; Kilina, S. The Electronic Structure of Cd₃₃Se₃₃ Quantum Dots Passivated with Various [Me(bpy)₃]²⁺ Complexes: A Comparative Study Based on DFT and TDDFT Simulation. In *APS Meeting Abstracts*; 2013.
- (175) Dolai, S.; Nimmala, P. R.; Mandal, M.; Muhoberac, B. B.; Dria, K.; Dass, A.; Sardar, R. Isolation of Bright Blue Light-Emitting CdSe Nanocrystals with 6.5 kDa Core in Gram Scale: High Photoluminescence Efficiency Controlled by Surface Ligand Chemistry. *Chem. Mater.* **2014**, *26*, 1278–1285.
- (176) Wang, Y.; Zhang, Y.; Wang, F.; Giblin, D. E.; Hoy, J.; Rohrs, H. W.; Loomis, R. A.; Buhro, W. E. The Magic-Size Nanocluster (CdSe)₃₄ as a Low-Temperature Nucleant for Cadmium Selenide Nanocrystals; Room-Temperature Growth of Crystalline Quantum Platelets. *Chem. Mater.* **2014**, *26*, 2233–2243.
- (177) M. J. Frisch, G. W. Trucks, H. B. Schlegel, G. E. Scuseria, M. A. Robb, J. R. Cheeseman, G. Scalmani, V. Barone, G. A. Petersson, H. Nakatsuji, X. Li, M. Caricato, A. V. Marenich, J. Bloino, B. G. Janesko, R. Gomperts, B. Mennucci, H. P. Hratchian, J. V. Ortiz, A. F. Izmaylov, J. L. Sonnenberg, D. Williams-Young, F. Ding, F. Lipparini, F. Egidi, J. Goings, B. Peng, A. Petrone, T. Henderson, D. Ranasinghe, V. G. Zakrzewski, J. Gao, N. Rega, G. Zheng, W. Liang, M. Hada, M. Ehara, K. Toyota, R. Fukuda, J. Hasegawa, M. Ishida, T. Nakajima, Y. Honda, O. Kitao, H. Nakai, T. Vreven, K. Throssell, J. A. Montgomery, Jr., J. E. Peralta, F. Ogliaro, M. J. Bearpark, J. J. Heyd, E. N. Brothers, K. N. Kudin, V. N. Staroverov, T. A. Keith, R. Kobayashi, J. Normand, K. Raghavachari, A. P. Rendell, J. C. Burant, S. S. Iyengar, J. Tomasi, M. Cossi, J. M. Millam, M. Klene, C. Adamo, R. Cammi, J. W. Ochterski, R. L. Martin, K. Morokuma, O. Farkas, J. B. Foresman, and D. J. Fox. Gaussian 16, Revision A.03. *Gaussian, Inc., Wallingford CT*, **2016**.
- (178) Shao, Y.; Gan, Z.; Epifanovsky, E.; Gilbert, A. T. B.; Wormit, M.; Kussmann, J.; Lange, A. W.; Behn, A.; Deng, J.; Feng, X.; *et al.* Advances in Molecular Quantum Chemistry Contained in the Q-Chem 4 Program Package. *Mol. Phys.* **2015**, *113*, 184–215.

- (179) Wu, Q.; Voorhis, T. V. Direct Calculation of Electron Transfer Parameters through Constrained Density Functional Theory. *J. Phys. Chem. A* **2006**, *110*, 9212–9218.
- (180) Lin, J.; Balabin, I. A.; Beratan, D. N. The Nature of Aqueous Tunneling Pathways between Electron-Transfer Proteins. *Science* **2005**, *310*, 1311–1313.
- (181) Nitzan, A. *Chemical Dynamics in Condensed Phases : Relaxation, Transfer and Reactions in Condensed Molecular Systems: Relaxation, Transfer and Reactions in Condensed Molecular Systems*; Oxford Graduate Texts; OUP Oxford, 2006.
- (182) Xu, F.; Gerlein, L. F.; Ma, X.; Haughn, C. R.; Doty, M. F.; Cloutier, S. G. Impact of Different Surface Ligands on the Optical Properties of PbS Quantum Dot Solids. *Materials* **2015**, *8*, 1858–1870.
- (183) Raffaele, R. P.; Castro, S. L.; Hepp, A. F.; Bailey, S. G. Quantum Dot Solar Cells. *Prog. Photovoltaics Res. Appl.* **2002**, *10*, 433–439.
- (184) Barito, A.; Sykes, M. E.; Huang, B.; Bilby, D.; Frieberg, B.; Kim, J.; Green, P. F.; Shtein, M. Universal Design Principles for Cascade Heterojunction Solar Cells with High Fill Factors and Internal Quantum Efficiencies Approaching 100%. *Adv. Energy Mater.* **2014**, *4*, 1400216.
- (185) Sim, M.; Kim, J. S.; Shim, C.; Cho, K. Cascade Organic Solar Cells with Energy-Level-Matched Three Photon-Harvesting Layers. *Chem. Phys. Lett.* **2013**, *557*, 88–91.
- (186) Heidel, T. D.; Hochbaum, D.; Sussman, J. M.; Singh, V.; Bahlke, M. E.; Hiromi, I.; Lee, J.; Baldo, M. A. Reducing Recombination Losses in Planar Organic Photovoltaic Cells Using Multiple Step Charge Separation. *J. Appl. Phys.* **2011**, *109*, 104502.
- (187) Cnops, K.; Rand, B. P.; Cheyng, D.; Heremans, P. Enhanced Photocurrent and Open-Circuit Voltage in a 3-Layer Cascade Organic Solar Cell. *Appl. Phys. Lett.* **2012**, *101*, 143301.
- (188) Barito, A.; Sykes, M. E.; Bilby, D.; Amonoo, J.; Jin, Y.; Morris, S. E.; Green, P. F.; Kim, J.; Shtein, M. Recovering Lost Excitons in Organic Photovoltaics Using a Transparent Dissociation Layer. *J. Appl. Phys.* **2013**, *113*, 203110.
- (189) Endres, J.; Pelczer, I.; Rand, B. P.; Kahn, A. Determination of Energy Level Alignment within an Energy Cascade Organic Solar Cell. *Chem. Mater.* **2016**, *28*, 794–801.

- (190) Lan, X.; Voznyy, O.; García de Arquer, F. P.; Liu, M.; Xu, J.; Proppe, A. H.; Walters, G.; Fan, F.; Tan, H.; Liu, M.; *et al.* 10.6% Certified Colloidal Quantum Dot Solar Cells via Solvent-Polarity-Engineered Halide Passivation. *Nano Lett.* **2016**, *16*, 4630–4634.
- (191) Liu, H.; Tian, Y.; Zhang, Y.; Gao, K.; Lu, K.; Wu, R.; Qin, D.; Wu, H.; Peng, Z.; Hou, L.; *et al.* Solution Processed CdTe/CdSe Nanocrystal Solar Cells with More than 5.5% Efficiency by Using an Inverted Device Structure. *J. Mater. Chem.* **2015**, *3*, 4227–4234.
- (192) Tong, S. W.; Mishra, N.; Su, C. L.; Nalla, V.; Wu, W.; Ji, W.; Zhang, J.; Chan, Y.; Loh, K. P. High-Performance Hybrid Solar Cell Made from CdSe/CdTe Nanocrystals Supported on Reduced Graphene Oxide and PCDTBT. *Adv. Funct. Mater.* **2014**, *24*, 1904–1910.
- (193) Ju, T.; Yang, L.; Carter, S. Thickness Dependence Study of Inorganic CdTe/CdSe Solar Cells Fabricated from Colloidal Nanoparticle Solutions. *J. Appl. Phys.* **2010**, *107*, 104311.
- (194) Santra, P. K.; Kamat, P. V. Tandem-Layered Quantum Dot Solar Cells: Tuning the Photovoltaic Response with Luminescent Ternary Cadmium Chalcogenides. *J. Am. Chem. Soc.* **2013**, *135*, 877–885.
- (195) Tyrrell, E. J.; Smith, J. M. Effective Mass Modeling of Excitons in Type-II Quantum Dot Heterostructures. *Phys. Rev. B Condens. Matter* **2011**, *84*, 165328.
- (196) Yonemoto, E. H.; Riley, R. L.; Kim, Y. I.; Atherton, S. J.; Schmehl, R. H.; Mallouk, T. E. Photoinduced Electron Transfer in Covalently Linked Ruthenium Tris(bipyridyl)-Viologen Molecules: Observation of Back Electron Transfer in the Marcus Inverted Region. *J. Am. Chem. Soc.* **1992**, *114*, 8081–8087.
- (197) Krüger, J.; Plass, R.; Cevey, L.; Piccirelli, M.; Grätzel, M.; Bach, U. High Efficiency Solid-State Photovoltaic Device due to Inhibition of Interface Charge Recombination. *Appl. Phys. Lett.* **2001**, *79*, 2085–2087.
- (198) Snaith, H. J.; Moule, A. J.; Klein, C.; Meerholz, K.; Friend, R. H.; Grätzel, M. Efficiency Enhancements in Solid-State Hybrid Solar Cells via Reduced Charge Recombination and Increased Light Capture. *Nano Lett.* **2007**, *7*, 3372–3376.
- (199) Liu, J.; Pathak, S.; Stergiopoulos, T.; Leijtens, T.; Wojciechowski, K.; Schumann, S.; Kausch-Busies, N.; Snaith, H. J. Employing PEDOT as the P-Type Charge Collection Layer in Regular Organic-Inorganic Perovskite Solar Cells. *J. Phys. Chem.*

- Lett.* **2015**, *6*, 1666–1673.
- (200) Talgorn, E.; de Vries, M. A.; Siebbeles, L. D. A.; Houtepen, A. J. Photoconductivity Enhancement in Multilayers of CdSe and CdTe Quantum Dots. *ACS Nano* **2011**, *5*, 3552–3558.
- (201) Wang, S.; Dong, W.; Fang, X.; Wu, S.; Tao, R.; Deng, Z.; Shao, J.; Hu, L.; Zhu, J. CdS and CdSe Quantum Dot Co-Sensitized Nanocrystalline TiO₂ Electrode: Quantum Dot Distribution, Thickness Optimization, and the Enhanced Photovoltaic Performance. *J. Power Sources* **2015**, *273*, 645–653.
- (202) Erwin, P.; Conron, S. M.; Golden, J. H.; Allen, K.; Thompson, M. E. Implications of Multichromophoric Arrays in Organic Photovoltaics. *Chem. Mater.* **2015**, *27*, 5386–5392.
- (203) Gust, D.; Moore, T. A.; Makings, L. R.; Liddell, P. A.; Nemeth, G. A.; Moore, A. L. Photodriven Electron Transfer in Triad Molecules: A Two-Step Charge Recombination Reaction. *J. Am. Chem. Soc.* **1986**, *108*, 8028–8031.
- (204) McGarrah, J. E.; Kim, Y.-J.; Hissler, M.; Eisenberg, R. Toward a Molecular Photochemical Device: A Triad for Photoinduced Charge Separation Based on a Platinum Diimine Bis (acetylide) Chromophore. *Inorg. Chem.* **2001**, *40*, 4510–4511.
- (205) Moore, T. A.; Gust, D.; Mathis, P.; Mialocq, J.-C.; Chachaty, C.; Bensasson, R. V.; Land, E. J.; Doizi, D.; Liddell, P. A.; Lehman, W. R.; *et al.* Photodriven Charge Separation in a Carotenoporphyrin–quinone Triad. **1984**, *307*, 630–632.
- (206) Johnson, D. G.; Niemczyk, M. P.; Minsek, D. W.; Wiederrecht, G. P.; Svec, W. A.; Iii, G. L. G.; Wasielewski, M. R. Photochemical Electron Transfer in Chlorophyll-Porphyrin-Quinone Triads: The Role of the Porphyrin-Bridging Molecule. *J. Am. Chem. Soc.* **1993**, *115*, 5692–5701.
- (207) McGarrah, J. E.; Hupp, J. T.; Smirnov, S. N. Electron Transfer in Platinum(II) Diimine-Centered Triads: Mechanistic Insights from Photoinduced Transient Displacement Current Measurements. *J. Phys. Chem. A* **2009**, *113*, 6430–6436.
- (208) Megiatto, J. D., Jr; Antoniuk-Pablant, A.; Sherman, B. D.; Kodis, G.; Gervaldo, M.; Moore, T. A.; Moore, A. L.; Gust, D. Mimicking the Electron Transfer Chain in Photosystem II with a Molecular Triad Thermodynamically Capable of Water Oxidation. *Proc. Natl. Acad. Sci. U. S. A.* **2012**, *109*, 15578–15583.
- (209) Griffith, O. L.; Forrest, S. R. Exciton Management in Organic Photovoltaic

Multidonor Energy Cascades. *Nano Lett.* **2014**, *14*, 2353–2358.

- (210) Pradhan, S.; Stavrinadis, A.; Gupta, S.; Christodoulou, S.; Konstantatos, G. Breaking the Open-Circuit Voltage Deficit Floor in PbS Quantum Dot Solar Cells through Synergistic Ligand and Architecture Engineering. *ACS Energy Lett.* **2017**, *1444*–1449.
- (211) Chuang, C.-H. M.; Maurano, A.; Brandt, R. E.; Hwang, G. W.; Jean, J.; Buonassisi, T.; Bulović, V.; Bawendi, M. G. Open-Circuit Voltage Deficit, Radiative Sub-Bandgap States, and Prospects in Quantum Dot Solar Cells. *Nano Lett.* **2015**, *15*, 3286–3294.
- (212) Zhao, T.; Goodwin, E. D.; Guo, J.; Wang, H.; Diroll, B. T.; Murray, C. B.; Kagan, C. R. Advanced Architecture for Colloidal PbS Quantum Dot Solar Cells Exploiting a CdSe Quantum Dot Buffer Layer. *ACS Nano* **2016**.
- (213) He, Z.; Zhong, C.; Huang, X.; Wong, W.-Y.; Wu, H.; Chen, L.; Su, S.; Cao, Y. Simultaneous Enhancement of Open-Circuit Voltage, Short-Circuit Current Density, and Fill Factor in Polymer Solar Cells. *Adv. Mater.* **2011**, *23*, 4636–4643.
- (214) Chen, H.-Y.; Hou, J.; Zhang, S.; Liang, Y.; Yang, G.; Yang, Y.; Yu, L.; Wu, Y.; Li, G. Polymer Solar Cells with Enhanced Open-Circuit Voltage and Efficiency. *Nat. Photonics* **2009**, *3*, 649–653.
- (215) Labelle, A. J.; Thon, S. M.; Masala, S.; Adachi, M. M.; Dong, H.; Farahani, M.; Ip, A. H.; Fratalocchi, A.; Sargent, E. H. Colloidal Quantum Dot Solar Cells Exploiting Hierarchical Structuring. *Nano Lett.* **2015**, *15*, 1101–1108.
- (216) Einax, M.; Nitzan, A. Network Analysis of Photovoltaic Energy Conversion. *J. Phys. Chem. C* **2014**, *118*, 27226–27234.
- (217) Einax, M.; Nitzan, A. Maximum Efficiency of State-Space Models of Nanoscale Energy Conversion Devices. *J. Chem. Phys.* **2016**, *145*, 014108.
- (218) Einax, M.; Dierl, M.; Schiff, P. R.; Nitzan, A. Multiple State Representation Scheme for Organic Bulk Heterojunction Solar Cells: A Novel Analysis Perspective. *EPL* **2013**, *104*, 40002.
- (219) Shockley, W.; Queisser, H. J. Detailed Balance Limit of Efficiency of P-n Junction Solar Cells. *J. Appl. Phys.* **1961**, *32*, 510–519.
- (220) Kuhn, H.; Försterling, H.-D.; Waldeck, D. H. *Principles of Physical Chemistry*; John

Wiley & Sons: New York, 2009.

- (221) Rutten, B.; Esposito, M.; Cleuren, B. Reaching Optimal Efficiencies Using Nanosized Photoelectric Devices. *Phys. Rev. B Condens. Matter* **2009**, *80*, 235122.
- (222) Haynes, W. M. *CRC Handbook of Chemistry and Physics, 95th Edition*; CRC Press: Boca Raton, FL, 2014.
- (223) Marple, D. T. F. Effective Electron Mass in CdTe. *Phys. Rev.* **1963**, *129*, 2466–2470.
- (224) Kubo, S.; Onuki, M. Effective Electron Mass in CdSe. *J. Phys. Soc. Jpn.* **1965**, *20*, 1280–1280.
- (225) Popadic, M.; Lorito, G.; Nanver, L. K. Analytical Model of I - V Characteristics of Arbitrarily Shallow P-N Junctions. *IEEE Trans. Electron Devices* **2009**, *56*, 116–125.
- (226) Giebink, N. C.; Wiederrecht, G. P.; Wasielewski, M. R.; Forrest, S. R. Ideal Diode Equation for Organic Heterojunctions. I. Derivation and Application. *Phys. Rev. B Condens. Matter* **2010**, *82*, 155305.
- (227) Gadisa, A.; Svensson, M.; Andersson, M. R.; Inganäs, O. Correlation between Oxidation Potential and Open-Circuit Voltage of Composite Solar Cells Based on Blends of Polythiophenes/fullerene Derivative. *Appl. Phys. Lett.* **2004**, *84*, 1609–1611.
- (228) Rand, B. P.; Burk, D. P.; Forrest, S. R. Offset Energies at Organic Semiconductor Heterojunctions and Their Influence on the Open-Circuit Voltage of Thin-Film Solar Cells. *Phys. Rev. B Condens. Matter* **2007**, *75*, 115327.
- (229) Liu, M.; Voznyy, O.; Sabatini, R.; García de Arquer, F. P.; Munir, R.; Balawi, A. H.; Lan, X.; Fan, F.; Walters, G.; Kirmani, A. R.; *et al.* Hybrid Organic-Inorganic Inks Flatten the Energy Landscape in Colloidal Quantum Dot Solids. *Nat. Mater.* **2017**, *16*, 258–263.

Biography

Ruibin Liu was born in Jiangxi province of China on October 23, 1988. He got his B.S. degree at University of Science and Technology of China in 2011. He begun this Ph.D. study in August 2011 and joined Prof. David N. Beratan's research group in 2012. In the graduate study, he was a teaching assistant for the Department of Chemistry and a research assistant in the group. He published and was preparing the following papers.

(1) Brian P. Bloom; **Ruibin Liu**; Peng Zhang; Ron Naaman; David N. Beratan; David H. Waldeck "Directing Charge Transfer in Quantum Dot Assemblies" (permitted by *Acc. Chem. Res.*; in preparation)

(2) **Ruibin Liu**; Peng Zhang; David N. Beratan "Charge-influenced Through-solvent and Through-bridge Electron Transfer Between Linked Quantum Dots" (in preparation)

(3) **Ruibin Liu**; Brian P. Bloom; David H. Waldeck; Peng Zhang; David N. Beratan "Improving Solar Cell Performance Using Quantum Dot Triad Charge-Separation Engines" *J. Phys. Chem. C*, 2018, 122 (11), pp 5924–5934

(4) **Ruibin Liu**; Brian P. Bloom; David H. Waldeck; Peng Zhang; David N. Beratan "Controlling the Electron-Transfer Kinetics of Quantum-Dot Assemblies" *J. Phys. Chem. C*, 2017, 121 (27), pp 14401–14412

(5) Brian P. Bloom; **Ruibin Liu** et. al. "Ligand-Induced Changes in the Characteristic Size-Dependent Electronic Energies of CdSe Nanocrystals" *J. Phys. Chem. C*, 2013, 117 (43), pp 22401–22411